



# Università degli Studi di Ferrara

DOTTORATO DI RICERCA IN  
SCIENZE DELL'INGEGNERIA

CICLO XXIII

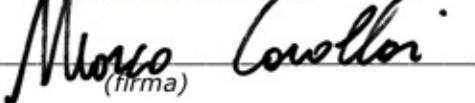
COORDINATORE Prof. Trillo Stefano

A Lumped Parameter Model  
for the Pressure and Vibration Analysis of  
Variable Displacement Vane Pumps

Settore Scientifico Disciplinare ING-IND/13

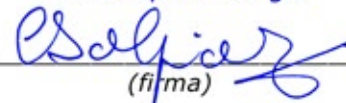
**Dottorando**

Dot. Cavallari Marco

  
(firma)

**Tutore**

Prof. Dalpiaz Giorgio

  
(firma)

Anni 2008/2010



# Riassunto

*L'argomento affrontato in questa tesi riguarda lo sviluppo di un modello a parametri concentrati in grado di simulare il comportamento vibratorio di pompe a palette a cilindrata variabile. Si tratta di un modello piano a tre gradi di libertà, deputato allo studio della dinamica delle parti in rotazione. Tale modello considera l'azione delle forze di pressione variabili sul rotore, le reazioni dei cuscinetti idrodinamici, l'attrito dovuto alle azioni viscosse ed alle forze di contatto, le proprietà del rotore in termini di rigidezza e smorzamento, le variazioni della geometria della pompa in funzione delle condizioni di esercizio ed infine, tutte le azioni d'inerzia. In particolare, il calcolo delle forze e delle coppie di pressione è svolto grazie alla valutazione preliminare del campo di pressione mediante un modello basato su un approccio euleriano che considera 26 volumi di controllo.*

*Il modello in questione può quindi determinare il campo di pressione agente all'interno della pompa e calcolare le accelerazioni a cui è sottoposto il rotore, le forze di reazione dei cuscinetti fluido-dinamici e la coppia motrice assorbita dalla pompa in condizioni operative.*

*Dopo la descrizione del modello dal punto di vista teorico, vengono presentati la campagna sperimentale ed il metodo di validazione. A tal pro si è sviluppata un'originale metodologia, che consiste nel comparare le accelerazioni del corpo pompa calcolate servendosi del modello con le medesime accelerazioni misurate in condizioni di esercizio.*

*Infine alcuni significativi risultati vengono riportati quale esempio di applicazione.*

*Il principale contributo originale di questa tesi consiste nello sviluppo di un modello dinamico non lineare di pompe a palette a cilindrata variabile che include simultaneamente i più rilevanti fenomeni dinamici presenti nel funzionamento della pompa e la valutazione delle loro interazioni. Questa peculiarità può essere importante al fine di investigare l'influenza di modifiche progettuali sul comportamento del sistema meccanico in questione e, in questo senso, il modello sviluppato può essere considerato un valido strumento di prototipazione, in grado di identificare l'origine di effetti dinamici indesiderati.*



# Abstract

*This PhD thesis presents a lumped parameter model able to simulate the vibrational behavior of a wide range of variable displacement vane pumps. The vibration analysis of the rotating parts is carried out through a planar model with three degrees of freedom. It takes into account the variability of the pressure loads acting on the rotor shaft, the hydrodynamic journal bearing reactions, the friction due to viscous actions and contact forces, the rotor shaft stiffness and damping, the variation of the pump geometry with respect to working condition and all the inertia actions. In particular, the computation of pressure forces and torques is allowed by the preliminary evaluation of the variable pressure field acting inside the pump, obtained through a model based on an Euler's approach with 26 control volumes.*

*Thus, the present model makes it possible to define the pressure field acting inside the pump, and calculate the rotor shaft accelerations, as well as the journal bearing reaction forces and the motor drive torque absorbed by the pump in working condition.*

*The test campaign and the validation method are then described: an original assessment technique based on the comparison of pump casing accelerations is proposed.*

*Finally, some important simulation results are reported as an example of application.*

*The main original contribution of this work concerns the development of a non-linear model of variable displacement vane pumps including all the important dynamic effects in the same model, with the aim at taking into account their interactions. This can be important in order to foresee the influence of working conditions and design modifications on the pump vibrational behavior. In this sense the developed lumped parameter model could be a very useful tool in prototype design, in order to identify the origin of unwanted dynamic effects.*



# Preface

Nowadays, increasing attention is addressed to vibro-acoustic problems in mechanical systems to improve their performances in terms of precision, reliability and comfort. In this frame the research activity I carried out during my PhD has dealt with the development of methodologies and applicative tools integrating vibro-acoustic modeling and experimental analysis with the aim to optimize the vibro-acoustic behavior of mechanical systems and to understand the complex phenomena related to their operational conditions. In more detail, my activity focused on the study of advanced modeling, simulation and experimental assessment techniques for the characterization of complex machinery and physical systems. The two main topics I studied in the last three years are the nearfield structure-borne sound holography applied to shell shape elements and the lumped parameter modeling of variable displacement vane pumps. This last topic will be widely discussed in the present work.

When dealing with complex mechanical systems, such as variable displacement vane pumps, an accurate prediction of the system dynamical behavior is capitally important in a proper vibro-acoustical optimization. The first target is the simulation of the pressure field acting inside the pump. As a matter of fact the pressure fields is the main actor in determining the time variable loads acting on the pump casing. In this sight a zero-dymensional model, based on an Euler's approach has been developed allowing to compute the pressure evolution by solving a system of flow rate continuity equations. The results have been validated by comparison with experimental pressure evolutions. Furthermore, the forces exciting the rotor shaft have been calculated and used as input data for a kineto-elastodynamic model that analyzes the equilibrium between the resulting pressure forces, the journal bearings reactions and the inertial actions. In this way the variable forces exciting the pump casing in working condition are fully characterized.

Another important activity deals with the frequency response function of the pump casing. To do this, an original procedure has been studied to better simulate the pump behavior in working conditions.

Finally the model outputs in term of time varying forces and the experimental frequency response functions can be used to estimate the pump casing accelerations that are the main noise cause. Such a global analysis approach can be rarely found in the literature and involves a large number of modeling techniques at the same time.

Part of this activity has been reported in the following publication:

---

Cavallari, M., Montanari, A., Mucchi, E., and Dalpiaz, G. "Analysis of the evolution of the pressure forces in variable displacement vane pumps using different approaches". By Meneghetti, U., Maggiore, A., Parenti Castelli, V., in *Quarta Giornata di studio in onore di Ettore Funaioli*, 16<sup>th</sup> July 2010, Ed. Asterisco, Bologna (acts in press).

The activity about nearfield structure-borne sound holography have been carried out during a period of six months I spent to the *Department of Fluid Mechanics and Engineering Acoustics* of the *Technische Universität Berlin*, under the supervision of Prof. B. A. T. Petersson. This project have been developed in the frame of the *EDSVS* program (European Doctorate in Sound and Vibration Studies) with the aim at defining a new technique suitable to reconstruct the velocity and force fields acting on the surface of a shell shape element with multiple excitation points (further information can be found at [www.isvr.soton.ac.uk/edsvs/pro08\\_Marco\\_Cavallari.htm](http://www.isvr.soton.ac.uk/edsvs/pro08_Marco_Cavallari.htm)). This novel approach allows to calculate the excitation forces starting from vibrational velocity measurements of the same structure in the near field. The structure has been modeled in MATLAB environment and the results have been experimentally assessed after having characterized the source-receiver coupling thanks to a test bench suitably designed. The promising results of this activity have been related in this publication:

Cavallari, M., Bonhoff, H. A., and Petersson B. A. T., 2009, "Nearfield structure-borne sound holography". In *NOVEM 2009*, 5–8 April 2009, Oxford.

Moreover, I worked in the diagnostics of mechanical systems by means of advanced signal processing techniques. In this frame I developed the cyclostationary modelling and other advanced techniques for the diagnosis of assembly faults in internal combustion engine cold tests; I studied polyurethane heavy-duty wheels for industrial applications to detect contamination faults and finally I worked on signal precessing techniques applied to fault detection in helical gearboxes.

Delvecchio, S., D'Elia, G., Cavallari, M., and Dalpiaz, G., 2008, "Use of the cyclostationary modelling for the diagnosis of assembly faults in i.c. engine cold tests". In *Proceedings of ISMA2008*, 15–17 September 2008, Leuven, Belgium.

Cavallari. M., D'Elia, G., Delvecchio, S., Malagò, M., Mucchi, E. and Dalpiaz, G., 2009, "On the use of vibration signal analysis for industrial quality control". In *acts of Aimeta 2009*, 14–17 September 2009, Ancona, Italy.

Cavallari, M., D'Elia, G., Delvecchio, S., Malagò, M., Mucchi, E. and Dalpiaz, G., 2010, "Condition monitoring by means of vibration analysis techniques: some case studies". By Meneghetti, U., Maggiore, A., Parenti Castelli, V., in *Terza Giornata di studio in onore di Ettore Funaioli*, 16<sup>th</sup> July 2009, Ed. Asterisco, Bologna, ISBN 978 – 902128 – 8 – 8. Available online: <http://amsacta.cib.unibo.it/2771/>.

At the end of my PhD experience I wish to thank *BERARMA s.r.l* (Casalecchio di Reno, Bologna, Italy) for their active co-operation during the test campaigns and all the people I have worked with during the last three years, in Italy and in



---

Germany. Many tanks to my colleagues and friends Gabriele, Gianluca, Simone, Stefano and Marco: I feel honored to have worked with all of you.

Finally a special tanks to Emiliano and to my supervisor, Prof. Giorgio Dalpiaz for their help during my studies.

Ferrara, 03/02/2011

Marco Cavallari



# Contents

<b>Riassunto</b>	<b>iii</b>
<b>Abstract</b>	<b>v</b>
<b>Preface</b>	<b>vii</b>
<b>List of figures</b>	<b>xiii</b>
<b>List of tables</b>	<b>xix</b>
<b>List of symbols</b>	<b>xxi</b>
<b>1 Introduction</b>	<b>1</b>
1.1 Variable displacement vane pumps peculiarities . . . . .	1
1.2 Modeling mechanical systems . . . . .	2
1.2.1 Physical model . . . . .	3
1.2.2 Mathematical model . . . . .	4
1.2.3 Integration . . . . .	4
1.3 Variable displacement vane pump: state of the art and modeling	4
1.4 Overview of the thesis . . . . .	6
<b>2 General description of a variable displacement vane pump</b>	<b>9</b>
2.1 Vane pump basic description . . . . .	9
2.2 BERARMA <i>PHV 05</i> pump . . . . .	14
2.2.1 Overview . . . . .	14
2.2.2 <i>PHV 05</i> design parameters . . . . .	14
2.3 Working condition description . . . . .	15
<b>3 Model description</b>	<b>25</b>
3.1 General description of the model . . . . .	25
3.2 Pressure distribution . . . . .	26
3.2.1 Flow rates involved in continuity equations . . . . .	28
3.2.2 Flow rate equations . . . . .	34
3.2.3 System integration . . . . .	37
3.3 Auxiliary quantities for pressure distribution calculation . . . . .	38
3.3.1 Shaft displacement . . . . .	38
3.3.2 Distance between rotor center and pressure ring . . . . .	40
3.3.3 Volume evolution for a vane space . . . . .	40
3.3.4 Volume evolution for a hole control volume . . . . .	42

---

3.3.5	Rate of volume variation . . . . .	42
3.3.6	Passage area evolution for a vane space . . . . .	43
3.3.7	Passage area evolution for a hole control volume . . . . .	48
3.4	Force estimation . . . . .	50
3.4.1	Force acting on the rotor . . . . .	50
3.4.2	Journal bearing reaction forces . . . . .	52
3.5	Torque estimation . . . . .	56
3.5.1	Torque due to pressure distribution . . . . .	56
3.5.2	Friction torque . . . . .	57
3.5.3	Torque due to viscous actions . . . . .	57
3.5.4	Motor drive torque . . . . .	58
3.6	The static equilibrium position . . . . .	59
3.7	Preliminary analysis . . . . .	60
<b>4</b>	<b>Model implementation in MATLAB and Simulink</b>	<b>67</b>
4.1	Integration of the equations of motion . . . . .	67
4.2	Pressure and force field calculation . . . . .	71
4.2.1	The function containing data: <i>data.m</i> . . . . .	71
4.2.2	The function <i>complete_look_up.m</i> . . . . .	76
4.2.3	The function <i>pressure_field.m</i> . . . . .	76
4.2.4	The function <i>rotor_dyn_force.m</i> . . . . .	77
4.2.5	The script <i>full_model.m</i> . . . . .	77
<b>5</b>	<b>Experimental validation</b>	<b>83</b>
5.1	Method . . . . .	83
5.2	Experimental tests . . . . .	84
5.2.1	Pressure evolution measurements . . . . .	84
5.2.2	Flow rate measurements . . . . .	84
5.2.3	Torque measurements . . . . .	87
5.2.4	Pressure force evolution calculation . . . . .	87
5.2.5	Case frequency response functions . . . . .	92
5.2.6	Case vibration measurements . . . . .	93
5.3	Comparing numerical and experimental results . . . . .	98
5.3.1	Pressure evolutions . . . . .	98
5.3.2	Flow rates . . . . .	101
5.3.3	Motor drive torque . . . . .	103
5.3.4	Forces on the pressure ring . . . . .	103
5.3.5	Forces on the rotor shaft . . . . .	107
5.3.6	Pump casing accelerations . . . . .	110
<b>6</b>	<b>Results and applications</b>	<b>117</b>
6.1	Dynamical events identification . . . . .	117
6.1.1	Full flow condition . . . . .	117
6.1.2	Zero flow condition . . . . .	121
<b>7</b>	<b>Concluding remarks</b>	<b>123</b>
<b>A</b>	<b>Inlet and outlet control volumes</b>	<b>127</b>
<b>B</b>	<b>Journal bearing reaction forces</b>	<b>131</b>
	<b>Bibliography</b>	<b>133</b>

# List of Figures

1.1	Single chambre vane pump. . . . .	2
1.2	Double chambre vane pump. . . . .	2
1.3	Variable displacement vane pump. . . . .	3
1.4	Flow chart of an ideal modeling process. . . . .	3
2.1	Vane pumps sorting. . . . .	10
2.2	The two extreme working conditions: full flow (a) and zero flow (b). . . . .	10
2.3	Variable displacement vane pump main components: casing (1), one piece rotor shaft (2), vane (3), pressure ring (stator) (4), balancing screw (5), control piston (6), bias piston (7), tuning screws (8, 9). . . . .	11
2.4	The pressure device compensator in full flow condition (a) and in zero flow condition (b). . . . .	12
2.5	Variable displacement vane pump characteristic curve. . . . .	13
2.6	Angular coordinate at the beginning of the trapped volume . . .	13
2.7	Two typical designs for the vane-stator coupling: an old solution (a) and a new solution to minimize wear due to the contact between the vane head and the stator (b). . . . .	14
2.8	Pump <i>PHV 05</i> main components. . . . .	15
2.9	Pump <i>PHV 05</i> cross section. . . . .	16
2.10	Pump <i>PHV 05</i> blow up. . . . .	18
2.11	Pump <i>PHV 05</i> characteristic curve. . . . .	19
2.12	Pump <i>PHV 05</i> drainage flow rate rage. . . . .	19
2.13	Port plate design. . . . .	20
2.14	Port plate section. . . . .	20
2.15	The rotor design. . . . .	21
2.16	Pressure ring cross section. . . . .	21
2.17	The vane design. . . . .	22
2.18	The test bench apparatus. . . . .	22
2.19	The modified rotor shaft used for the tests. . . . .	22
2.20	The pressure measured in a vane space (solid line) and in a hole (dash-dot line) for a complete shaft rotation in the full flow rate condition corresponding to the cutoff pressure. . . . .	23
2.21	The pressure measured in a vane space (solid line) and in a hole (dash-dot line) for a complete shaft rotation in the zero flow rate condition, corresponding to the dead head pressure. . . . .	23
3.1	Model for the dynamic analysis of the rotor shaft. . . . .	25

---

3.2	The main pump components, the inlet control volumes ( $V_{24}$ , $V_{26}$ ) and outlet control volume ( $V_{23}$ , $V_{25}$ ). . . . .	27
3.3	The control volumes on a $xy$ plane. . . . .	28
3.4	The laminar flow rates for a vane space and for a hole on a $xy$ plane. . . . .	29
3.5	A general scheme of a laminar flow. . . . .	29
3.6	The turbulent flow rate for a vane space and for a hole. . . . .	30
3.7	A general scheme of a turbulent flow. . . . .	30
3.8	The tangential velocities involved in drag flow calculation. . . . .	31
3.9	Ducts between external and internal distribution. . . . .	33
3.10	Geometry considered for the shaft displacement calculation. . . . .	38
3.11	Geometry scheme for the shaft displacement calculation. . . . .	39
3.12	Geometrical scheme used to compute distance between rotor center and pressure ring inner race. . . . .	40
3.13	The volume of a vane space. . . . .	41
3.14	The hole geometry on a $xy$ plane. . . . .	43
3.15	Angular region for passage area calculation. . . . .	43
3.16	The angular coordinate for passage area calculation. . . . .	44
3.17	Passage area in the carving region. . . . .	45
3.18	Passage area at the beginning of distribution ducts. . . . .	46
3.19	Passage area at the beginning of duct constant area region. . . . .	47
3.20	Passage area between the vane space $V_1$ and port plate ducts for a complete shaft rotation. . . . .	47
3.21	Angular regions for the inner distribution. . . . .	48
3.22	The inner exchange area. . . . .	49
3.23	Passage area between the hole corresponding to control volume $V_{12}$ and port plate ducts for a complete shaft rotation. . . . .	50
3.24	Generic geometry used to compute the forces on the rotor shaft. . . . .	51
3.25	The force components taken into account in the calculation of the dorce acting on the rotor shaft: force due to the pressure evolution in a vane space (a), force due to the pressure evolution in a hole (b), force due to the action of the pressure field on a vane, forces acting on a vane in radial direction. . . . .	53
3.26	Journal bearing scheme, $P$ is the journal center, $O$ is the bearing center. $\bar{\mu}_\epsilon$ and $\bar{\mu}_\Gamma$ are the unit vector along and normal the eccentricity $\tilde{e}$ . . . . .	54
3.27	Kinematic variables in the journal bearing impedance method. . . . .	54
3.28	The coupling between rotor flanks and port plates. . . . .	58
3.29	The rotor shaft. . . . .	59
3.30	Pressure and force calculation loop. . . . .	60
3.31	The <i>SEP</i> position with respect to journal bearing radial clearance (a) and the shaft orbit around the <i>SEP</i> (b). . . . .	61
3.32	The constraint condition 1 (a), the constraint condition 2 (b) and the constraint condition 3 (c). . . . .	63
3.33	The rotor shaft deflection and the journal bearing in constraint condition 1. . . . .	64
3.34	The cylindrical constraints used for the finite element dynamical analysis. . . . .	64
3.35	The meshed geometry used for the finite element dynamical analysis. . . . .	65

---

3.36	The first flexural mode (13838 Hz). . . . .	65
3.37	The second flexural mode (16486 Hz). . . . .	66
4.1	Simulink flow chart of the rotor shaft equilibrium problem. The model file is called <i>rotor_equilibrium_look_up.mdl</i> . . . . .	68
4.2	Detail of <i>rotor_equilibrium_look_up.mdl</i> : the integrators. . . . .	69
4.3	Integration parameters in the Simulink dialog box. . . . .	69
4.4	Detail of <i>rotor_equilibrium_look_up.mdl</i> : a passage for the motor drive torque calculation. . . . .	70
4.5	Detail of <i>rotor_equilibrium_look_up.mdl</i> : the periodic time calculation. . . . .	70
4.6	The periodic time calculated by the block of Figure 4.5. . . . .	71
4.7	The input data for the models (p. 1). . . . .	72
4.8	The input data for the models (p. 2). . . . .	73
4.9	The input data for the models (p. 3). . . . .	74
4.10	The input data for the models (p. 4). . . . .	75
4.11	The input data for the models (p. 5). . . . .	76
4.12	The script <i>system_26.m</i> syntax (p. 1). . . . .	78
4.13	The script <i>system_26.m</i> syntax (p. 2). . . . .	79
4.14	The script <i>rotor_dyn_force.m</i> syntax (p. 1). . . . .	80
4.15	The script <i>rotor_dyn_force.m</i> syntax (p. 2). . . . .	81
4.16	The <i>full_model.m</i> syntax. . . . .	82
5.1	The pump <i>PHV05</i> on the test bench in normal configuration (on the left) in with the modified cover and measurements devices (on the right). . . . .	85
5.2	The pump <i>PHV05</i> modified to perform experimental measurements in working condition. . . . .	85
5.3	Pressure evolution in the full flow condition in a vane space (solid line) and in a hole control volume (dash-dot line). . . . .	85
5.4	Pressure evolution in the zero flow condition in a vane space (solid line) and in a hole control volume (dash-dot line). . . . .	86
5.5	The drainage flow rate (blue line) and the outlet flow rate (red line). . . . .	86
5.6	Motor torque variation (red line) from the full flow condition to the zero flow condition (see blue line). . . . .	87
5.7	Radial pressure forces acting on the pump casing. . . . .	88
5.8	Forces acting on the pressure ring due to centrifugal actions relative to lubricant ( $\mathbf{F}_{co,i}$ ) and vane ( $\mathbf{F}_{cv,i}$ ). . . . .	89
5.9	Force acting on the pressure ring in the full flow condition: $x$ component (solid line), $y$ component (dash-dot line), total force (dashed line). . . . .	90
5.10	Force acting on the pressure ring in the zero flow condition: $x$ component (solid line), $y$ component (dash-dot line), total force (dashed line). . . . .	90
5.11	Force acting on the rotor in the full flow condition: $x$ component (solid line), $y$ component (dash-dot line), total force (dashed line). . . . .	91
5.12	Force acting on the rotor in the zero flow condition: $x$ component (solid line), $y$ component (dash-dot line), total force (dashed line). . . . .	91

---

5.13	Spectrum of the total force acting on the pressure ring in full flow condition. . . . .	92
5.14	Measurement points on the pressure ring, direction $-y$ ( $A$ ); on the pressure ring, direction $-x$ ( $B$ ); on the journal bearing cover side ( $C$ ) and on the journal bearing, motor side ( $D$ ). . . . .	93
5.15	Detail of accelerometers mounted on the journal bearing, motor side, point $D$ (a) on the pressure ring, $-y$ direction, point $A$ and $-x$ direction, point $B$ (b). . . . .	94
5.16	Excitation points on the pump casing. . . . .	94
5.17	Power spectrum density ( $PSD$ ) of all the hammer blows. . . . .	94
5.18	The sealing on the rotor shaft hole used to realize the passage of the accelerometers cables. . . . .	95
5.19	Frequency response function obtained exciting the pump casing in point 1 and measuring the acceleration in point $A$ . . . . .	95
5.20	The accelerometers placed on the pump casing. . . . .	97
5.21	Time synchronous average of the acceleration signal acquired in correspondence of point 3 (see Figure 5.20). . . . .	97
5.22	Frequency spectrum of the time synchronous average signal depicted in Figure 5.21. . . . .	98
5.23	Comparison between pressure measured in working conditions (dash-dot line) and pressure calculated by the lumped parameter model (solid line) in the full flow condition for a vane space. . . . .	99
5.24	Comparison between pressure measured in working conditions (dash-dot line) and pressure calculated by the lumped parameter model (solid line) in the full flow condition for a hole control volume. . . . .	99
5.25	Comparison between pressure measured in working conditions (dash-dot line) and pressure calculated by the lumped parameter model (solid line) in the zero flow condition for a vane space. . . . .	100
5.26	Comparison between pressure measured in working conditions (dash-dot line) and pressure calculated by the lumped parameter model (solid line) in the zero flow condition for a hole control volume. . . . .	100
5.27	Outlet flow rate evolution in the full flow condition. . . . .	101
5.28	Drainage flow rate evolution in the full flow condition. . . . .	102
5.29	Outlet flow rate evolution in the zero flow condition. . . . .	102
5.30	Drainage flow rate evolution in the zero flow condition. . . . .	102
5.31	The motor drive torque evolution on a vane pitch in the full flow condition. . . . .	103
5.32	The motor drive torque evolution on a vane pitch in the zero flow condition. . . . .	104
5.33	Comparison between the forces acting on the pressure ring in working condition (solid line) and the forces calculated by the $LP$ model (dash-dot line) in full flow condition, $x$ direction. . . . .	105
5.34	Comparison between the forces acting on the pressure ring in working condition (solid line) and the forces calculated by the $LP$ model (dash-dot line) in full flow condition, $y$ direction. . . . .	105
5.35	Comparison between the forces acting on the pressure ring in working condition (solid line) and the forces calculated by the $LP$ model (dash-dot line) in zero flow condition, $x$ direction. . . . .	106



---

5.36	Comparison between the forces acting on the pressure ring in working condition (solid line) and the forces calculated by the <i>LP</i> model (dash-dot line) in zero flow condition, <i>y</i> direction. . . . .	106
5.37	Position corresponding to 12 deg after the initial position. . . . .	107
5.38	Comparison between the forces acting on the rotor shaft in working condition (solid line) and the forces calculated by the <i>LP</i> model (dash-dot line) in full flow condition, <i>x</i> direction. . . . .	108
5.39	Comparison between the forces acting on the rotor shaft in working condition (solid line) and the forces calculated by the <i>LP</i> model (dash-dot line) in full flow condition, <i>y</i> direction. . . . .	108
5.40	Comparison between the forces acting on the rotor shaft in working condition (solid line) and the forces calculated by the <i>LP</i> model (dash-dot line) in zero flow condition, <i>x</i> direction. . . . .	109
5.41	Comparison between the forces acting on the rotor shaft in working condition (solid line) and the forces calculated by the <i>LP</i> model (dash-dot line) in zero flow condition, <i>y</i> direction. . . . .	109
5.42	Pump casing accelerations in correspondence of points 1, 2, 3, 4 of Figure 5.20, full flow condition. The black square markers represent experimental accelerations, while the red circular markers represent the calculated accelerations. . . . .	113
5.43	Pump casing accelerations in correspondence of points 1, 2, 3, 4 of Figure 5.20, zero flow condition. The black square markers represent experimental accelerations, while the red circular markers represent the calculated accelerations. . . . .	114
5.44	Comparison between the experimental and the calculated acceleration relative to point 3, in full flow condition (a) and in zero flow condition (b). . . . .	115
6.1	Rotor shaft accelerations in full flow condition, along <i>x</i> direction (a) and <i>y</i> direction (b). . . . .	118
6.2	Control volumes configuration in the angular position corresponding to $\varphi = 1.7$ deg. . . . .	119
6.3	Control volumes configuration in the angular position corresponding to $\varphi = 11.5$ deg. . . . .	119
6.4	Control volumes configuration in the angular position corresponding to $\varphi = 22.2$ deg. . . . .	120
6.5	Control volumes configuration in the angular position corresponding to $\varphi = 24.5$ deg. . . . .	120
6.6	Control volumes configuration in the angular position corresponding to $\varphi = 31.4$ deg. . . . .	121
6.7	Rotor shaft accelerations in zero flow condition, along <i>x</i> direction (a) and <i>y</i> direction (b). . . . .	122
A.1	The outlet control volume shape ( $V_{23}$ ). . . . .	127
A.2	The inlet control volume shape ( $V_{24}$ ). . . . .	128
A.3	The inner outlet control volume shape ( $V_{25}$ ). . . . .	128
A.4	The inner inlet control volume shape ( $V_{26}$ ). . . . .	129
B.1	Journal bearing reaction force in the full flow condition. . . . .	131
B.2	Journal bearing reaction force in the zero flow condition. . . . .	132



# List of Tables

2.1	Pump <i>PHV 05</i> main design features. . . . .	15
2.2	Pump <i>PHV 05</i> port plate design data. . . . .	16
2.3	Pump <i>PHV 05</i> pressure ring and rotor geometry features. . . . .	17
2.4	Pump <i>PHV 05</i> vane geometry features. . . . .	17
2.5	Pump <i>PHV 05</i> main clearances values. . . . .	18
2.6	Lubricant <i>Shel Tellus ST 46</i> main features. . . . .	18
3.1	Deflection angle in correspondence of constraints. . . . .	62
3.2	Finite element dynamic simulation parameters. . . . .	62
4.1	Initial conditions in terms of displacements and velocities for the integration of the rotor shaft equilibrium problem. . . . .	69
5.1	Instrumentation used during the <i>FRF</i> measurements. . . . .	93
5.2	Acceleration measurements in working conditions. . . . .	96
5.3	Order tracking parameters. . . . .	97
5.4	PGP values for the pressure evolutions in a vane space and in a hole control volume, for the full flow and zero flow condition ( $\delta = 3\%$ ). . . . .	99
5.5	Drainage and outlet flow rate values. . . . .	101
5.6	Motor drive torque in full flow and zero flow condition. . . . .	103
5.7	Comparison between the <i>RMS</i> statistical parameter applied to measured and calculated accelerations signals. . . . .	112
6.1	Main dynamical phenomena and time when they take place in percentage of the vane pitch. . . . .	118
A.1	Volume amount of inlet and outlet ducts. . . . .	127



# List of Symbols

$\Delta\varphi$	Angular step [deg]
$\eta_c$	Carving slope [deg]
$\eta_{vh}$	Vane head slope [mm]
$\gamma_T$	Proportional damping factor [s]
$\mu$	Lubricant dynamic viscosity [Pa·s]
$\mu_f$	Friction coefficient between vane head and pressure ring inner race
$\omega$	Angular velocity [rad/s]
$\phi$	Current angular coordinate used to calculate the passage area [deg]
$\rho$	Lubricant density [kg/m <sup>3</sup> ]
$\theta_c$	Carving splay [deg]
$\varphi$	Angular coordinate [deg]
$\varphi_0$	Input angular coordinate for the rotor dynamic equilibrium model
$\varphi_{tvb}$	Vane angular extension [deg]
$\varphi_{vp}$	Vane pitch [deg]
$A_i(\varphi)$	Passage area for control volume $i$ [m <sup>2</sup> ]
$A_v(\varphi^*)$	Frontal area of the trapped volume [mm <sup>2</sup> ]
$A_{23,i}$	Exchange area between control volume $i$ and outlet duct [mm <sup>2</sup> ]
$A_{24,i}$	Exchange area between control volume $i$ and inlet duct [mm <sup>2</sup> ]
$A_{25,i}$	Exchange area between control volume $i$ and inner outlet duct [mm <sup>2</sup> ]
$A_{26,i}$	Exchange area between control volume $i$ and inner inlet duct [mm <sup>2</sup> ]
$A_{duct}$	Area of ducts between internal and external distribution volumes [mm <sup>2</sup> ]
$A_{inlet}$	Inlet duct interface area [mm <sup>2</sup> ]
$A_{outlet}$	Outlet duct interface area [mm <sup>2</sup> ]

---

$a_{p,dir}$	Pump casing acceleration in correspondence of point $p$ , along the direction $dir$ [m/s <sup>2</sup> ]
$b_c$	Carving base width [mm]
$b_i(\varphi)$	Meatus width [mm]
$b_f$	Width of the meatus between vane flank and port plates [mm]
$b_{hr}$	Width of the meatus between rotor and port plates, starting from hole control volume [mm]
$b_h$	Width of the meatus between vane and rotor groove [mm]
$B_{oil}$	Lubricant bulk modulus [Pa]
$b_r$	Width of the meatus between rotor and port plates [mm]
$b_s$	Width of the meatus between pressure ring and port plates [mm]
$C_r$	Radial clearance in the journal bearing [mm]
$C_T$	Test bench shaft proportional damping [Nm/rads]
$D$	Actual displacement [cm <sup>3</sup> /rev]
$d_b$	Journal bearing diameter [mm]
$d_d$	Duct between internal and external distribution diameter [mm]
$e$	Stator eccentricity [mm]
$e_f$	Component of the eccentricity between rotor and pressure ring inner race due to shaft displacement [mm]
$e_i$	Imposed eccentricity between rotor and pressure ring [mm]
$e_{sep}$	Component of the eccentricity between rotor and pressure ring inner race due to journal bearings behavior [mm]
$e_{tot}$	Total eccentricity between rotor center and pressure ring inner race [mm]
$f$	Shaft displacement [mm]
$f_b$	Journal bearing friction coefficient
$F_{b,x}$	Journal bearing force reaction in $x$ direction [N]
$F_{b,y}$	Journal bearing force reaction in $y$ direction [N]
$F_{co,i}(\varphi)$	Force on the pressure ring due to centrifugal acceleration of lubricant in control volume $i$ [N]
$F_{fv,i}(\varphi)$	Force acting on the pressure ring due to the contact force between vane $i$ and pressure ring [N]
$F_{hr,i}(\varphi)$	Force acting on the rotor shaft due to pressure in the generic hole $i$ [N]
$F_{rotor}(\varphi)$	Force acting on the rotor shaft [N]

---

$F_{sr,i}(\varphi)$	Force acting on the rotor shaft due to pressure in the generic vane space $i$ [N]
$F_{stator}(\varphi)$	Force acting on the pressure ring [N]
$F_{vh,i}(\varphi)$	Contact force between vane $i$ and pressure ring [N]
$F_{vr,i}(\varphi)$	Force acting on the rotor shaft due to pressure in the generic vane space $i$ [N]
$F_{vr,i}(\varphi)$	Force acting on the rotor shaft due to the action of the pressure field on the generic vane $i$ [N]
$G$	Shear modulus [GPa]
$h_c$	Carving depth [mm]
$h_d$	Clearance between rotor and distributor [mm]
$h_f$	Clearance between vane flank and port plate [mm]
$h_g$	Clearance between a vane and a rotor groove [mm]
$h_i(\varphi)$	Meatus thickness [mm]
$h_p$	Port plate thickness [mm]
$h_v$	Vane height [mm]
$h_{hr}$	Thickness of the meatus between rotor and port plates, starting from hole control volume [mm]
$h_h$	Thickness of the meatus between a vane and rotor groove [mm]
$H_{out,in}$	Frequency response function with input in $in$ and output in $out$ [(m/s <sup>2</sup> )/N]
$h_{rg}$	Distance between the vane bottom and the rotor [mm]
$h_r$	Thickness of the meatus between rotor and port plates [mm]
$h_s$	Thickness of the meatus between pressure ring and port plates [mm]
$I$	Polar moment of inertia of the shaft [m <sup>4</sup> ]
$i$	Subscript denoting control volumes
$J$	Rotating parts polar moment of inertia [kg m <sup>2</sup> ]
$j$	Subscript denoting control volume in communication with control volume $i$
$k$	Flow coefficient
$K_T$	Test bench shaft torsional stiffness [Nm/rad]
$L(\varphi)$	Distance between rotor center and stator inner race [mm]
$l_c$	Carving length [mm]

---

$l_i(\varphi)$	Length of a generic laminar meatus [mm]
$l_f$	Length of the meatus between vane flank and port plates [mm]
$l_{hr}$	Length of the meatus between rotor and port plates, starting from hole control volume [mm]
$l_h$	Length of the meatus between vane and rotor groove [mm]
$l_r$	Length of the meatus between rotor and port plates [mm]
$l_s$	Length of the meatus between pressure ring and port plates [mm]
$m$	Rotating parts mass [kg]
$M_m$	Motor drive torque [Nm]
$M_p(\varphi)$	Torque due to pressure distribution [Nm]
$m_v$	Mass of a vane [kg]
$M_{vd}$	Torque due to viscous actions [Nm]
$M_{vh}(\varphi)$	Torque due to friction between vane head and pressure ring [Nm]
$N$	Number of vanes
$p$	Pressure [Pa]
$p^*$	Normalized pressure
$p^0$	First trial pressure [Pa]
$p_{drain}$	Drainage pressure [Pa]
$p_{in}$	Inlet pressure [Pa]
$p_{out}$	Outlet pressure [Pa]
$PGP$	Percentage of good points index [%]
$Q_i$	Generic flow rate for the control volume $i$ [m <sup>3</sup> /s]
$Q_{drag}$	Drag flow rate for vane spaces [m <sup>3</sup> /s]
$Q_{drain}$	Drainage flow rate [m <sup>3</sup> /s]
$Q_{exp}$	Theoretical outlet flow rate [m <sup>3</sup> /s]
$Q_{hd}$	Drainage flow rate for holes [m <sup>3</sup> /s]
$Q_{ht}$	Turbulent flow rate between holes and distribution ducts [m <sup>3</sup> /s]
$Q_{inlet}$	Inlet flow rate [m <sup>3</sup> /s]
$Q_{lam,i}$	Sum of all the laminar flow rate involved in the $i^{th}$ control volume balance [m <sup>3</sup> /s]
$Q_{outlet}$	Outlet flow rate [m <sup>3</sup> /s]



---

$Q_{td}$	Turbulent flow rate in ducts between external and internal distribution [m <sup>3</sup> /s]
$Q_{vd}$	Laminar flow between the rotor and the port plate for a vane space control volume [m <sup>3</sup> /s]
$Q_{vf}$	Laminar flow rate on a vane flank [m <sup>3</sup> /s]
$Q_{vh}$	Laminar flow rate from a vane space to a hole [m <sup>3</sup> /s]
$Q_{vs}$	Drainage flow between the pressure ring and port plates [m <sup>3</sup> /s]
$Q_{vt}$	Turbulent flow rate from a vane space to distribution ducts [m <sup>3</sup> /s]
$R_b$	Bearing radius [mm]
$r_c$	External duct carving radius [mm]
$r_e$	External ducts radius [mm]
$r_i$	Internal ducts radius [mm]
$r_p$	Duct end fillet radius [mm]
$r_r$	Rotor radius [mm]
$r_s$	Shaft radius [mm]
$r_{frg}$	Fillet radius at the end of a rotor groove [mm]
$r_{hr}$	Hole radius [mm]
$r_{ic}$	Internal duct carving radius [mm]
$r_{se}$	Pressure ring external radius [mm]
$r_{si}$	Pressure ring inner radius [mm]
$r_{sr}$	Rotor side radius [mm]
$SEP$	Journal bearing static equilibrium position [mm]
$t_{vb}$	Vane base thickness [mm]
$t_{vh}$	Vane head thickness [mm]
$temp$	Lubricant temperature [°C]
$u$	Tangential velocity [m/s]
$V_h$	Generic hole volume [m <sup>3</sup> ]
$V_i$	Generic control volume
$v_s$	Journal bearing squeeze velocity [m/s]
$V_v$	Generic vane volume [m <sup>3</sup> ]
$W$	Journal bearing impedance

---

$W_b$	Journal bearing axial width [mm]
$W_c$	Carving width [mm]
$W_p$	Rotor and pressure ring common width [mm]
$W_r$	Rotor width [mm]
$W_s$	Pressure ring width [mm]
$W_v$	Vane width [mm]
$W_{sr}$	Rotor side width [mm]
$x$	Rotor shaft degree of freedom corresponding to horizontal direction
$y$	Rotor shaft degree of freedom corresponding to vertical direction
$z$	Rotor shaft degree of freedom corresponding to axial direction

# Chapter 1

## Introduction

*In this introductory section a general overview of the present study will be provided. Dealing with high pressure variable displacement vane pumps great attention must be paid to all the dynamic phenomena taking place inside such machinery. For this reason several advanced modeling techniques have been developed and used. The basic theory, the applications and the results of these models will be reported in the present work following the scheme underlined hereafter.*

### 1.1 Variable displacement vane pumps peculiarities

Vane pumps are a particular kind of positive displacement pumps (*PD*), in which a unit of fluid is physically transferred from an inlet region to an outlet region. In the family of *PD* pumps, vane pumps can be classified as rotary pumps. With respect to alternative pumps, this category will produce a smoother and more continuous flow, while alternative pumps will lead to a pulsed flow. Between vane pumps it is possible to distinguish three subfamilies [1]:

- Single chamber vane pumps: they use an eccentric circular pressure ring that allows to obtain for each vane space a single cycle from inlet to outlet pressure per rotor revolution;
- Double chamber vane pumps: they use an elliptical pressure ring characterized by a double eccentricity that allows to obtain for each vane space a double cycle from inlet to outlet pressure per rotor revolution;
- Variable displacement vane pumps: in this kind of vane pumps a circular pressure ring can vary its eccentricity with respect to the rotor shaft.

The three items previously listed are respectively depicted in Figures 1.1, 1.2, 1.3, where the inlet region is represented in blue, while the outlet region in red. The pump studied in this thesis is a variable displacement high pressure vane pump. This kind of *PD* pump is widely used in machine tools and in hydraulic systems thanks to its control strategy. In fact the lubricant flow rate can be

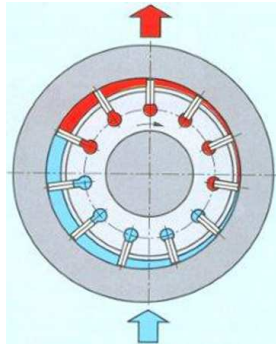


Figure 1.1: Single chambre vane pump.

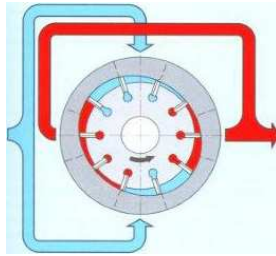


Figure 1.2: Double chambre vane pump.

simply tuned accordingly to system and efficiency requirements by varying the relative eccentricity between pressure ring and rotor shaft. In this way the pump elaborates only the required flow rate allowing to save energy. This main feature leads to select a variable displacement vane pump for all the applications in which the plant needs to be kept at working pressure by compensating the plant losses and only occasionally a flow rate is required to move tools mounted on the lyne. This is the typical case of a machine tool, i. e. a drill, that usually stands still, only when the tool start to be used the variable displacement vane pump starts to elaborate the required flow rate. As a machine tool component, the pump being studied must provide low vibration and acoustic levels to ensure high working precision as well as health and comfort of technicians. In this sight, an optimization process must be performed to reduce vibration levels and noise emissions. This optimization process is based on advanced modeling techniques as described hereafter.

## 1.2 Modeling mechanical systems

Modeling a complex mechanical system is often an hard task, in fact a complete knowledge of the system is required to avoid mistakes and errors, a coherent formulation of the problem must be done and finally the mathematical formulation must be implemented in an efficient and smart way. Let us consider separately all this step resumed in the flow chart of Figure 1.4 [2]. In more detail, the mechanical system to be studied will be analyzed in Chapter 2, the physical

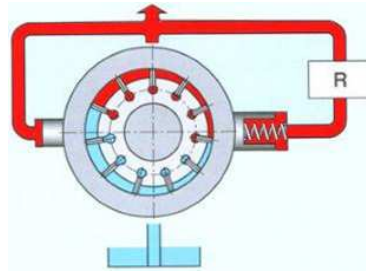


Figure 1.3: Variable displacement vane pump.

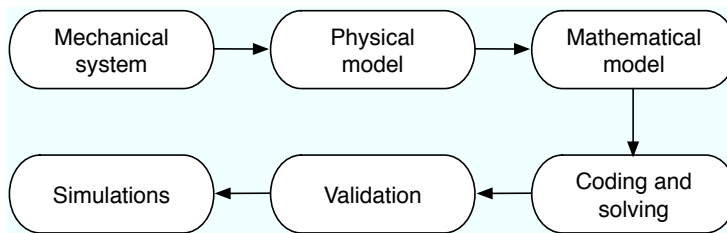


Figure 1.4: Flow chart of an ideal modeling process.

model and the mathematical formulation will be treated in Chapter 3, the main aspects of the implementation will be described in Chapter 4, the validation procedure will be reported in Chapter 5 and finally an example of application will be summarized in Chapter 6.

### 1.2.1 Physical model

Usually the physical model represents an equivalent system of the actual mechanical system under some hypotheses:

- The distributed characteristics (e.g. density, stiffness, damping, etc) are replaced with lumped characteristics;
- When possible the system behavior is supposed to be linear;
- The system parameters are not time-varying;
- The uncertainties are neglected.

The physical model built up depends on the kind of analysis that has to be performed. For example to study the pump *PHV 05* a kyneto-elastodynamic model has been developed. Using such an approach, the properties of the system in terms of mass, stiffness and dumping are considered as *Lumped Parameters*, for this reason it is called *LP* model.

### 1.2.2 Mathematical model

This kind of *LP* model can be generally represented by means of the second order system of differential equations (1.1):

$$[M]\ddot{\bar{x}} + [C]\dot{\bar{x}} + [K]\bar{x} = \bar{F}(t) \quad (1.1)$$

where  $[M]$ ,  $[C]$  and  $[K]$  represents the mass, the viscous damping and the stiffness of the system and  $\bar{F}(t)$  is the external force field applied to the system, while  $\ddot{\bar{x}}$ ,  $\dot{\bar{x}}$  and  $\bar{x}$  are respectively the vectors of accelerations, velocities and displacements.

In the case of volumetric pumps, the force calculation can be generalized as stated in equation (1.2), where  $s_i$  is the generic surface in which the pressure  $p_i$  is acting.

$$F_i = \int p_i ds_i \quad (1.2)$$

For this reason a deep characterization of the pressure field is required because quantity  $\bar{F}(t)$  in equation (1.1) can be determined once the pressure evolution around the rotor shaft is calculated. The pressure field calculation involves the solution of a first order differential equation system whose equations can be written in a general way as follows:

$$\frac{dp_i}{d\varphi} = f(p) \quad (1.3)$$

Where  $p_i$  represents the pressure evolution in a generic control volume and  $p$  represents the whole pressure field to be calculated.

### 1.2.3 Integration

The system of first order differential non linear equations, with non constant coefficients describing the pressure field is an example of stiff problem. To solve it, a variable order solver, based on the numerical differentiation formulas (NDFs) has been used. The algorithm is an explicit Runge-Kutta variable step formulas for stiff initial values problems (IVPs) [3]. On the other hand, dealing with the rotor shaft equilibrium system solution, also fixed step solvers can be used. In this case the solution is easier and faster because the problem is non-stiff and it is described by few equations.

## 1.3 Variable displacement vane pump: state of the art and modeling

When dealing with variable displacement vane pumps, the use of models is suitable to investigate and optimize several aspects related to working condition. In particular, since this kind of pumps often equips machine tools, great importance is given to the optimization of the vibrational behavior to ensure high working precision as well as comfort of technicians.

The first step in order to simulate the pump dynamic behavior is the development of a dynamic model of the rotating parts. A *Lumped Parameter (LP)*

model is generally considered for this purpose: this approach consists in considering all the inertia, the stiffness and the damping properties as lumped. An example of this method applied to gear pumps can be found in [2, 4–6] that are taken as starting point in this study. Then, once the loads in terms of pressure forces and torques are known, it is possible to integrate the equations of motion obtaining the rotating part accelerations as well as the bearing force reactions. In the above mentioned works, these bearing reactions are calculated by a non linear algorithm based on the finite impedance theory [7].

As stated before, the determination of loads in terms of pressure forces and torques is required for the integration of the equations of motion involved in the *LP* model of the rotor shaft equilibrium. These loads are a function of the pressure field inside the pump that is the first aspect to be studied in a proper pump modeling process. As a matter of fact, all the variable forces acting on the pump casing are due to variations in the pressure field. Hence in the frame of a noise and vibration optimization the reduction of pressure ripple is crucially important because this phenomenon generates variable forces and finally body vibrations. An attempt to investigate and minimize the ripple phenomena has been described by Hattori et al. [8]. This work is based on the study of the pump by means of an Euler’s approach, as proposed in [9–13]. Using this modeling technique, the pump fluid domain is divided in several control volumes; hence, the flow rate continuity equation can be applied to each control volume. The pressure field and the flow rates that characterize the pump can be finally obtained by integrating the system of flow rate continuity equations.

Once the pressure field is determined, it is possible to calculate the main excitation forces that load the pump components. Dealing with this fundamental calculation, several works have been performed by Fiebig and Heisel [13], Mancò et al. [14], Gellrich et al. [15] and Novi et al. [16]. In all the above mentioned works, the force calculation is performed to study wear phenomena taking place inside the pump and mainly deals with the calculation of contact forces between the vane head and the pressure ring.

Another important step in modeling a variable displacement vane pumps is the validation procedure used to assess the pressure evolution basing on the comparison between calculated pressures and pressures measured in working condition. Works dealing with this topic have been carried out by Bianchini et al. [17] and Kunz et al. [18].

The results in terms of pressure loads can be combined with *frequency response functions (FRFs)* of the pump casing to calculate the casing accelerations that are the main sources of noise and vibrations. In this way the operational accelerations of the casing can be obtained and compared with accelerations measured in working condition to validate the whole procedure. Such an approach has been used from an acoustical point of view by Dickinson et al. [19]. In a more similar way the same validation method has been exposed by Mucchi et al. in [20], in which *FRFs* simulated by means of a finite element model have been used instead of experimental *FRFs*.

In this context, this works aims at developing tools useful to carry out a noise and vibration optimization by considering all the approaches underlined in the state of the art outlined above. In more detail, the model developed in this thesis can be used for the analysis of the dynamic behavior of the rotor shaft. It is a simple, but non-linear, model taking into account only the transversal

plane dynamics of the rotor shaft. In addition to the pressure forces and torque, the dynamic equilibrium of the rotor shaft includes the non-linear reactions of the hydrodynamic journal bearings, the torsional stiffness and damping of the driving shaft, as well as the friction effects. This model allows to simulate the rotor shaft accelerations, the journal eccentricity and the time variable reactions in the bearings in working condition.

As stated before, the *LP* model includes the evaluation of pressure forces and torques. These quantities are functions of the pressure field, for this reason an algorithm based on an Euler's approach has been developed as well. This algorithm studies the pressure field by dividing the pump fluid domain in several control volumes, hence the flow rate continuity equation can be applied to each control volume. The results of the pressure calculation can be compared with experimental pressure evolution to carry out a first validation.

The assessed pressure evolutions can be used as input data for subroutines devoted to variable pressure forces and torques calculation. These last results are used by the above mentioned *LP* model to integrate the rotor shaft equations of motion to finally calculate the journal bearing reaction forces as well as the rotor shaft accelerations and the journal bearing eccentricity in working condition.

Moreover, the variable pressure and bearing forces evaluated by means of the *LP* model have been combined with frequency response functions of the pump casing, experimentally estimated. In this way the operational accelerations of the casing can be obtained and compared with accelerations measured in working condition to validate the whole procedure.

Finally, once the *LP* model can be considered validated, a study on the calculated rotor shaft acceleration can be performed with the aim at studying the dynamical phenomena related to pump working condition.

All the algorithm useful to carry out the calculations related to the modeling process outlined in the present section have been developed in MATLAB and Simulink environments. The experimental data used for comparisons and validations have been acquired and processed by means of LMS Test.Lab.

## 1.4 Overview of the thesis

In order to achieve the goals listed above (analysis of the behavior of the system, evaluation of the dynamic forces, etc.) the model described in the previous section has been developed and experimentally assessed.

The first step in a proper modeling activity is the full knowledge of the component being studied. For this reason a general description of variable displacement vane pump has been reported in Chapter 2. Hence a complete characterization of pump *PHV 05* produced by *BERARMA s.r.l* (Casalecchio di Reno, Bologna, Italy) has been provided from a geometrical and operational point of view. In this frame great attention has been paid for the components involved in pump working. The port plate geometry has been fully characterized, hence the rotor, the vane and the pressure ring main dimensions have been provided. Furthermore, the clearances between pump components have been determined, whose geometrical features will influence the communications between the control volumes used to compute the pressure evolutions. Finally the lubricant main features have been specified. The model developed in the present work will use as inputs all these data.



In Chapter 3 the *LP* model is presented in depth from a theoretical point of view. First of all the general features of the model are exposed starting from the system of equation of motion that governs the rotor shaft equilibrium. Hence the calculation of all the quantities involved in the system integration is described. In this frame the procedure for pressure evolution calculation is deeply analyzed. This procedure is based on an Euler's approach that allows to determine the pressure field by integrating a system of flow rate continuity equations, each one referred to the control volumes used to discretize the whole fluid domain. Once the pressure evolution has been determined, the variable pressure forces acting on the rotor can be calculated. Hence, the journal bearing reaction forces can be determined basing on the finite impedance formulation. The calculation of torques acting on the rotor shaft has been described as well. Three kind of load torques have been considered: torques due to the pressure evolution inside control volumes; torques due to the friction between the vanes and the pressure ring and torques due to viscous actions. In this sense, the developed lumped parameter model takes into account the most important phenomena taking place inside the pump in working conditions, most of them are non linear and time varying. Finally, for the sake of completeness, a preliminary analysis is reported to asses the goodness of the assumptions used to develop the model.

In Chapter 4 the main problems related to model implementation in MATLAB and Simulink are described and the most interesting code pieces are reported as well. In this frame the integration of the equations of motion characterizing the rotor shaft equilibrium is carried out in Symulink. The whole model has been described with reference to the blocks that constitutes itself. In more detail, the initial conditions choice has been discussed, and the integration strategy as well as the interface between Symulink and MATLAB are explained by means of images depicting the blocks architecture. The main aspects related to the implementation in MATLAB of the subroutines devoted to the pressure evolution, the pressure forces and the torques calculations are discussed. The most interesting pieces of code are attached as well.

In Chapter 5 the method used to assess the *LP* model has been exposed. First of all the measurements performed during the test campaign have been described. A suitably modified pump has been used to measure the pressure evolutions in working condition in all the regions of interest. Tests at different working pressures have been carried out to evaluate the flow rates and the motor drive torques in different working conditions. The method used to calculate the pressure forces from the pressure measurement has been explained, hence, the original procedure used to measure the frequency response functions of the pump casing is reported. Finally, the casing accelerations measurements and processing is briefly explained. The above mentioned experimental data have been used to assess the model. The validation procedure has been carried out on several levels, in this way the goodness of intermediate results is checked as well. In more detail, the calculated pressure evolution has been assessed by using the experimental pressures. The same validation strategy has been applied to validate the flow rates and the torques. Subsequently, the pressure forces calculated by means of an *ad hoc* method applied to experimental and calculated pressures have been compared and discussed. Hence, the above mentioned forces have been combined with the frequency response functions to calculate the pump casing accelerations. This last results is finally assessed by comparison with the experimental accelerations and the results have been discussed as well.

Since the model can be considered globally validated, in Chapter 6 an example of application has been provided. The results in terms of rotor shaft accelerations are used to establish the events related to unwanted dynamical effects. The analysis has been carried out in the two main working conditions.

The final considerations about the whole modeling and experimental activity are finally reported in Chapter 7, devoted to concluding remarks.

Moreover in Appendix A the volume amount and shape of inlet and outlet control volumes are resumed and in Appendix B the journal bearing reaction forces are reported.

## Chapter 2

# General description of a variable displacement vane pump

*The hydraulic pump universe includes a wide choice of volumetric pumps. In this frame it is possible to classify pumps by using several criteria, such as the pressure range in which they work, the way used to obtain the desired displacement, the possibility to vary the displacement. This chapter will focus on the high pressure variable displacement vane pump family, in particular a pump of the series PHV by BERARMA oleodinamica will be fully described. An analysis of the working condition will be provided as well to fully understand the present work.*

### 2.1 Vane pump basic description

A lot of different classifications can be done when dealing with hydraulic pumps [21]. A first classification is based on the working principle and it is shown in Figure 2.1: the *dynamic pumps* give energy to the flow by imparting a velocity amount able to transfer the flow rate from the inlet to the outlet, while pumps based on *positive displacement* traps a fluid volume and physically move it from the inlet to the outlet. Vane pumps belong to the latter category: they are composed by a cast iron body in which a one piece rotor shaft, a pressure ring and two port plates are located. The pressure ring is eccentric with respect to the shaft axis and in this way the volume isolated between two consecutive vanes varies from a maximum value, in correspondence with the inlet port, to a minimum value, in correspondence with the outlet port. Vane pumps with a double pressure chamber can be realized using an elliptical pressure ring and can transport fluid from inlet to outlet two times per revolution. Vane pumps with circular pressure ring have only one pressure chamber and are widely used. Both this kind of vane pumps can not vary their actual displacement in working condition.

Variable displacement van pumps can supply to this task by varying the relative eccentricity between rotor and pressure ring (stator): they can elaborate a *full*

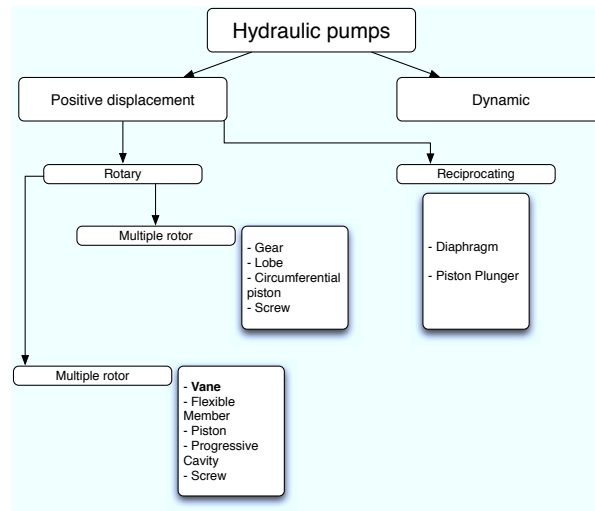


Figure 2.1: Vane pumps sorting.

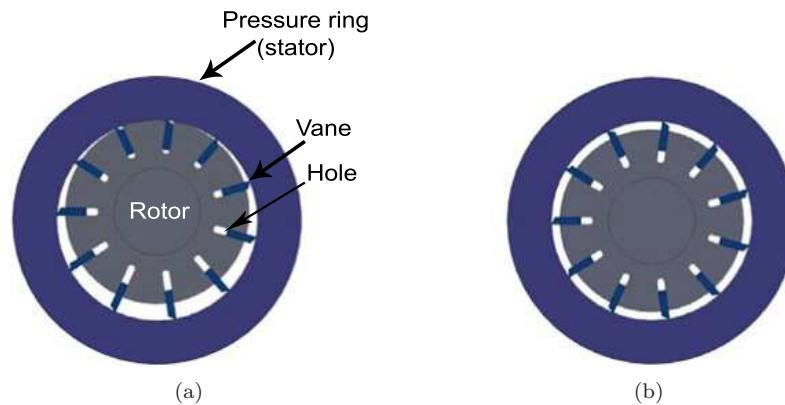


Figure 2.2: The two extreme working conditions: full flow (a) and zero flow (b).

*flow rate* (see Figure 2.2(a)) till the desired pressure level is reached, or they can work in a *zero flow condition* (see Figure 2.2(b)), just to keep the desired pressure by compensating the hydraulic losses. While the *full flow* condition is characterized by the maximum eccentricity between rotor and stator, in the *zero flow* condition there is almost no eccentricity.

The variable displacement vane pump main elements are depicted in Figure 2.3 [22]. The control piston (6) moves the pressure ring changing the pump actual displacement, the bias piston (7) reports the pressure ring in the zero eccentricity condition when the desired pressure level is reached, the balancing screw (5) is used to compensate the main component of the resulting pressure force. The control piston force can be regulated by a tuning screw (8). This mechanical control system can be substituted by an equivalent hydraulic system, called *pressure device compensator*, depicted in Figure 2.4 [23], in which the control piston (2) and the bias piston (3) act on the pressure ring (1) with a

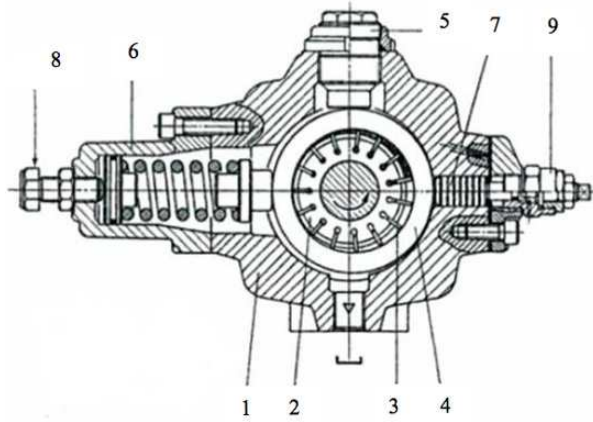


Figure 2.3: Variable displacement vane pump main components: casing (1), one piece rotor shaft (2), vane (3), pressure ring (stator) (4), balancing screw (5), control piston (6), bias piston (7), tuning screws (8, 9).

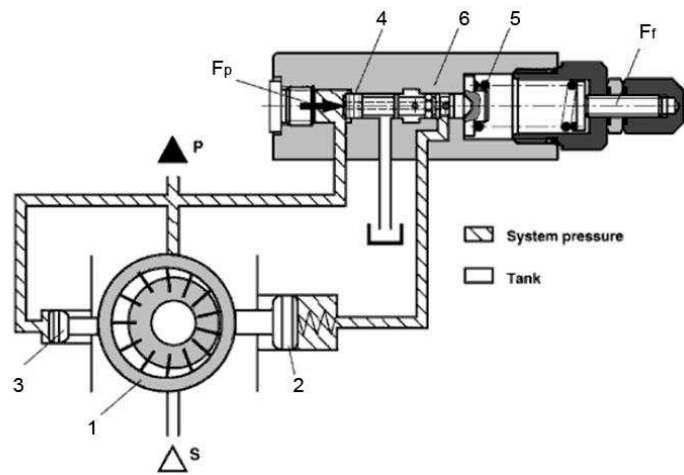
force regulated by the lubricant pressure in the inlet and outlet ducts. In fact, the bias piston is always loaded by the outlet pressure. In the start up phase the control piston is loaded by the outlet pressure as well and his resulting force is bigger than the bias piston one, so it can move the pressure ring to his maximum eccentricity (see Figure 2.4(a)) till the desired pressure level is reached. The compensator spring (5), if compressed, allows the communication between the inlet chamber and the control piston (see Figure 2.4(b)). In this last configuration, the bias piston force is bigger then control piston force and the pressure ring is moved again to zero flow condition: the desired pressure level can now be maintained by using a small power amount.

The characteristic curve of a variable displacement vane pump depicted in Figure 2.5 shows that the maximum eccentricity, corresponding to full flow condition, is maintained till the *cutoff pressure* is reached [24]. The small slope of the first part of the curve is due to hydraulic losses. Once the *cutoff pressure* is reached, the eccentricity (and the flow rate) and the slope of the second part of the curve are determined by the spring stiffness. This procedure can be reversed when the working pressure decreases under the cutoff value. Finally, it can be noticed from Figure 2.5 that the *cutoff pressure* and the *dead head pressure* have almost the same value.

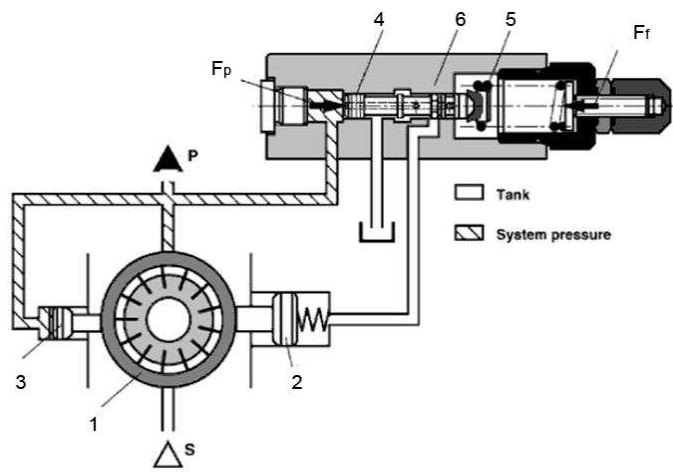
When dealing with vane pumps, one of the most important features is the *actual displacement*: the lubricant volume transferred from inlet to outlet during a revolution of the rotor shaft. It is a function of the volume that each vane space traps after the end of inlet ducts and before the beginning of the outlet ducts. It can be calculated as stated in equation (2.1).

$$D = A_v(\varphi^*)NW_r \quad (2.1)$$

Where, the quantity  $A_v(\varphi^*)$  represents the frontal surface of the trapped vane space at the angular position  $\varphi^*$ ,  $N$  is the number of vanes and  $W_r$  is the rotor width in axial direction. The volume of the trapped vane space depends on design parameters such as external rotor diameter, rotor width in axial direction,



(a)



(b)

Figure 2.4: The pressure device compensator in full flow condition (a) and in zero flow condition (b).

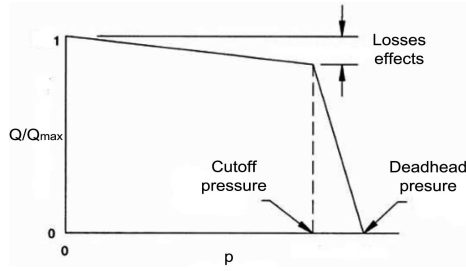


Figure 2.5: Variable displacement vane pump characteristic curve.

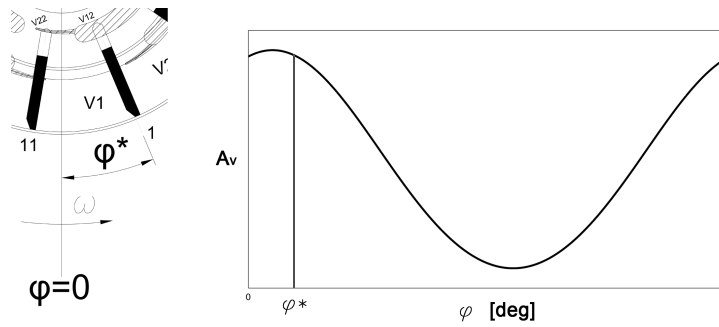


Figure 2.6: Angular coordinate at the beginning of the trapped volume

inner pressure ring diameter, and on the eccentricity between rotor and pressure ring. The procedure to calculate  $D$  consists in determining the evolution of the vane space surface during a revolution ( $A_v$ ), then it is easy to evaluate the quantity  $A_v(\varphi^*)$ . The angular coordinate  $\varphi^*$  is determined as the angular coordinate in which the first vane with respect to the angular velocity  $\omega$  (i.e.  $V_{11}$  in Figure 2.6) passes the inlet duct.

When the design of distributors is unknown, a less accurate estimation of actual displacement can be obtained by considering the trapped vane space as a rectangular surface in correspondence of the maximum eccentricity ( $e_{max}$ ).

$$D = 2\pi r_m e_{max} W_r \quad (2.2)$$

In equation (2.2)  $r_m$  represents the mean radius between the eternal rotor radius and the radius of the inner race of pressure ring, while  $W_r$  represents the rotor width along the axial direction. In this way the displacement is overestimated. The actual displacement depends also on the trapped volume sealing, useful to avoid hydraulic losses inside the pump. The sealing is guarantee by the centrifugal force and by an amount of lubricant at outlet pressure in the vane housing (corresponding to rotor holes). The force acting between the stator inner race and the vane head must be controlled to avoid excessive wear and the contact surface must be designed as well. For this reason a lot of solutions have been proposed, in Figure 2.7 two widely used vane designs are depicted [25].

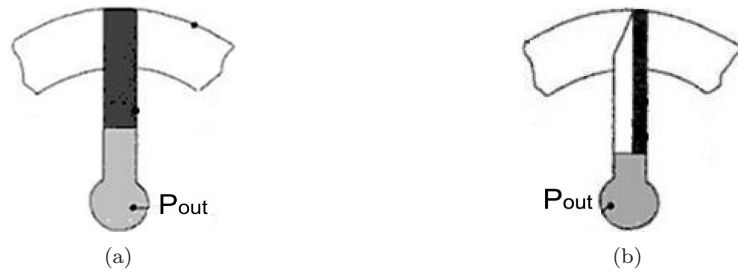


Figure 2.7: Two typical designs for the vane-stator coupling: an old solution (a) and a new solution to minimize wear due to the contact between the vane head and the stator (b).

## 2.2 BERARMA *PHV 05* pump

### 2.2.1 Overview

The pump under study is made by *BERARMA oleodinamica* (Casalecchio di Reno, Bologna, Italy) and belongs to the *PHV* family. The model being studied is the *PHV 05* [26]: it is an high pressure variable displacement vane pump that take advantage of a double inlet/outlet port plate system in which each port is packed on the pressure ring by using a system based on hydrostatic compensation. Such a pump uses a pressure device compensator (described in section 2.1) to vary his actual displacement. The main component shown in Figure 2.3 can now be identified on the *PHV 05* pump (see Figure 2.8, 2.9 and 2.10).

To fully describe the pump *PHV 05*, the flow rate characteristic curve and the drainage flow rate range are provided in Figure 2.11 and 2.12.

### 2.2.2 *PHV 05* design parameters

Before describing the mathematical formulation of the model (see next chapter), it is useful to define the geometry of the vane pump and the reference frame used. The displacement of the rotor in axial direction has been neglected as well as the pressure variation in axial direction. Therefore the geometry taken into account is a plane geometry, orthogonal to the shaft axis direction. Nevertheless, to avoid misunderstanding it is important to impose a 3-dimensional coordinate system (see Figure 2.8 and 2.9): the  $z$  axis identifies the shaft direction, while the  $xy$  plane defines a rotor shaft cross section. The angular coordinate  $\varphi$  start to be computed in correspondence of the  $-y$  axis, with positive verse in the angular velocity direction. The main design data are listed in table 2.1 [26]. The port plate design is crucially important in determining a proper pump behavior. Figure 2.13 and 2.14 depict the meaning of the most important design parameters and Table 2.2 resumes their values.

As stated in section 2.1, in this kind of pumps the actual displacement as well as the outlet flow rate can be defined with respect to rotor and pressure ring geometry, respectively depicted in Figure 2.15 and 2.16, whose main geometrical features are defined in 2.3.



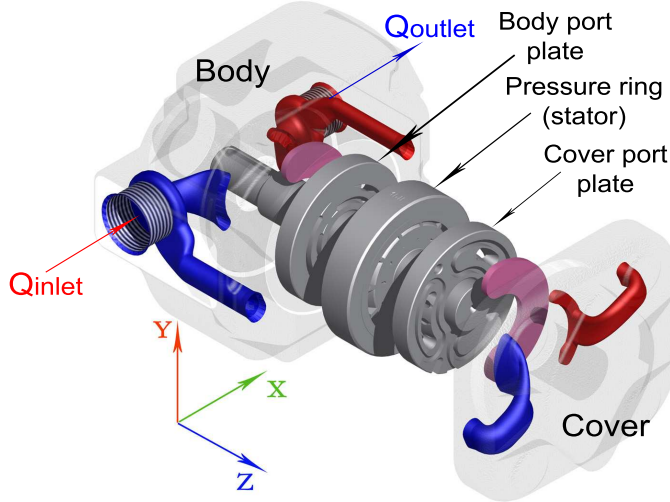


Figure 2.8: Pump *PHV 05* main components.

Table 2.1: Pump *PHV 05* main design features.

Actual displacement (ISO 3662)	16 cm <sup>3</sup> /rev
Max working pressure allowed	250 bar
Max drainage pressure allowed	1 bar
Inlet pressure ( $p_{in}$ )	0.8 ÷ 1.5 bar
Rotational velocity	1350 ÷ 1500 rpm

Finally, to fully define the main components, the vane geometry has to be characterized (see Figure 2.17 and Table 2.4).

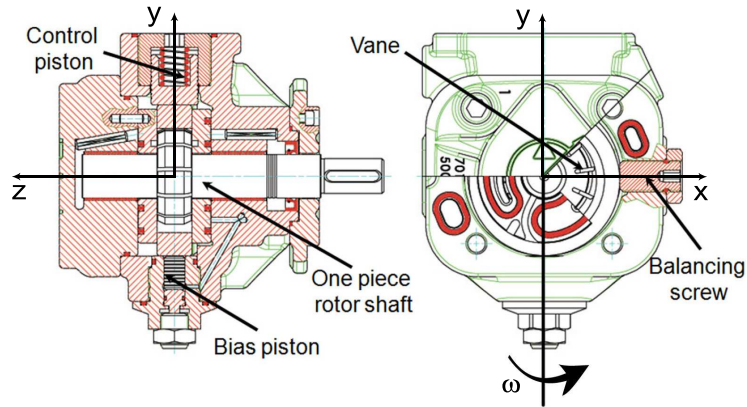
To complete the geometry description, also the geometrical clearances have to be taken into account. This aspect is capitally important when dealing with high pressure pumps because the flow rates taking place inside the clearances are not negligible in a proper model construction. Table 2.5 resumes the main clearances values.

The pump *PHV05* has been tested using the lubricant *Shel Tellus ST46* whose main features are reported in Table 2.6

For the sake of completeness in Appendix A, the distribution ducts are characterized in terms of shape and volumes.

## 2.3 Working condition description

This kind of pump is widely used for applications in machine tools tanks to the possibility to regulate the flow rate accordingly to the system requests. In this way it is possible to minimize hydraulic losses by elaborating only the strictly necessary flow rate. Such a machine typically needs to be kept at working pressure also when there is no request of torque and motion. In this case the variable displacement vane pump works in zero flow condition (see Figure 2.2(b))

Figure 2.9: Pump *PHV 05* cross section.Table 2.2: Pump *PHV 05* port plate design data.

$h_c$	Carving depth	3.5 mm
$\theta_c$	Carving splay	60 deg
$b_c$	Carving base width	0.2 mm
$r_i$	Internal ducts radius	18.7 mm
$r_e$	External ducts radius	25.8 mm
$r_p$	Duct end radius	1.75 mm
$\varphi_{seo}$	External outlet start angle	28 deg
$\varphi_{eeo}$	External outlet end angle	168 deg
$\varphi_{sei}$	External inlet start angle	203 deg
$\varphi_{eei}$	External inlet end angle	353 deg
$\varphi_{sio}$	Internal outlet start angle	343 deg
$\varphi_{eio}$	Internal outlet end angle	194 deg
$\varphi_{sii}$	Internal inlet start angle	225 deg
$\varphi_{eio}$	Internal inlet end angle	330.5 deg

just to compensate the circuit hydraulic losses. When the torque and motion are needed to accomplish the work, the compensator device automatically moves the pressure ring generating the displacement needed to supply the request, till the full flow condition (see Figure 2.2(a)). Of course the pump can work also in intermediate conditions when the pressure ring eccentricity value is less than the biggest allowed. Nevertheless, Figure 2.5 shows that intermediate working conditions are negligible because of the fast passage from the cutoff pressure to the dead head pressure. For this reason the tests have been carried out mainly in full flow or zero flow condition.

To study the working condition behavior, a test bench has been used (see Figure 2.18). The experimental rig allows to measure the pressure inside a vane space and inside a hole for a complete shaft rotation by means of piezoelectric transducers directly placed on the one piece rotor shaft. To do this, a suitably designed rotor shaft is used (see Figure 2.19) in which two meatus connect a vane space and a hole to the end of the shaft, where two pressure transducers

Table 2.3: Pump *PHV 05* pressure ring and rotor geometry features.

$W_r$	Rotor width	20 mm
$r_r$	Rotor radius	27.5 mm
$r_{hr}$	Hole radius	18.3 mm
$r_{sr}$	Rotor side radius	25.5 mm
$W_{sr}$	Rotor side width	4.5 mm
$W_s$	Pressure ring width	20 mm
$r_{se}$	Pressure ring external radius	86.5 mm
$r_{si}$	Pressure ring inner radius	30 mm

Table 2.4: Pump *PHV 05* vane geometry features.

$h_v$	Vane heigh	8.8 mm
$W_v$	Vane width	20 mm
$t_{vh}$	Vane head thickness	0.2 mm
$t_{vb}$	Vane base thickness	2.2 mm
$\eta_{vh}$	Vane head slope	30 deg

are placed. The pump cover must be modified as well to allow the rotor shaft passage and finally, two measure chamber are isolated by using O-ring gaskets. The pressure signals and the trigger are acquired and processed by a *LMS Scadas SC305 Front-end* controlled by software *LMS Test-Lab*. The pressure sensors being used are piezoelectric transducers *Kistler, model 6207*, the proximity sensor used as trigger is a *Balluff BES 516324S4C* finally, a charge amplifier *Kistler 5006* and an oscilloscope *Fluke 96 B Series II*, with a sampling frequency of 60 MHz have been used to perform an on-line control of the measurement procedure. The torque signal can be acquired as well by a torque transmitter *Stiger Mohilo 0160 DM*, with a full scale of 500 Nm.

With this set up the measure of the pressure inside a hole and a vane space can be obtained. The results are shown in Figures 2.20 and 2.21, in which the passage from the inlet to the outlet region can be immediately distinguished and the ripple phenomena for the high pressure region are underlined as well. The reference system used to plot the pressure evolution in Figure 2.20 is depicted in Figure 2.9: the angular coordinate reference starts from  $-y$  direction. For the sake of completeness also the test bench power train is depicted in Figure 2.18. All these aspects will be deeply analyzed in section 5.2.

Table 2.5: Pump *PHV 05* main clearances values.

$h_f$	Clearance on the vane flank	0.0173 mm
$h_d$	Clearance between rotor and distributor	0.023 mm
$h_g$	Clearance between a vane ad a rotor groove	0.0162 mm

Table 2.6: Lubricant *Shel Tellus ST 46* main features.

Lubricant viscosity ( $\mu$ )	11 ÷ 68 cSt
Max lubricant viscosity during start-up	400 cSt
Working condition temperature ( $temp$ )	+15 ÷ +60°C
Max lubricant contamination allowed	20/18/15

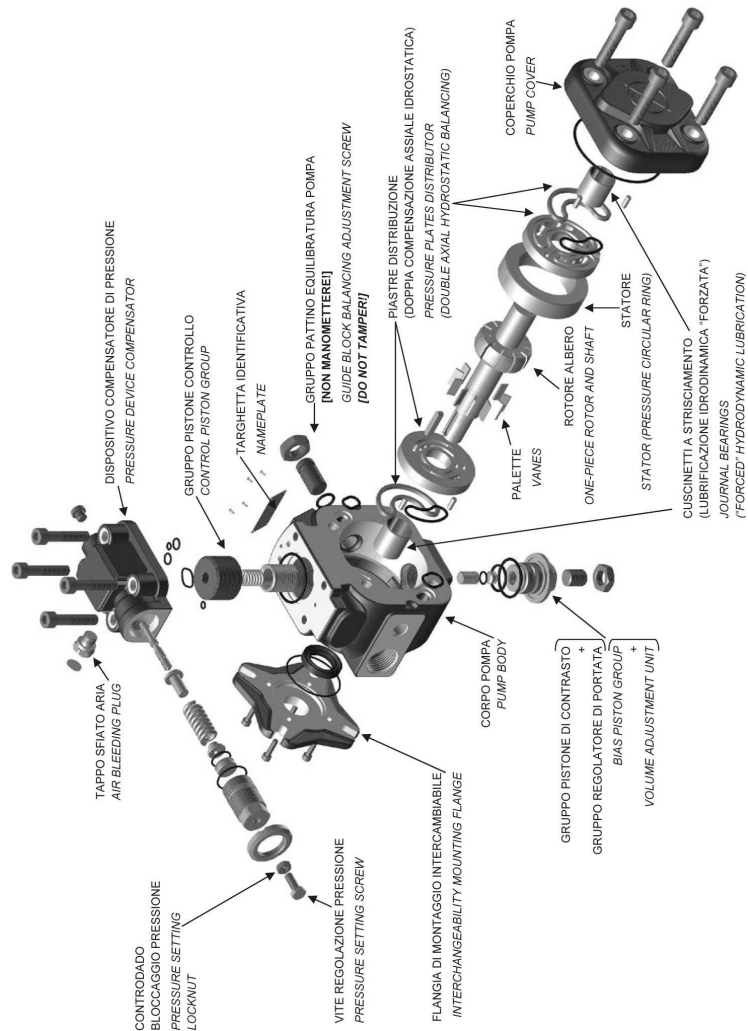


Figure 2.10: Pump *PHV 05* blow up.

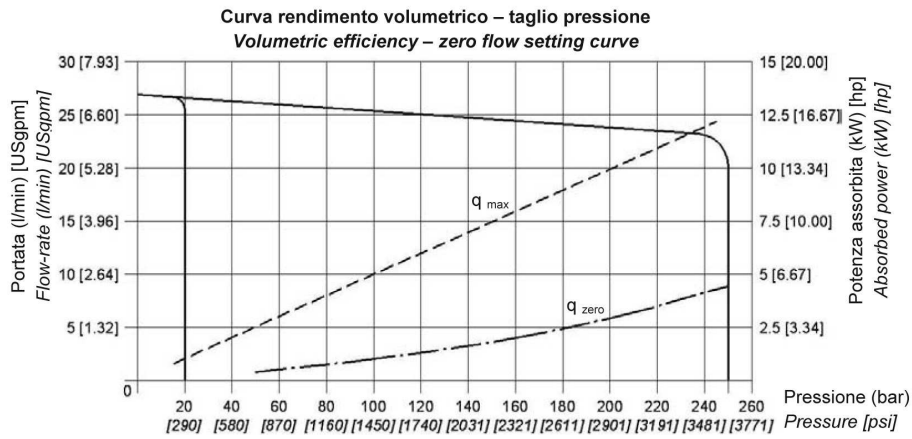


Figure 2.11: Pump *PHV 05* characteristic curve.

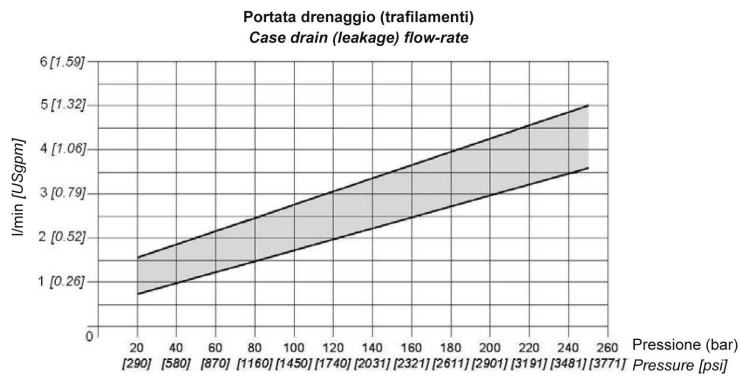


Figure 2.12: Pump *PHV 05* drainage flow rate range.

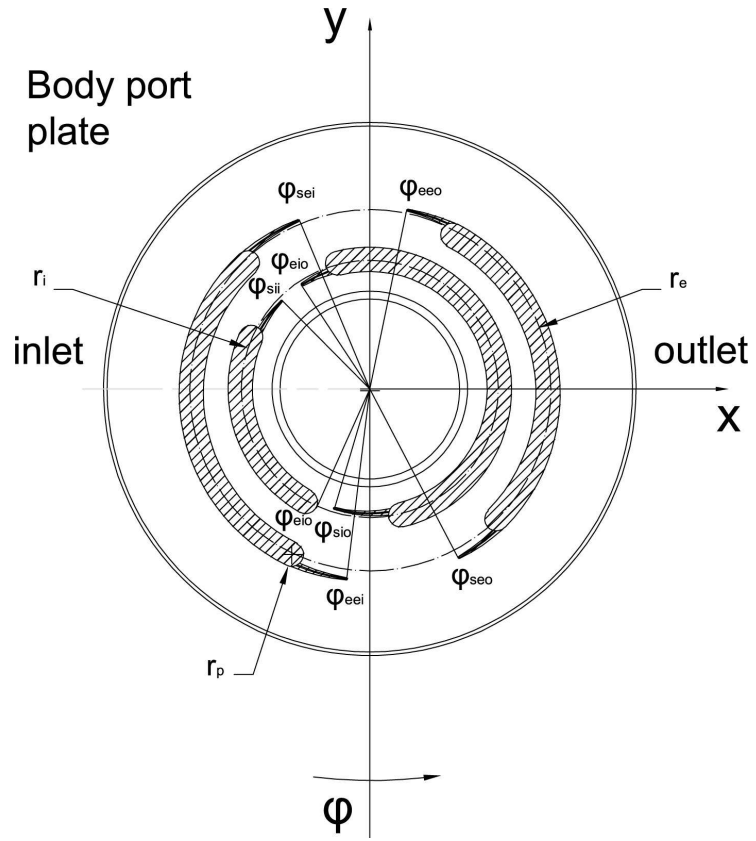


Figure 2.13: Port plate design.

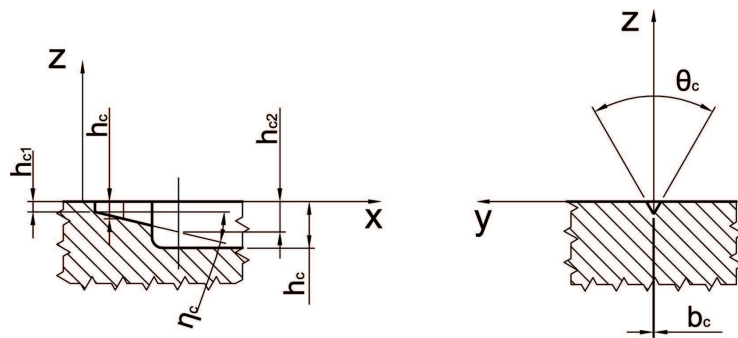


Figure 2.14: Port plate section.

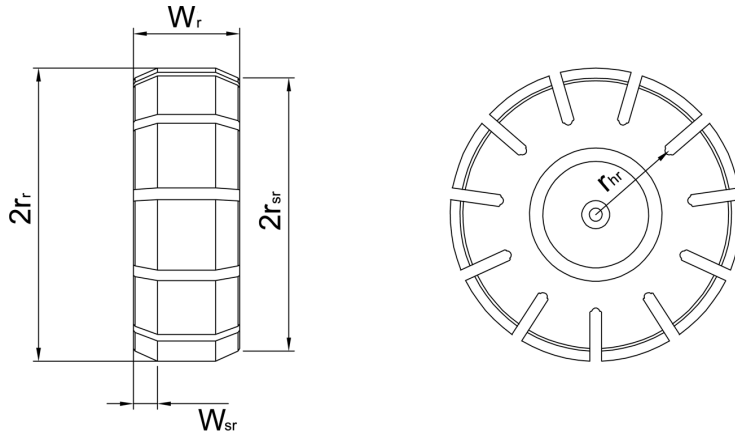


Figure 2.15: The rotor design.

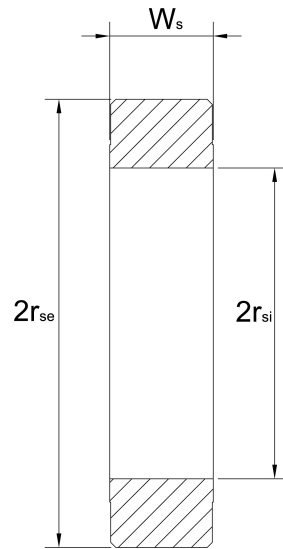


Figure 2.16: Pressure ring cross section.

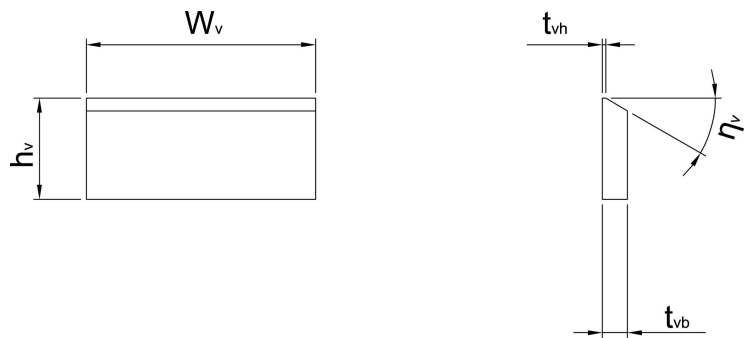


Figure 2.17: The vane design.

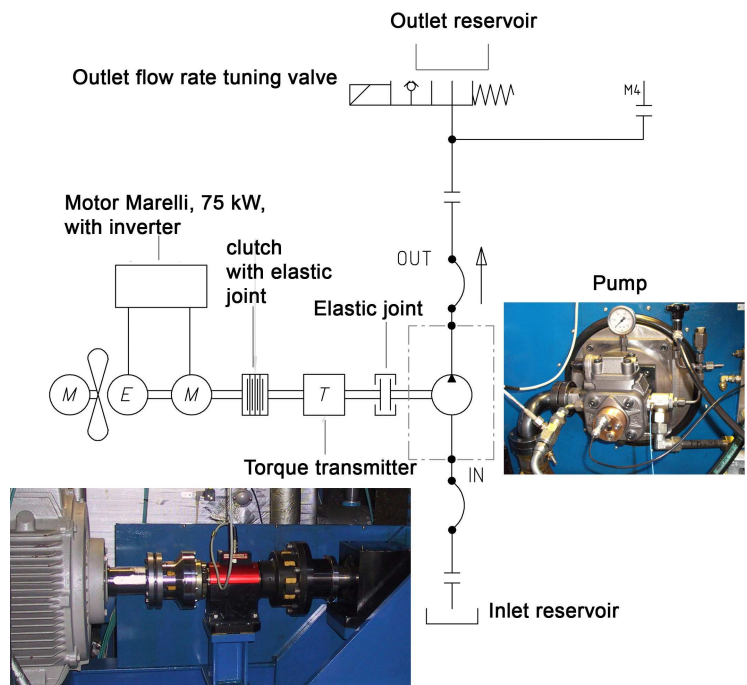


Figure 2.18: The test bench apparatus.

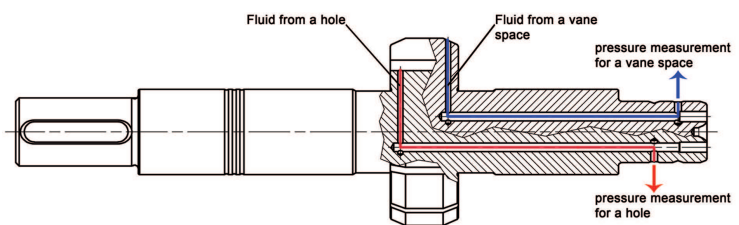


Figure 2.19: The modified rotor shaft used for the tests.



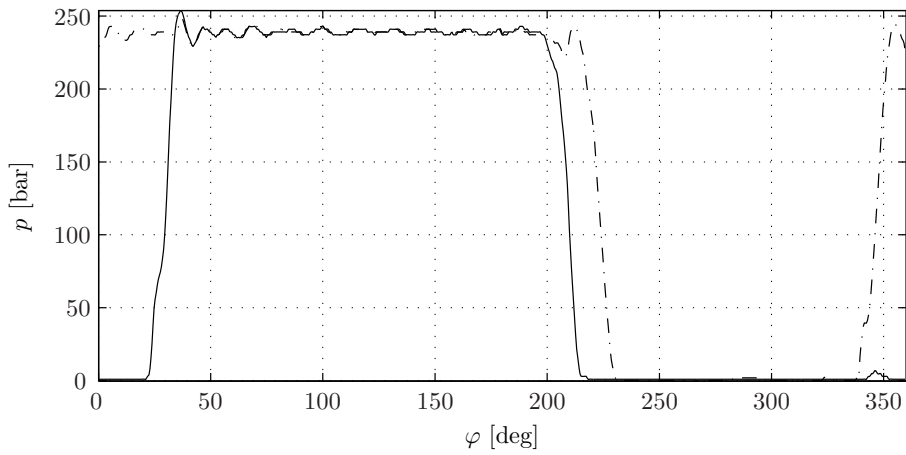


Figure 2.20: The pressure measured in a vane space (solid line) and in a hole (dash-dot line) for a complete shaft rotation in the full flow rate condition corresponding to the cutoff pressure.

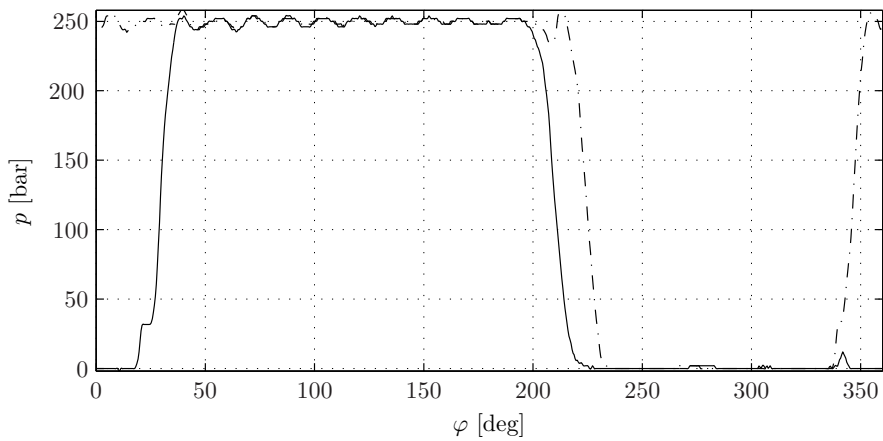


Figure 2.21: The pressure measured in a vane space (solid line) and in a hole (dash-dot line) for a complete shaft rotation in the zero flow rate condition, corresponding to the dead head pressure.



# Chapter 3

## Model description

The need to increase the knowledge on the dynamic behavior of a mechanical system leads to the formulation of reliable physical models, from which mathematical models can be obtained. After this step the model can be validated by comparing its results with empirical observations and finally the validated model can be used to perform simulations and make predictions.

### 3.1 General description of the model

The model takes into account only the transversal plane dynamics of the rotor shaft: it is a planar model with 3 degrees of freedom as presented in Figure 3.1. The inertia properties of the rotor shaft is considered to be lumped in the rotor portion carrying the vanes (indicated with "r" in Figure 3.1). Therefore the degrees of freedom are the displacement along the  $x$  and  $y$  direction and the angular displacement  $\varphi$  of the rotor portion.

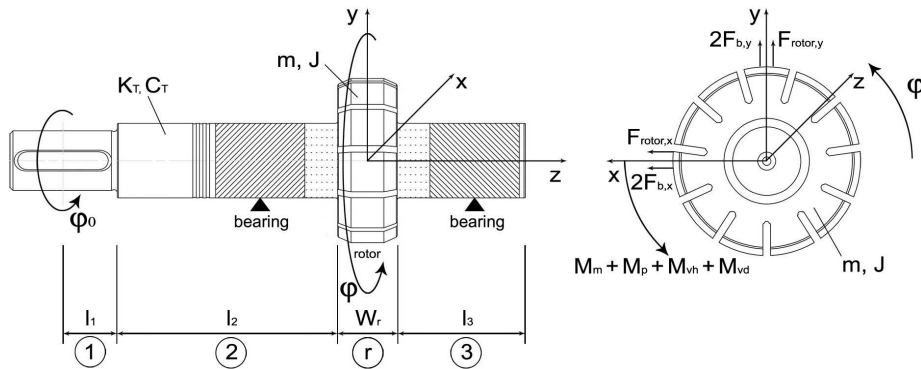


Figure 3.1: Model for the dynamic analysis of the rotor shaft.

The known model input is the coordinate  $\varphi_0$ , representing the angular displacement of the rotor shaft section in which the shaft is joined to the electrical motor drive through a key (see Figure 3.1, shaft portion 1). This section, as well as the motor, is assumed to rotate at constant speed  $\dot{\varphi}_0$ . Coordinate  $\varphi_0$  is

connected to coordinate  $\varphi$  by a torsional spring-damper element that represents the torsional stiffness and the damping of shaft portions 1 and 2 depicted in Figure 3.1. The shaft torsional stiffness is indicated as  $K_T$  and the proportional damping coefficient as  $C_T$ . The motor drive torque  $M_m$  is transmitted through this spring-damper element. Section 3.5.4 will illustrate the evaluation of  $K_T$  and  $C_T$  and the expression of  $M_m$  [2].

The inertia properties lumped in portion "r" are the whole rotor shaft mass  $m$  and the equivalent moment of inertia  $J$ , whose evaluation takes into account that the shaft portions between coordinates  $\varphi_0$  and  $\varphi$  (where the lumped inertia is located) is modeled as a torsional spring:

$$J = \frac{1}{3}(J_1 + J_2) + J_r + J_3 \quad (3.1)$$

where  $J_1$ ,  $J_2$ ,  $J_r$  and  $J_3$  are the moments of inertia of the shaft portions respectively indicated with "1", "2", "r" and "3" in Figure 3.1.

The forces and the torques applied to the rotor are pressure forces  $F_{rotor,x}$  and  $F_{rotor,y}$  (section 3.4.1), journal bearing reactions  $F_{b,x}$  and  $F_{b,y}$  (section 3.4.2), pressure torque  $M_p$  (section 3.5.1), torque due to friction between vane head and pressure ring  $M_{vh}$  (section 3.5.2), torque due to viscous actions  $M_{vd}$  (section 3.5.3) and the already mentioned motor drive torque  $M_m$  (section 3.5.4).

Thus, with respect to reference system depicted in Figure 3.1, the equations of motion for the model can be written as stated in equation system (3.2):

$$\begin{cases} 2F_{b,x} + F_{rotor,x} = m\ddot{x} \\ 2F_{b,y} + F_{rotor,y} = m\ddot{y} \\ M_m + M_p + M_{vh} + M_{vd} = J\ddot{\varphi} \end{cases} \quad (3.2)$$

In order to reduce the integration time, the average static position of journal axes into bearings are previously estimated and used as initial condition for displacements along  $x$  and  $y$  coordinates (see section 3.6). The variable pressure forces evolution has been estimated in the above mentioned static equilibrium position and finally it has been verified that this approach gives good results. The non linear differential equations of motion are numerically integrated in Simulink environment as described in section 4.1 [27].

## 3.2 Pressure distribution

Several researches have been done in *LP models* for vane pumps in order to obtain the pressure evolution around the shaft. The lumped parameter approach used in this work is based on [12, 13]. Even if these models were already based on an Euler's approach in which the pressure evolution during a rotation is studied by dividing the pump in several control volumes corresponding to vane spaces, they were not able to estimate the pressure ripple. Subsequent works have been done improving this first approach by increasing the number of control volumes to appreciate the pressure ripple in a vane space [9–11, 14]. In these last models also the distribution ducts are treated as control volumes. The present work is based on the latter approach but implements also the pressure calculation in the holes, i.e. the spaces included between the bottom of the vane, the rotor grooves and the port plates. The pressure in these domains is very important not only

to define the dynamical behavior of the rotor, but also to calculate the reaction forces between the vanes and the pressure ring. Obviously this new calculation involves more control volumes at the same time with respect to models devoted only to the vane space characterization.

It has to be observed that the fluid inertia effects inside control volumes have been neglected as well as all the excitations and flow rate fluctuations coming from the hydraulic circuit to which the pump is connected.

The first step in developing a proper algorithm for the pressure evolution calculation is the assumption of proper coordinate systems, as shown in Figure 2.9 and in Figure 3.2. Then, the pump system must be divided in several control volumes. The present model is based on 26 control volumes: control volumes from  $V_1$  to  $V_{11}$  correspond to the vane spaces; control volumes from  $V_{12}$  to  $V_{22}$  correspond to the holes control volumes, control volumes  $V_{23}$  and  $V_{25}$  are the control volumes of the outlet ducts and control volumes  $V_{24}$  and  $V_{26}$  are the inlet control volumes (see Figure 3.2 and 3.3). The number of control volumes involved in the pressure calculation remains constant during the whole integration period but the flow rate exchanged by control volumes can vary with respect to angular coordinate  $\varphi$ .

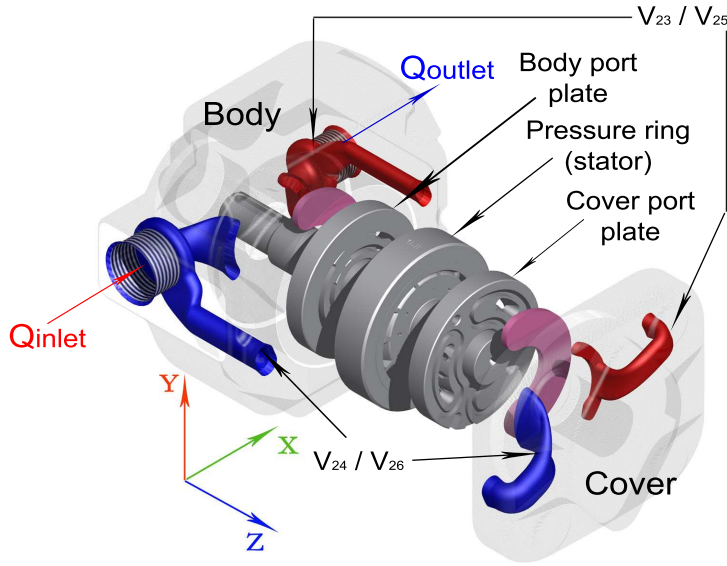
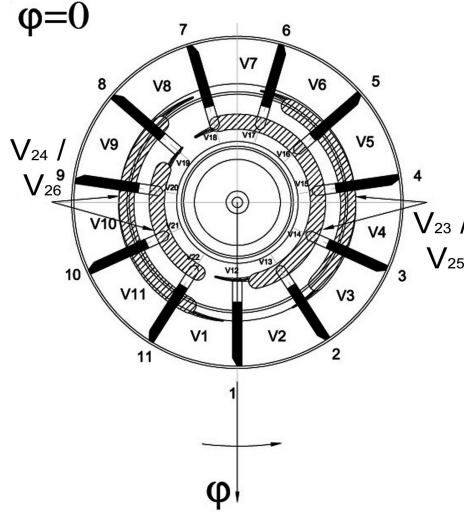


Figure 3.2: The main pump components, the inlet control volumes ( $V_{24}$ ,  $V_{26}$ ) and outlet control volume ( $V_{23}$ ,  $V_{25}$ ).

Applying to the open thermodynamic system consisting in control volume  $V_i$  the first thermodynamic principle, the continuity equation and the steady-state fluid equation, under the hypothesis of adiabatic and isentropic transformation, the following equation is thus obtained [28, 29]:

$$\frac{dp_i}{dt} = \frac{B_{oil}}{V_i} \left( \Delta Q_i - \frac{dV_i}{dt} \right) \quad (3.3)$$

Using this relation it is possible to determine the pressure variation of the fluid (characterized by Bulk modulus  $B_{oil}$ ) contained into the control volume  $V_i$ ,

Figure 3.3: The control volumes on a  $xy$  plane.

caused by mass gain of  $\Delta Q_i$  and by the volume variation  $\frac{dV_i}{dt}$ . Considering that  $dt = \frac{d\varphi}{\omega}$ , the continuity equation (3.3) can be expressed in terms of rotor shaft rotational angle  $\varphi$ :

$$\frac{dp_i}{d\varphi} = \frac{B_{oil}}{V_i \omega} \left( \Delta Q_i - \frac{dV_i}{d\varphi} \omega \right) \quad (3.4)$$

In order to solve equation (3.4), the calculus of the terms on the right side of equation, i.e. the volume and its variation and the incoming and exiting flow rates, has to be performed for each control volume. As mentioned before, the geometry is  $\varphi_{vp}$  periodic, where  $\varphi_{vp} = 360/N$  is the angular vane pitch. Since the all the phenomena involved in the pump rotation shows this periodicity, to improve the computational efficiency, the integration is done in the angular domain, from  $\varphi = 0$  to  $\varphi = \varphi_{vp}$ , then the pressure evolution around the shaft is obtained by adding the pressure field of each control volume consecutively. Finally, for determining the term  $\Delta Q_i$  of equation (3.4), it is necessary to understand how each volume communicates with each other or with the inlet or the outlet control volumes through the pump clearances or through inlet and outlet ducts.

### 3.2.1 Flow rates involved in continuity equations

Before writing the equations for each control volume, all the flow rates involved in defining term  $\Delta Q_i$  of equation (3.4) must be specified.

#### Laminar flow rates for vane spaces

The laminar flow rates (see Figure 3.4) take place from a vane space to the adjacent vane spaces, on the vane flank ( $Q_{vf}$ ), from a vane space to the holes ( $Q_{vh}$ ) and in the meatus between pressure ring and rotor (drainage flow rate

$Q_{vs}$ ). Since the vane is supposed to be always in contact with the inner race of the pressure ring, the flow rate in correspondence of the vane head is not taken into account. All these flow rates can be calculated as suggested by equation (3.5), in which  $b_i(\varphi)$ ,  $h_i(\varphi)$  and  $l_i(\varphi)$  are respectively the meatus width, thickness and length (see Figure 3.5). Hence, quantity  $\mu$  represents the lubricant dynamic viscosity,  $p_i$  is the pressure in the control volume and  $p_j$  is the pressure in the control volume interested by the exchange:

$$Q_{lam,i} = \frac{b_i(\varphi)h_i(\varphi)^3}{12\mu l_i(\varphi)}(p_j(\varphi) - p_i(\varphi)) \quad (3.5)$$

For the sake of brevity, with the term  $Q_{lam,i}$  it will be intended the sum of all the laminar contributions depicted before, referred to control volume  $i$ . It can be calculated after the geometry is fully described with respect to the angle  $\varphi$ .

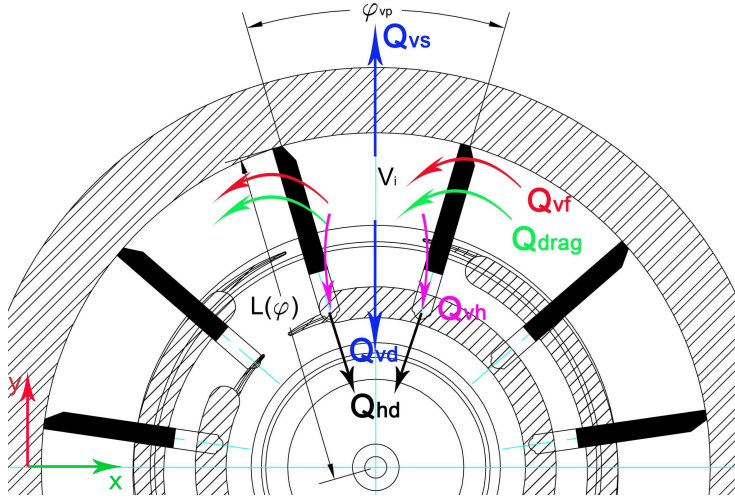


Figure 3.4: The laminar flow rates for a vane space and for a hole on a  $xy$  plane.

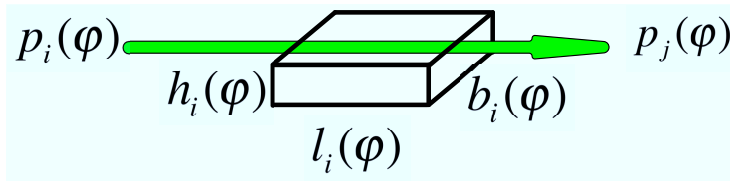


Figure 3.5: A general scheme of a laminar flow.

### Turbulent flow rates for vane spaces

The turbulent flow rates take place from the vane space control volume to the distribution ducts ( $Q_{vt}$  in Figure 3.6). It can be calculated using equation (3.6)

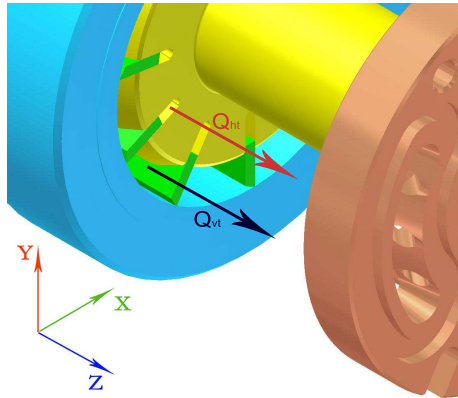


Figure 3.6: The turbulent flow rate for a vane space and for a hole.

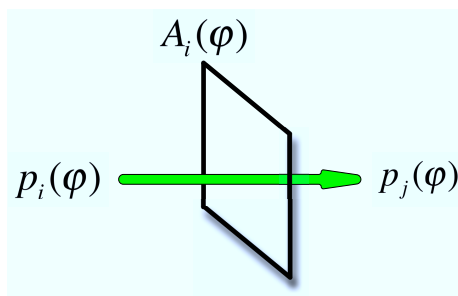


Figure 3.7: A general scheme of a turbulent flow.



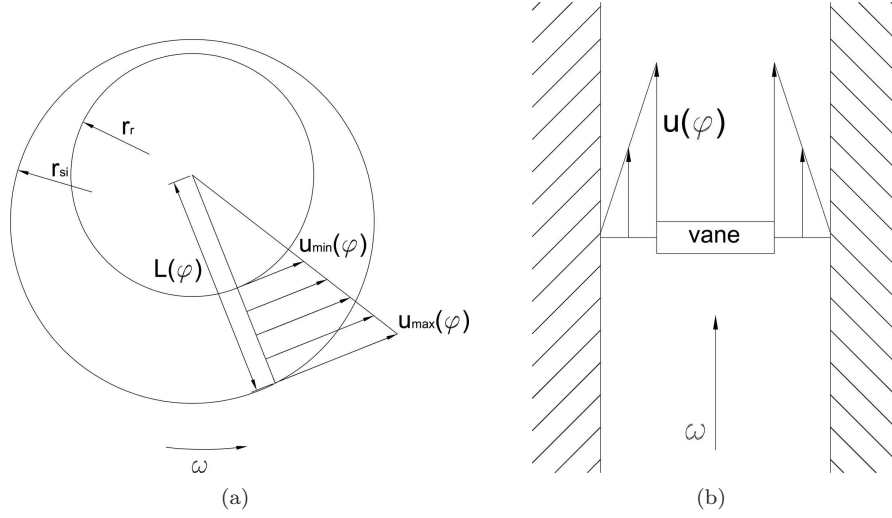


Figure 3.8: The tangential velocities involved in drag flow calculation.

in which  $k$  represents the flow coefficient,  $A_i(\varphi)$  is the exchange area between the control volume  $i$  and the control volume  $j$  (see section 3.3 for the calculation method),  $\rho$  is the lubricant density,  $p_i$  is the pressure in the control volume and  $p_j$  is the pressure in the control volume interested by the exchange.

$$Q_{turb,i} = kA_i(\varphi) \sqrt{\frac{2|p_j(\varphi) - p_i(\varphi)|}{\rho}} \text{sign}(p_j(\varphi) - p_i(\varphi)) \quad (3.6)$$

### Drag flow rate for vane spaces

Angular velocity  $\omega$  generates a tangential velocity  $u$  on the vane flanks. This velocity causes a flow rate independent to pressure field. First of all, to determine the drag flow rate  $Q_{drag}$ , the tangential velocities have to be analyzed on a  $xy$  plane and on a cylindrical section as depicted respectively in Figures 3.8(a) and 3.8(b). It can be noticed from Figure 3.8(a) that tangential velocities vary from  $u_{min}$  to  $u_{max}$ , the velocities in correspondence of the rotor and the pressure ring.

$$u_{min} = \omega r_r \quad (3.7)$$

$$u_{max} = \omega L(\varphi) \quad (3.8)$$

In equation (3.8), quantity  $L(\varphi)$  represents the distance between the rotor center and the pressure ring inner race taking into account shaft eccentricity and shaft displacement (the calculation will be explained in section 3.3).

The drag flow rate takes place in a meatus characterized by a thickness  $h_f$  on the vane flanks, side by side (see Figure 3.8(b)). On a cylindrical section the tangential velocity varies from 0 in correspondence to port plate distributors to  $u$ , in correspondence to vane flanks, where  $u$  can be calculated as follows:

$$u = \omega \frac{L(\varphi) + \omega r_r}{2} \quad (3.9)$$

Finally, the average velocity inside the meatus can be calculated as shown in equation (3.10).

$$u_m = \omega \frac{L(\varphi) + r_r}{4} \quad (3.10)$$

Considering a contribution of a single vane, the drag flow rate in a generic angular position  $\varphi$  can be calculated as follows:

$$Q_{drag} = 2u_m(L(\varphi) - r_r) \quad (3.11)$$

Therefore, the net drag flow rate for a vane space  $i$  at the angular coordinate  $\varphi$  can be calculated taking into account the drag flow on the first vane and of the second vane (at the coordinate  $\varphi - \varphi_{vp}$ ) as stated in equation (3.12) [30].

$$Q_{drag,i} = Q_{drag}(\varphi) - Q_{drag}(\varphi - \varphi_{vp}) = \omega \frac{(L(\varphi)^2 - L(\varphi - \varphi_{vp})^2)}{4} \quad (3.12)$$

### Laminar flow rates for holes control volumes

As shown in Figure 3.4, the holes control volumes are interested by three kind of laminar flow rates:

- $Q_{vh}$ : The laminar flows in the meatus between vanes and rotor grooves;
- $Q_{vd}$ : The laminar flow taking place between rotor and port plates;
- $Q_{hd}$ : The drainage flow taking place between rotor and port plates;

As all the other drainage flow rate,  $Q_{hd}$  connects a control volume with a region at atmospheric pressure.

### Turbulent flow rates for holes control volumes

Figure 3.6 depicts the only turbulent flow rate involving holes control volumes,  $Q_{ht}$ , taking place between holes and inner duct distributions.

### Inlet turbulent flow rates

The inlet control volume in communication with inlet pressure (usually atmospheric pressure) is  $V_{24}$ . In this case equation (3.6) can be rewritten as follows:

$$Q_{inlet} = k_{in} A_{inlet}(\varphi) \sqrt{\frac{2|p_{in} - p_{24}(\varphi)|}{\rho}} \text{sign}(p_{in} - p_{24}(\varphi)) \quad (3.13)$$

In equation (3.13) the quantity  $k_{in}$  is the flow coefficient (typically 0.65) and  $A_{inlet}$  represents the inlet duct interface area.

### Outlet turbulent flow rates

The outlet control volume in communication with outlet pressure is  $V_{23}$ . Usually it communicates with atmospheric pressure by means of the plant, whose presence is taken into account by the flow coefficient  $k_{outlet}$  (see equation (3.14)). Hence, the outlet flow rate  $Q_{outlet}$  (see Figure 3.2) has been expressed as follows:

$$Q_{outlet} = k_{outlet} A_{outlet} \sqrt{\frac{2|p_{out} - p_{23}(\varphi)|}{\rho}} \text{sign}(p_{atm} - p_i(\varphi)) \quad (3.14)$$

Where quantity  $p_{out}$  represents the atmospheric pressure, and the flow coefficient  $k_{outlet}$  takes into account the plant losses and resistance. By using equation (3.14) it is possible to estimate the flow coefficient  $k_{outlet}$ , in fact, assuming an outlet flow rate  $Q_{exp}$  experimentally assessed during the test campaign, a pressure in the outlet volume equal to  $p_{outlet}$ ,  $k_{outlet}$  can be determined as follows:

$$k_{outlet} = \frac{Q_{exp}}{A_{outlet}} \sqrt{\frac{\rho}{2|p_{atm} - p_{outlet}|}} \quad (3.15)$$

### Internal turbulent flow rates

As shown in Figure 3.9, the internal distribution ( $V_{25}$  and  $V_{26}$ ) and external distribution ( $V_{23}$  and  $V_{24}$ ) communicate by several ducts in which a turbulent flow rate it is supposed to take place because their diameter ( $d_d = 3.5$  mm) is almost equal to their length. These flow rates can be computed as stated in equation (3.6) and they will be denoted by the symbol  $Q_{td,i}$ .

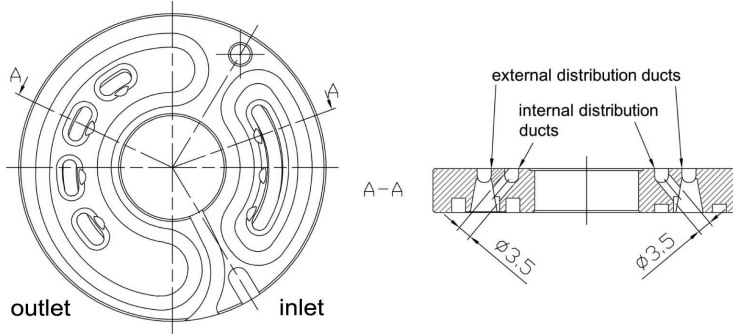


Figure 3.9: Ducts between external and internal distribution.

It is now clear that quantity  $\Delta Q_i$  depends on the pressure field so, for the control volume  $i$ , the equation (3.4) can be written as follows:

$$\frac{dp_i}{\varphi} = f_i(p(\varphi)) \quad (3.16)$$

In equation (3.16), symbol  $p(\varphi)$  represents the whole pressure field. To determine this quantity, the equation system (3.17) constituted by 26 non linear differential equation must be solved.

$$\left\{ \begin{array}{l} \frac{dp_1(\varphi)}{d\varphi} = f_1(p_1, \dots, p_{26}) \\ \vdots \\ \frac{dp_{26}(\varphi)}{d\varphi} = f_{26}(p_1, \dots, p_{26}) \end{array} \right. \quad (3.17)$$

### 3.2.2 Flow rate equations

In this section the flow rate continuity equations will be derived for each control volume to fully define equation system (3.17). The equations are written taking into account all the possible configurations for the control volumes communications over a vane pitch  $\varphi_{vp}$ .

#### Flow rate balance equation for a generic vane space

With reference to equation (3.4), the term  $\Delta Q_i$  must be expanded to understand the meaning of each flow rate contribution. Figure 3.4 and 3.6 depicts the various contributions whose algebraic sum constitutes the term  $\Delta Q_i$ . Finally, equation (3.4) can be rewritten as follows:

$$\frac{dp_i}{d\varphi} = \frac{B_{oil}}{V_i \omega} \left( Q_{drag,i} + Q_{vs,i} + Q_{vd,i} + Q_{vh,i} + Q_{vf,i} + Q_{vt,i} - \frac{dV_i}{d\varphi} \omega \right) \quad (3.18)$$

All the terms of equation (3.18) have been described in previous section. More in detail the subscript  $i$  denotes the control volume ( $i = 1 \dots N$ , where  $N$  is the vane number), the terms  $Q_{vs,i}$ ,  $Q_{vd,i}$ ,  $Q_{vh,i}$ ,  $Q_{vf,i}$  refers to laminar flow rates and can be calculated as stated in equations (3.19 - 3.22).

$$Q_{vs,i} = 2 \frac{b_{s,i}(\varphi) h_{s,i}(\varphi)^3}{12 \mu l_{s,i}(\varphi)} (p_{drain}(\varphi) - p_i(\varphi)) \quad (3.19)$$

In equation (3.20)  $p_{drain}$  represents the drainage pressure (usually atmospheric pressure) and the subscripts  $s, i$  denote the clearance between pressure ring and port plates with reference to control volume  $i$ .

$$Q_{vd,i}(\varphi) = 2 \frac{b_{r,i}(\varphi) h_{r,i}(\varphi)^3}{12 \mu l_{r,i}(\varphi)} (p_{drain}(\varphi) - p_i(\varphi)) \quad (3.20)$$

In equation (3.20) the subscripts  $r, i$  denote the clearance between rotor and port plates with reference to control volume  $i$ .

$$Q_{vf,i} = 2 \frac{b_{f,i+1}(\varphi) h_{f,i+1}(\varphi)^3}{12 \mu l_{f,i+1}(\varphi)} (p_{i+1}(\varphi) - p_i(\varphi)) + 2 \frac{b_{f,i-1}(\varphi) h_{f,i-1}(\varphi)^3}{12 \mu l_{f,i-1}(\varphi)} (p_{i-1}(\varphi) - p_i(\varphi)) \quad (3.21)$$

In equation (3.21) the subscripts  $f$  denote the clearance between vane flank and port plates, the subscript  $i$  indicates the control volume for which the flow rate balance equation is written, while the subscripts  $i+1$  and  $i-1$  refer respectively

to control volume immediately after and before control volume  $i$  with respect to the verse of angular velocity  $\omega$ .

$$Q_{vh,i} = \frac{b_{h,i}(\varphi)h_{h,i}(\varphi)^3}{12\mu l_{h,i}(\varphi)}(p_{i+N}(\varphi) - p_i(\varphi)) + \frac{b_{h,i-1}(\varphi)h_{h,i-1}(\varphi)^3}{12\mu l_{h,i-1}(\varphi)}(p_{i+N-1}(\varphi) - p_i(\varphi)) \quad (3.22)$$

In equation (3.22) the subscripts  $h$  denote the clearance between vane and rotor grooves, the subscript  $i$  indicates the control volume for which the flow rate balance equation is written, the subscript  $i + N$  and  $i + N - 1$  individuate the hole control volume under the vane  $i$  and  $i - 1$  respectively ( $N$  represents the number of vanes, see Figure 3.3 to understand how the control volumes have been numbered).

The term  $Q_{vt,i}$  represents the turbulent flow rate exchanged by control volume  $i$  with the outlet and inlet distribution ducts. Inlet distribution duct corresponds to control volume  $V_{24}$ , while outlet distribution duct corresponds to control volume  $V_{23}$  (see Figure 3.2). During the integration period (from  $\varphi = 0$  to  $\varphi = \varphi_{vp}$ ) a control volume can communicate with both inlet and outlet or can remain isolated for a certain angular interval. All these facts are automatically taken into account by the factor  $A_{23,i}$  and  $A_{24,i}$  of equation (3.26). In fact these quantities represent respectively the passage area between the control volume  $i$  and the outlet or inlet control volumes and they become zero when there is no communications between control volumes involved in the flow exchange.

$$Q_{vt,i} = kA_{23,i}(\varphi)\sqrt{\frac{2|p_{23}(\varphi) - p_i(\varphi)|}{\rho}}\text{sign}(p_{23}(\varphi) - p_i(\varphi)) + kA_{24,i}(\varphi)\sqrt{\frac{2|p_{24}(\varphi) - p_i(\varphi)|}{\rho}}\text{sign}(p_{24}(\varphi) - p_i(\varphi)) \quad (3.23)$$

### Flow rate balance equation for a generic hole control volume

With reference to equation (3.4), the term  $\Delta Q_i$  must be expanded to understand the meaning of each flow rate contribution. Figure 3.4 and 3.6 depicts the various contributions whose algebraic sum constitutes the term  $\Delta Q_i$ . Equation (3.4) can be rewritten as follows:

$$\frac{dp_i}{d\varphi} = \frac{B_{oil}}{V_i\omega} \left( Q_{hd,i} + Q_{vh,i} + Q_{ht,i} - \frac{dV_i}{d\varphi}\omega \right) \quad (3.24)$$

All the terms of equation (3.24) have been described in previous sections. More in detail the subscript  $i$  denotes the control volume ( $i = N + 1 \dots 2N$ , where  $N$  is the vane number), the term  $Q_{hd,i}$  refers to laminar flow rates and can be calculated as stated in equation (3.25).

$$Q_{hd,i}(\varphi) = 2\frac{b_{hr,i}(\varphi)h_{hr,i}(\varphi)^3}{12\mu l_{hr,i}(\varphi)}(p_{drain}(\varphi) - p_i(\varphi)) \quad (3.25)$$

Where the subscripts  $hr, i$  denote the clearance between rotor and port plates with reference to control volume  $i$ , starting from a hole. The term  $Q_{vh,i}$  calculation has been described in equation (3.22). For a hole control volume this flow rate can be calculated by using the same method.

The term  $Q_{ht,i}$  represents the turbulent flow rate exchanged by control volume  $i$  with the outlet and inlet internal distribution ducts. Inlet distribution duct corresponds to control volume 26, while outlet distribution duct corresponds to control volume 25 (see Figure 3.2). During the integration period (from  $\varphi = 0$  to  $\varphi = \varphi_{vp}$ ) a hole control volume can communicate with both inlet and outlet or can remain isolated for a certain angular interval. All these facts are automatically taken into account by the factor  $A_{25,i}$  and  $A_{26,i}$  of equation (3.26). In fact these quantities represent respectively the passage area between the control volume  $i$  and the outlet or inlet control volumes and they becomes zero when there is no communications between control volumes involved in the flow exchange.

$$Q_{ht,i} = kA_{25,i}(\varphi) \sqrt{\frac{2|p_{25}(\varphi) - p_i(\varphi)|}{\rho}} \text{sign}(p_{25}(\varphi) - p_i(\varphi)) + kA_{26,i}(\varphi) \sqrt{\frac{2|p_{26}(\varphi) - p_i(\varphi)|}{\rho}} \text{sign}(p_{26}(\varphi) - p_i(\varphi)) \quad (3.26)$$

#### Flow rate balance equation for external outlet control volume

To understand which volumes communicate with the external inlet distribution duct (control volume 23) all the possible configurations during integration period must be investigated. After all the volumes in communication with control volume  $V_{23}$  have been considered, the following equation can be obtained:

$$\frac{dp_{23}}{d\varphi} = \frac{B_{oil}}{V_i\omega} \left( Q_{td,23} + Q_{outlet} - \sum_{i=1}^N Q_{vt,i} \right) \quad (3.27)$$

In equation (3.27), the term  $Q_{td,23}$  represents the turbulent flow rate taking place inside four ducts between external and internal distribution (see Figure 3.9). It can be calculated as follows:

$$Q_{td,23} = 4kA_{duct} \sqrt{\frac{2|p_{25} - p_{23}(\varphi)|}{\rho}} \text{sign}(p_{25}(\varphi) - p_{23}(\varphi)) \quad (3.28)$$

In equation(3.28),  $A_{duct}$  represents the area of ducts between the external distribution volume (control volume  $V_{23}$ ) and the internal distribution volume (control volume 25).

#### Flow rate balance equation for external inlet control volume

The observations useful to understand the flow rate balance equation for outlet control volume are still valid, only subscript indexes must be changed to take into account the changing in communications between control volumes. The flow rate balance equation for control volume  $V_{24}$  is reported below:

$$\frac{dp_{24}}{d\varphi} = \frac{B_{oil}}{V_i\omega} \left( Q_{td,24} + Q_{inlet} - \sum_{i=1}^N Q_{vt,i} \right) \quad (3.29)$$

Where the term  $Q_{td,24}$  can be calculated as suggested by equation (3.30).

$$Q_{td,24} = 4kA_{duct} \sqrt{\frac{2|p_{26} - p_{24}(\varphi)|}{\rho}} \text{sign}(p_{26}(\varphi) - p_{24}(\varphi)) \quad (3.30)$$

### Flow rate balance equation for internal outlet control volume

The internal outlet control volume corresponds to control volume  $V_{25}$ . Its flow rate balance equation can be summarized as follows:

$$\frac{dp_{25}}{d\varphi} = \frac{B_{oil}}{V_i\omega} \left( -Q_{td,23} - \sum_{i=1}^N Q_{ht,i} \right) \quad (3.31)$$

### Flow rate balance equation for internal outlet control volume

The internal outlet control volume corresponds to control volume 26. Its flow rate balance equation can be summarized as follows:

$$\frac{dp_{26}}{d\varphi} = \frac{B_{oil}}{V_i\omega} \left( -Q_{td,24} - \sum_{i=1}^N Q_{ht,i} \right) \quad (3.32)$$

## 3.2.3 System integration

Each row of equation system (3.17) is now fully described. It is a first order system of non-linear differential equations with non-constant coefficients that has to be solved using the iterative procedure depicted in Figure 3.30. The first trial pressure  $p^0$  has to be provided as input data and the initial condition can be written in the following form:

$$\left\{ \begin{array}{l} p_1(\varphi = 0) = p_{in} \\ \vdots \\ p_{26}(\varphi = 0) = p_{in} \end{array} \right. \quad (3.33)$$

Basing on  $p^0$ , the pressure force around the rotor ( $F^0$ ) can be calculated to define the shaft displacement and the first trial journal bearing static equilibrium position ( $SEP^0$ ) whose theoretic description is reported in section 3.6. Shaft displacement and  $SEP^0$  can be used to define the eccentricity between rotor and pressure ring in working condition as follows:

$$\mathbf{e}_{tot} = \mathbf{e}_f + \mathbf{e}_i + \mathbf{e}_{SEP} \quad (3.34)$$

Quantity  $\mathbf{e}_{tot}$  in Figure 3.12 represents the total eccentricity between the rotor center and the pressure ring,  $\mathbf{e}_f$  is the contribution due to shaft displacement under the pressure force load, while  $\mathbf{e}_i$  is the eccentricity imposed to the pressure ring and the eccentricity due to journal bearing clearance  $\mathbf{e}_{sep}$  will be further explained in next sections.

The volume evolution  $V(\varphi)$  and the rate of volume variation  $\frac{dv}{d\varphi}$  can be calculated once  $\mathbf{e}_{tot}$  and the geometry are determined. At this point, the full system

can be written by using auxiliary quantities whose calculation will be described in section 3.3. After the integration, the pressure field for each control volume is obtained from  $\varphi = 0$  to  $\varphi = \varphi_{vp}$ . Then, the pressure evolution around the shaft is obtained by adding the pressure fields of the first  $N$  control volumes consecutively. The same procedure can be adopted to obtain the pressure evolution for a generic hole control volume by using the pressure fields of calculated for control volumes from  $V_{N+1}$  to  $V_{2N}$ . In this way the pressure evolution can be obtained by integrating on a vane pitch only, and not on a whole shaft evolution. Finally a new pressure force  $F^1$  and a new static equilibrium position  $SEP^1$  can be calculated. The iteration will proceed till the results of two successive iterations will match under a small tolerance in term of force  $F$  and  $SEP$ .

### 3.3 Auxiliary quantities for pressure distribution calculation

In section 3.2 several quantities have been defined with the aim at solving the pressure evolution problem. Some of these can be directly calculated by knowing geometrical data, i.e. the laminar flow rates taking place in the clearances meatus. To define other quantities the implementation of proper subroutines is required. This is the case of shaft displacement  $f$ , of  $L(\varphi)$  in equation (3.11) of the volume  $V_i(\varphi)$  in equation (3.4) of the rate of volume variation  $\frac{dV_i}{d\varphi}$ , of the passage areas  $A_i(\varphi)$  used to compute turbulent flow rates (see equation (3.6)). Finally, in Appendix A, the distribution ducts corresponding to control volumes  $V_{23}$ ,  $V_{24}$ ,  $V_{25}$ ,  $V_{26}$ , are characterized in terms of shape and volumes.

#### 3.3.1 Shaft displacement

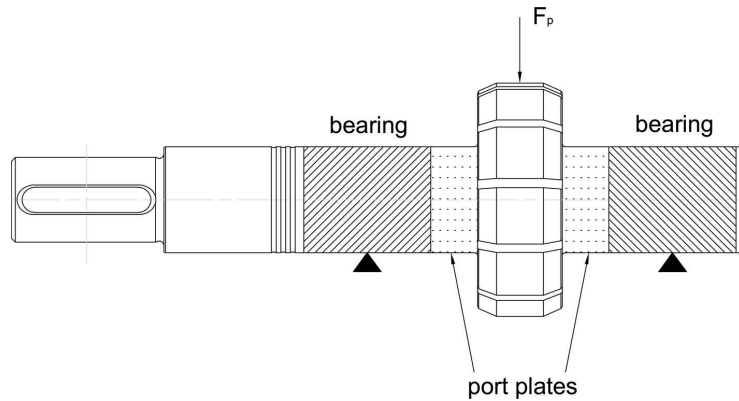


Figure 3.10: Geometry considered for the shaft displacement calculation.

The shaft displacement  $f$  is important in defining a component of eccentricity between rotor and pressure ring called  $e_f$  (see equation (3.34)). Considering that the rotor diameter is bigger than shaft diameter, the analysis can be focused only on the shaft pieces from the journal bearing middle axis to rotor flanks. The shaft load condition can be reduced to the scheme depicted in Figure 3.11.



This approach considers the rotor infinitely rigid with respect to shaft diameter. Several approaches have been used to determine in the most accurate way the rotor shaft stiffness. First of all the shaft bending stiffness has been calculated using equation (3.35), then the shear stiffness has been determined using equation (3.36). Hence an equivalent stiffness is calculated considering as series spring the shear and the bending stiffness. Finally the stiffness has been calculated also by means of a finite elements analysis ( $K_{FEM} = 1.80 \cdot 10^9$  N/m).

$$K_F = \frac{6EI}{l^3} = 1,37 \cdot 10^9 \text{ N/m} \quad (3.35)$$

$$K_T = \frac{2\pi Gr_s^2}{l\beta} = 2.74 \cdot 10^9 \text{ N/m} \quad (3.36)$$

$$l = h_p + \frac{W_b}{2} \quad (3.37)$$

$$I = \frac{\pi(2r_s)^4}{64} \quad (3.38)$$

$$K = \frac{1}{\frac{1}{K_F} + \frac{1}{K_T}} = 9.16 \cdot 10^8 \text{ N/m} \quad (3.39)$$

In equation (3.35),  $E$  is the Joung modulus,  $l$  is the considered shaft length, and  $I$  is the polar moment of inertia relative to the shaft (see equations (3.37), in which  $W_b$  represents the journal bearing axial width, and (3.38)). In equation (3.36),  $G$  is the shear modulus,  $\beta$  is the shear factor, equal to  $\frac{10}{9}$ . After having compared the results in terms of pressure evolution obtained by using approaches listed before, the analytical formulation resumed in equations (3.35), (3.36), (3.39) has been used inside the model for the shaft displacement calculation as proposed by equation (3.40),

$$f = \frac{F_{rotor}}{K} \quad (3.40)$$

in which  $F_{rotor}$  is the pressure force due to the pressure distribution around the rotor.

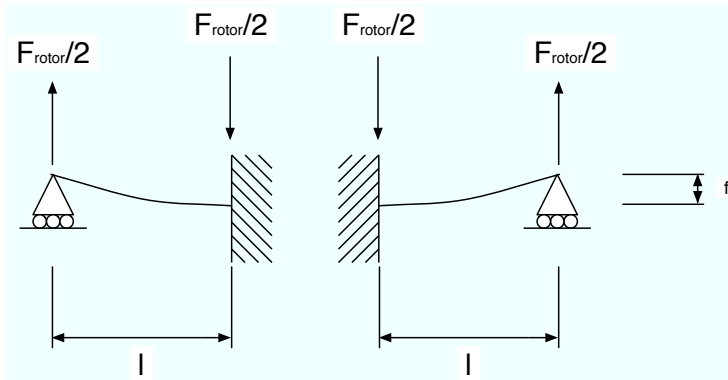


Figure 3.11: Geometry scheme for the shaft displacement calculation.

### 3.3.2 Distance between rotor center and pressure ring

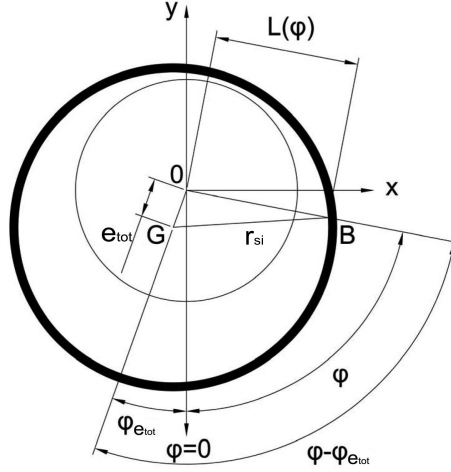


Figure 3.12: Geometrical scheme used to compute distance between rotor center and pressure ring inner race.

The distance between rotor center and pressure ring inner race ( $L(\varphi)$ ) is very important in determining the volume of a vane space and other important quantities involved in the integration of equation system (3.17). The quantity  $\mathbf{e}_{tot}$  in Figure 3.12 represents the total eccentricity between the rotor center and the pressure ring. It can be computed as suggested by equation (3.34). The component  $e_i$  can be imposed by a system of bias and control piston along the  $-x$  and  $-y$  directions. After having determined the value of  $\mathbf{e}_{tot}$ ,  $L(\varphi)$  can be calculated applying the law of cosine to  $OGB$  triangle:

$$r_{si}^2 = e_{tot}^2 + L(\varphi)^2 - 2L(\varphi)e_{tot}\cos(\varphi - \varphi_{e_{tot}}) \quad (3.41)$$

Solving the quadratic expression with respect to  $L(\varphi)$  it is possible to obtain the relation between the angular coordinate and the distance between rotor center and pressure ring inner race as follows:

$$L(\varphi) = e_{tot}\cos(\varphi - \varphi_{e_{tot}}) + \sqrt{r_{si}^2 - e_{tot}^2\sin^2(\varphi - \varphi_{e_{tot}})} \quad (3.42)$$

### 3.3.3 Volume evolution for a vane space

The volume included between two consecutive vanes can be calculated by adding three different contributions,  $V_m$ ,  $V_h$  and  $V_s$ , whose physical meaning is depicted in Figure 3.13.  $V_m$  represents the main volume included between two vane,  $V_h$  is the volume included between the upper part of the vane and the pressure ring and finally  $V_s$  is the volume delimited by lateral distributors, rotor sides and the main volume  $V_m$ . While  $V_m$  changes its value during a shaft revolution, the value of  $V_h$  and  $V_s$  remains constant.

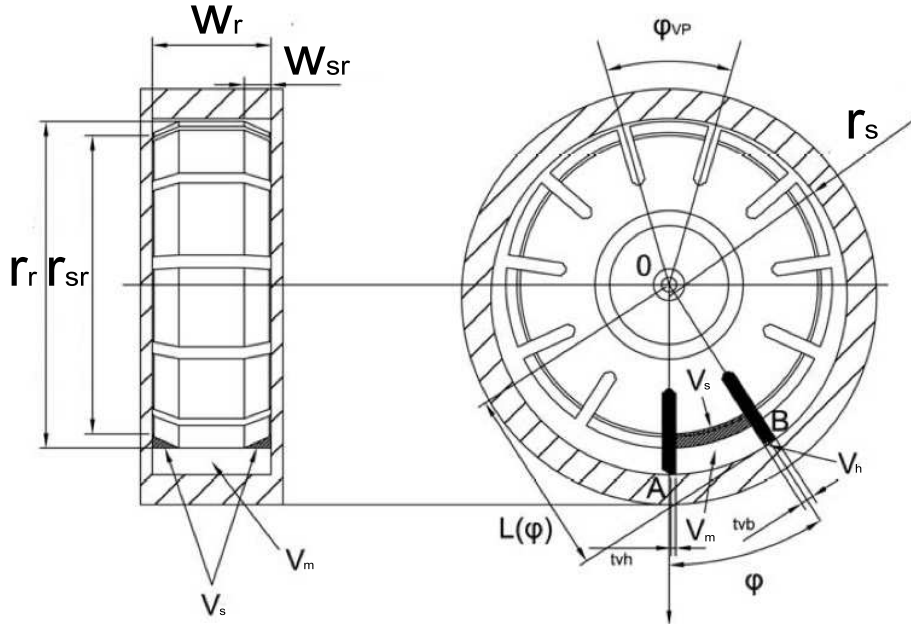


Figure 3.13: The volume of a vane space.

### Determination of $V_m$

It is possible to obtain  $V_m$  by considering several contributions as stated in equation (3.43).

$$V_m(\varphi) = V_{m,1} - V_{m,2} - V_{m,3} \quad (3.43)$$

The term  $V_{m,1}$  represents the volume contribution due to projection of the surface delimited by segments  $OA$  and  $OB$  and by the arc  $AB$  along the rotor shaft axial direction, the term  $V_{m,2}$  represents the contribution due to the volume occupied by the vane and the term  $V_{m,3}$  represents the rotor volume.

$$V_{m,1}(\varphi) = W_r \int_{\varphi - \varphi_{vp}}^{\varphi} \frac{L(\varphi)^2}{2} d\varphi \quad (3.44)$$

$$V_{m,2}(\varphi) = W_r \frac{t_{vb}}{2} (L(\varphi)^2 - L(\varphi - \varphi_{vp})^2 - 2r_r) \quad (3.45)$$

$$V_{m,3}(\varphi) = W_r \frac{r_r^2 \varphi_{vp}}{2} \quad (3.46)$$

Using equations (3.44), (3.45), (3.46), equation (3.43) can be rewritten as follows:

$$V_m(\varphi) = W_r \left( \int_{\varphi - \varphi_{vp}}^{\varphi} \frac{L(\varphi)^2}{2} d\varphi - \frac{t_{vb}}{2} (L(\varphi)^2 + L(\varphi - \varphi_{vp})^2 - 2r_r) - \frac{r_r^2 \varphi_{vp}}{2} \right) \quad (3.47)$$

**Determination of  $V_h$** 

The volume  $V_h$  remains constant during the shaft revolution. It can be calculated as a prism with a triangular base and high  $W_r$ . With reference to Figure 3.13, the expression for  $V_h$  is the following:

$$V_h = \frac{W_r(t_{vb} - t_{vh})^2 \tan(\eta_{vh})}{2} \quad (3.48)$$

**Determination of  $V_s$** 

The volume  $V_s$  (see Figure 3.13) remains constant during the shaft revolution, it is symmetrically distributed on the two rotor sides and it can be calculated as follows:

$$V_s = W_{sr}(r_r - r_{sr})(r_r \varphi_{vp} - t_{vb}) \quad (3.49)$$

Where  $W_{sr}$  represents the rotor sides width (see Figure 2.15). To conclude, it is possible to express  $V_v$  as stated in equation (3.50).

$$V_v(\varphi) = W_r \left( \int_{\varphi - \varphi_{vp}}^{\varphi} \frac{L(\varphi)^2}{2} d\varphi - \frac{t_{vb}}{2} (L(\varphi)^2 + L(\varphi - \varphi_{vp})^2 - 2r_r) - \frac{r_r^2 \varphi_{vp}}{2} - \frac{W_r(t_{vb} - t_{vh})^2 \tan(\eta_{vh})}{2} - W_{sr}(r_r - r_{sr})(r_r \varphi_{vp} - t_{vb}) \right) \quad (3.50)$$

**3.3.4 Volume evolution for a hole control volume**

The volume trapped under a vane, in a rotor groove can be calculated by analyzing the hole geometry on a  $xy$  plane (see Figure 3.14). The distance between the vane bottom and the rotor groove ( $h_{rg}$ ) can be calculated as follows:

$$h_{rg}(\varphi) = L(\varphi) - h_v - r_{rg} \quad (3.51)$$

where  $r_{rg}$  represents the fillet radius at the end of each rotor groove (see Figure 3.14). The volume of a hole can now be easily determined as proposed in equation (3.52).

$$V_h(\varphi) = W_r \left( \frac{\pi r_{rg}^2}{2} + h_{rg}(\varphi) t_{vb} \right) \quad (3.52)$$

**3.3.5 Rate of volume variation**

The rate of volume variation  $\frac{dV_i}{d\varphi}$  can be calculated by discretizing the volume evolution with respect to angular coordinate by step  $\Delta\varphi$ . To do this, equation (3.53) can be applied.

$$\frac{dV_i(\varphi)}{d\varphi} = \frac{V(\varphi + \Delta\varphi) - V(\varphi)}{\Delta\varphi} \quad (3.53)$$

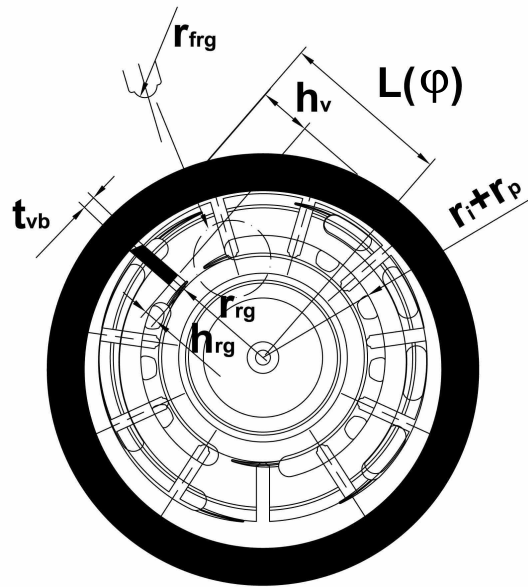


Figure 3.14: The hole geometry on a  $xy$  plane.

### 3.3.6 Passage area evolution for a vane space

The term  $A_i(\varphi)$  involved in equation (3.6) represents the passage area between a vane space and distribution duct. This calculation must be done by a subroutine suitably studied to compute the passage area of a vane space in function of port plate design features (see Figure 2.13). To do this the linearized geometry depicted in Figure 3.15 can be studied.

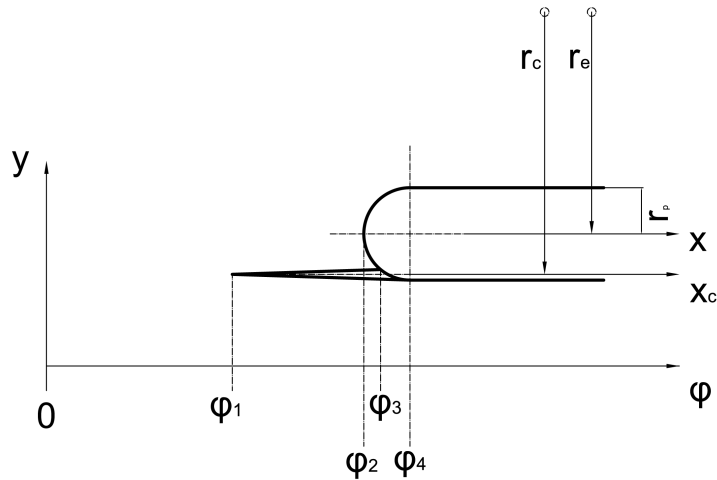


Figure 3.15: Angular region for passage area calculation.

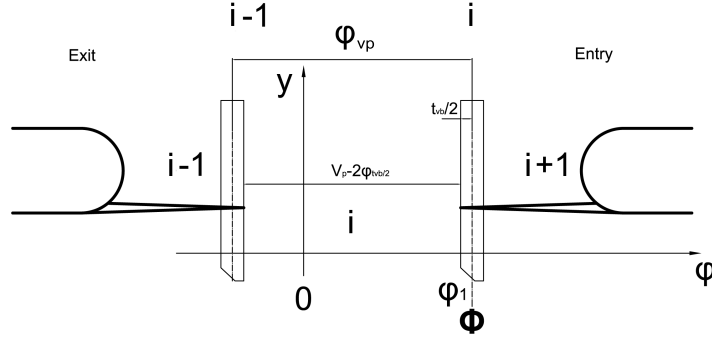


Figure 3.16: The angular coordinate for passage area calculation.

During the area calculation procedure, the zero coordinate is in correspondence of the  $-y$  direction and  $\varphi_1$  corresponds to  $\varphi_{seo}$  in Figure 2.13, while  $\varphi_4$  corresponds to the beginning of the inlet/outlet constant section. With reference to Figure 3.15, from  $\varphi_1$  to  $\varphi_2$  the passage area has been considered on a  $yz$  plane, in correspondence of a carving transversal section while, once  $\varphi_2$  is passed by the vane, the passage area is considered on a  $xy$  plane. In Figure 3.16, the convention used to compute the passage area is explained:  $\phi$  represents the current angular coordinate on the  $\varphi$  axis, the control volume we want to determine the passage area is  $V_i$  and it is included between the vane  $i$  and the vane  $i - 1$ . In agreement with this convention, the passage area for the control volume  $V_i$  starts to increase when all the vane  $i$  passes the carving corner ( $\phi > \varphi_1 + \varphi_{tvb}/2$ ). On the other side, the closure is anticipated of the same angular quantity  $\varphi_{tvb}/2$ . The vane angular extension  $\varphi_{tvb}$  can be calculated by using equation (3.54). The vane  $i$  and  $i - 1$  are separated by the angular pitch  $\varphi_{vp}$ .

$$\varphi_{tvb} = \frac{t_{vb}}{2(L(\varphi) - h_v)} \simeq \frac{t_{vb}}{L(\varphi)_{max} + L(\varphi)_{min} - 2h_v} \quad (3.54)$$

Several angular regions are taken into account in the subroutine but, for the sake of brevity, only the area calculation in the carving region, on a  $yz$  plane and the area calculation in two representative regions of the  $xy$  plane are reported hereafter.

#### Area calculation in the region $\varphi_1 + \varphi_{tvb}/2 < \phi \leq \varphi_2 + \varphi_{tvb}/2$

In the region  $0 < \phi \leq \varphi_1 + \varphi_{tvb}/2$  the exchange area between a control volume and distribution ducts is zero. Once  $\varphi_1$  is totally passed by the vane  $i$ , the fluid can communicate with the outlet by a duct corresponding to a carving section on a  $yz$  plane (see Figure 3.17)

The carving slope on a  $xz$  plane can be calculated as follows:

$$\eta_c = \tan^{-1} \left( \frac{h_{c2} - h_{c1}}{l_c} \right) \quad (3.55)$$

Then, one needs to set a coordinate to guide the calculation with respect to

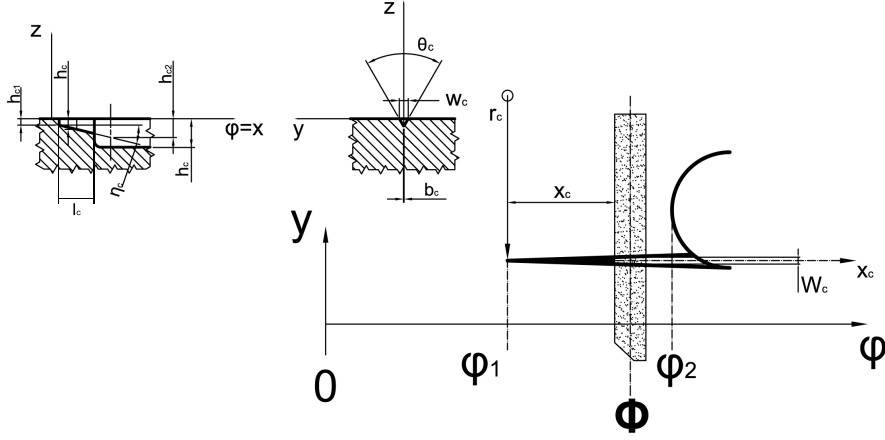


Figure 3.17: Passage area in the carving region.

current angular coordinate  $\phi$ :

$$x_c(\phi) = r_c \left( \phi - \phi_1 - \frac{\varphi_{tvb}}{2} \right) \quad (3.56)$$

Where  $r_c$  represents the radius on which the current carving is lying. The carving depth  $h_c$  and carving width  $W_c$  can now be computed as a function of  $x_c$ :

$$h_c(\phi) = h_{c1} + x_c \tan \eta_c \quad (3.57)$$

$$W_c(\phi) = b_c + 2h_c \tan \left( \frac{\theta_c}{2} \right) \quad (3.58)$$

The effective passage area on a  $yz$  plane can be considered as a trapeze and finally it can be calculated as follows:

$$A_i(\phi) = A_{yz}(\phi) = h_c + \frac{b_c + W_c}{2} \quad (3.59)$$

#### Area calculation in the region $\varphi_2 + \varphi_{tvb}/2 < \phi \leq \varphi_4 + \varphi_{tvb}/2$

In this angular region the passage area can be obtained by adding to the carving contribution on a  $yz$  plane (see previous paragraph,  $A_{yz}$ ) the distribution duct area on a  $xy$  plane ( $A''_{xy}$ ). To calculate this further contribution, some new quantities have to be introduced and a new coordinate  $x'$  has to be used. The angle  $\beta$  represents the angular distance between the  $x$  axis and the line passing on the center of the eyelet circular edge and the intersection between the same edge with the vane back profile.

$$x'(\phi) = r_e(\phi - \varphi_2 - \varphi_{tvb}/2) \quad (3.60)$$

$$\beta = \cos^{-1} \left( 1 - \frac{x'}{r_p} \right) \quad (3.61)$$

The expression for the calculation of area  $A''_{xy}$  in Figure 3.18 can now be obtained. In equation (3.62), the first contribution represents the area of a circular sector included in an angle  $2\beta$ , while the term to subtract is the area of the triangle  $ABC$ . Finally, the effective passage area can be obtained as stated in equation (3.65).

$$A''_{xy}(\phi) = r_p^2(\beta - \sin \beta \cos \beta) \quad (3.62)$$

$$A_i(\phi) = A_{yz}(\phi) + A''_{xy}(\phi) \quad (3.63)$$

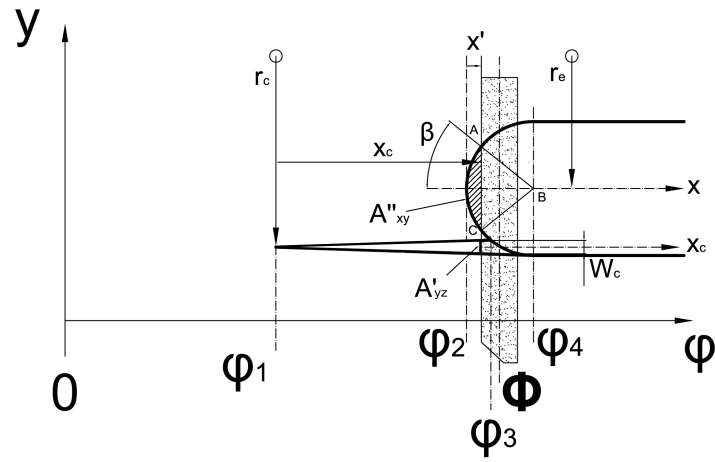


Figure 3.18: Passage area at the beginning of distribution ducts.

#### Area calculation in the region $\varphi_4 + \varphi_{tvb}/2 < \phi \leq \varphi_2 + \varphi_{tvb}/2$

With reference to Figure 3.19, the passage area for the black region can be calculated by means of equation (3.65). The area  $A'''_{xy}$  can be easily computed after having introduced a new coordinate  $x''$  as stated below:

$$x''(\phi) = r_e(\phi - \varphi_4 - \varphi_{tvb}/2) \quad (3.64)$$

$$A_i(\phi) = A_i(\varphi = \varphi_4) + 2x''r_p \quad (3.65)$$

By using the method underlined in the last paragraphs it is possible to calculate the passage area  $A_i(\varphi)$  between a generic vane space control volume  $i$  and inlet or outlet ducts. For the sake of brevity only the procedure for the beginning of a duct has been reported since this region is the most complicated to model. The same method can be applied when a vane space control volume is exiting from inlet/outlet duct. The result for the passage area of the *PHV05* pump is depicted in Figure 3.20. It has been validated as well by comparison with measurements on a *CAD* model.



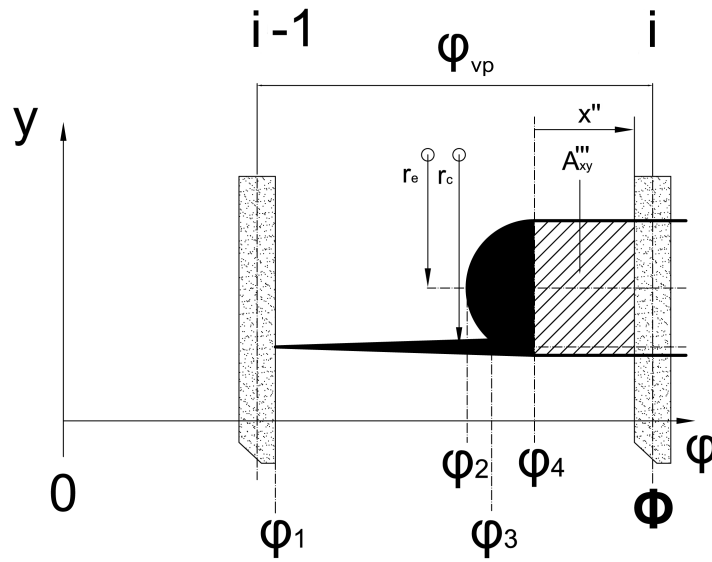


Figure 3.19: Passage area at the beginning of duct constant area region.

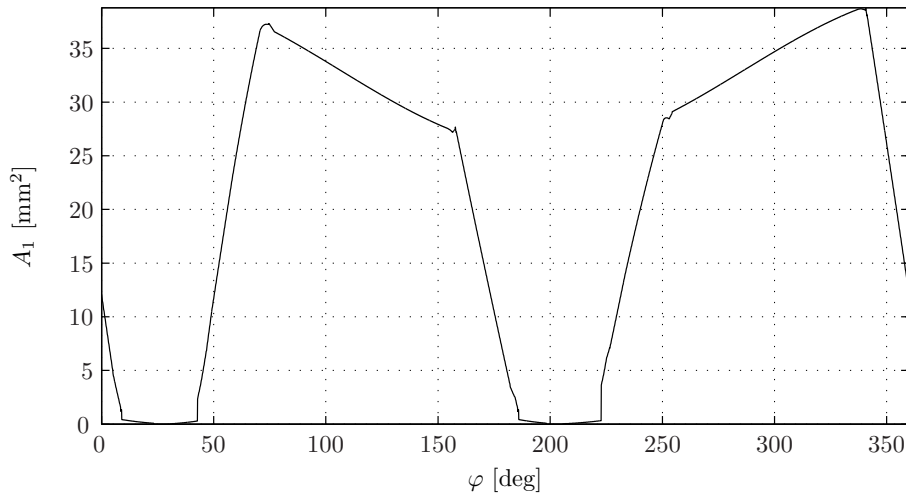


Figure 3.20: Passage area between the vane space  $V_1$  and port plate ducts for a complete shaft rotation.

### 3.3.7 Passage area evolution for a hole control volume

In this section several angular regions will be defined with reference to figure 3.21:

- Carving region: from  $\varphi_1$  to  $\varphi_2$ , from  $\varphi_3$  to  $\varphi_4$  and from  $\varphi_5$  to  $\varphi_6$  the passage area can be represented on a  $yz$  plane as  $A_i(\phi_3)$  in Figure 3.22;
- Full groove region: from  $\varphi_2$  to  $\varphi_3$  and from  $\varphi_6$  to  $\varphi_7$  the passage area can be represented on the  $xy$  plane as depicted for  $A_i(\phi_1)$  and  $A_i(\phi_2)$  in Figure 3.22.

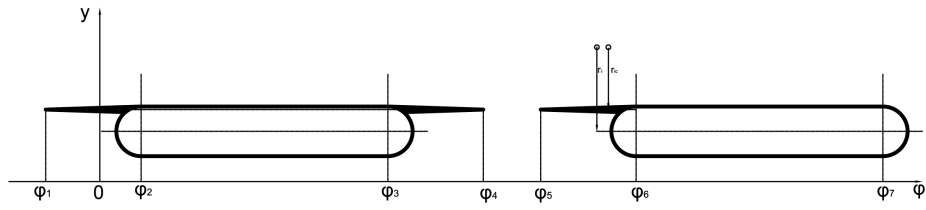


Figure 3.21: Angular regions for the inner distribution.

#### Inner passage area in the carving region

In this regions the passage area can be calculated as described in the previous section, devoted to the description of the procedure used to calculate the passage area for a vane space. First of all the carving radial coordinate has to be defined in a slightly different way, because in this case the carving is located in the inner part of the groove. For a generic carving, the carving radius  $r_{ic}$  can be calculated as follows:

$$r_{ic} = r_i - r_p + \frac{W_{Cmax}}{2} \quad (3.66)$$

Where  $W_{Cmax}$  represents the carving width in correspondence of  $\varphi_2$  (see Figure 3.21). It is now possible to define a linearized coordinate useful to compute the area on the  $yz$  plane:

$$x_{ic}(\phi) = r_{ic}(\phi - \varphi_1) \quad (3.67)$$

The carving depth and the carving width can be calculated as described in the following equations (see equation (3.57):

$$h_{ic}(\phi) = h_{ic1} + x_{ic} \tan \eta_i \quad (3.68)$$

$$W_{ic}(\phi) = b_{ic} + 2h_{ic} \tan \left( \frac{\theta}{2} \right) \quad (3.69)$$

It is now easy to compute the passage area as described in equation (3.70):

$$A_i(\phi) = \frac{(b_{ic} + W_{ic})h_{ic}}{2} \quad (3.70)$$

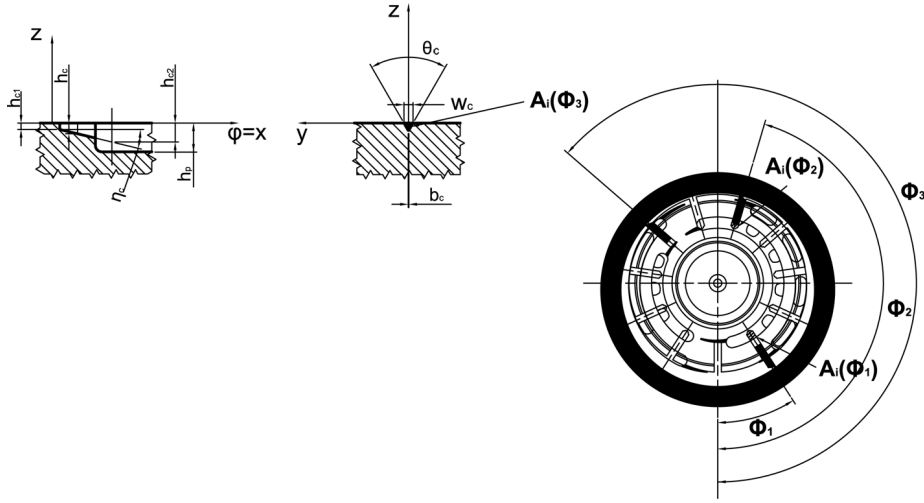


Figure 3.22: The inner exchange area.

### Inner passage area in the full groove region

In this region the passage area between the bottom part of the rotor groove and the distribution groove is a function of pressure ring eccentricity (see figure 3.22). In general one can observe that for some angular coordinates the intersection between the two regions is upper bounded by the distribution groove's width (see  $A_i(\phi_1)$ ) and in some other angular coordinates the passage area on the  $xy$  plane coincides with the area between the bottom of the vane and the bottom of the rotor groove (see  $A_i(\phi_2)$ ).

First of all the distance between the bottom of the vane and the bottom of the rotor groove has to be determined ( $h_{rg}$ ) as stated in equation (3.51) (see Figure 3.14).

The area in the "full groove" region can be calculated using the following equation:

$$A_i(\phi) = \frac{\pi r_f r_g^2}{2} + h_{rg} t_{vb} \quad (3.71)$$

It has to be observed that equation (3.71) can be used only when the relation  $r_i + r_p \geq r_{rg} + h_{rg}$  is verified (the case of  $A_i(\phi_1)$  in Figure 3.22), otherwise (the case of  $A_i(\phi_2)$  in Figure 3.22)  $A_i(\phi)$  must be calculated using the following equation:

$$A_i(\phi) = \pi r_f^2 r_g + (r_i + r_p - r_{rg}) t_{vb} \quad (3.72)$$

The results obtained for the exchange area between a hole control volume and port plate ducts are depicted in Figure 3.23. It has been validated by comparison with measurements on a *CAD* model. The present result refers to the maximum eccentricity condition.

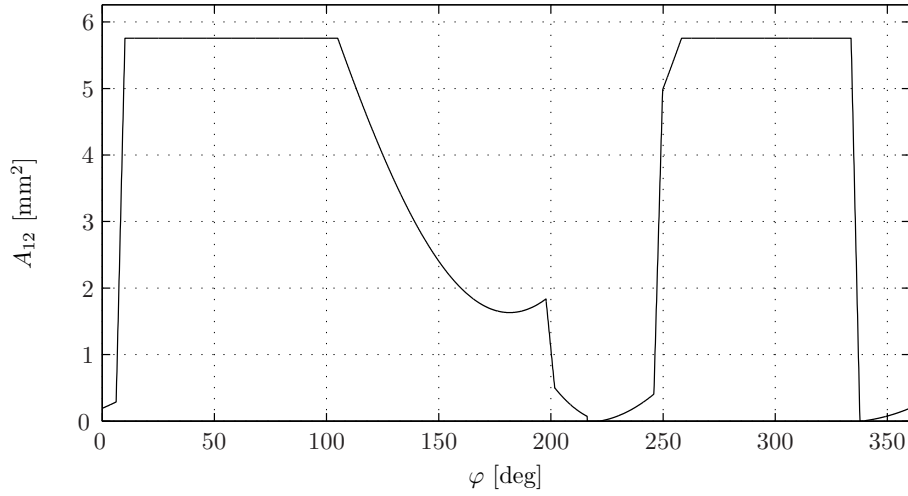


Figure 3.23: Passage area between the hole corresponding to control volume  $V_{12}$  and port plate ducts for a complete shaft rotation.

## 3.4 Force estimation

In the present section the procedures used to determine the forces acting on the rotor shaft will be described. In more detail, quantities  $F_{rotor,x}$ ,  $F_{rotor,y}$ ,  $F_{b,x}$ ,  $F_{b,y}$  involved in equation system (3.2) will be fully characterized.

### 3.4.1 Force acting on the rotor

The pressure distribution inside the vane spaces and inside the holes are used to determine the force acting on the rotor shaft, on a  $xy$  plane, under the following approximations and hypothesis:

- The difference between  $W_r$  and  $W_s$  is neglected ( $W_r \simeq W_s = W_p$ );
- In the meatus between the vanes and the rotor grooves, the pressure difference between the two sides of each vane is neglected;
- The viscous actions in the meatus between vanes and rotor grooves are neglected;
- Direct contact with coulombian friction takes place between vane heads and pressure ring inner race;
- The acceleration of the vane center of mass is approximated to the only centrifugal component.

The force acting on the rotor shaft can be decomposed in two components:

- $F_{rotor,x}$  along  $x$  direction;
- $F_{rotor,y}$  along  $y$  direction.

Both the components are variable with respect to the angular coordinate  $\varphi$  with angular period  $\varphi_{vp}$ .

The forces acting on the on the rotor shaft can be calculated taking into account four main contributions (see equation (3.73)):

- $\mathbf{F}_{sr,i}(\varphi)$  is the contribution due to the pressure evolution inside control volume  $V_i$ , corresponding to a generic vane space (see equation (3.74));
- $\mathbf{F}_{hr,i}(\varphi)$  is the contribution due to the pressure evolution inside control volume  $V_{i+N}$ , corresponding to a generic hole (see equation (3.75));
- $\mathbf{F}_{vr,i}(\varphi)$  is the contribution due to the action of the pressure filed on the vanes along tangential direction (see equation (3.76));
- $\mathbf{F}_{fv,i}(\varphi)$  is the contribution due to friction between vane head and pressure ring inner race (see equation (3.77)).

$$\mathbf{F}_{rotor}(\varphi) = \sum_{i=1}^N (\mathbf{F}_{sr,i}(\varphi) + \mathbf{F}_{hr,i}(\varphi) + \mathbf{F}_{vr,i}(\varphi) + \mathbf{F}_{fv,i}(\varphi)) \quad (3.73)$$

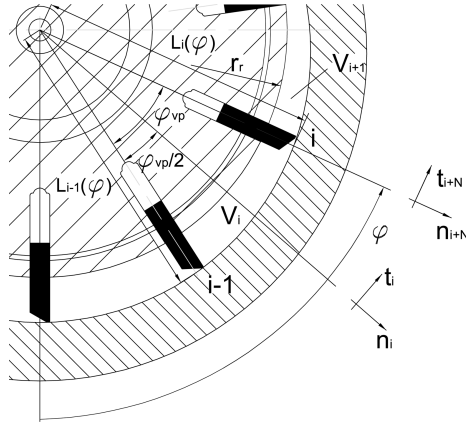


Figure 3.24: Generic geometry used to compute the forces on the rotor shaft.

In the following equations the summation terms of equation (3.73) are described. The meaning of the geometrical features involved in the calculations has been explained in section 2.2.2, while the meaning of unit vectors  $\mathbf{n}_i$ ,  $\mathbf{n}_{i+N}$  and  $\mathbf{t}_{i+N}$  is depicted in Figure 3.24.

$$\begin{aligned} \mathbf{F}_{sr,i}(\varphi) &= -2r_r W_p \mathbf{n}_i \int_0^{\frac{\varphi_{vp}}{2}} p_i(\varphi) \cos\theta d\theta = \\ &= -2p_i(\varphi) r_r W_p \sin\left(\frac{\varphi_{vp}}{2}\right) \mathbf{n}_i \end{aligned} \quad (3.74)$$

$$\mathbf{F}_{hr,i}(\varphi) = -t_{vb} W_p \left( p_{i+N}(\varphi) - \frac{p_i(\varphi) + p_{i+1}(\varphi)}{2} \right) \mathbf{n}_{i+N} \quad (3.75)$$

$$\mathbf{F}_{vr,i}(\varphi) = W_p (L_i(\varphi) - r_r) (p_i(\varphi) - p_{i+1}(\varphi)) \mathbf{t}_{i+N} \quad (3.76)$$

$$\mathbf{F}_{fv,i}(\varphi) = -\mu_f F_{vh,i}(\varphi) \mathbf{t}_{i+N} \quad (3.77)$$

In equation (3.77), quantity  $F_{vh,i}$  represents the magnitude of contact force between the vane head and the pressure ring, while  $\mu_f$  is friction coefficient between vane head and pressure ring (assumed equal to 0.05). The magnitude of this force contribution can be calculated considering the vane equilibrium in radial direction (see Figure 3.25(d)) as stated by equation (3.78), in which  $F_{hole,i}(\varphi)$  represents the force acting on the vane bottom,  $F_{cv,i}(\varphi)$  is the centrifugal force and  $F_{head,i}(\varphi)$  is the force acting on the vane head.

$$F_{vh,i}(\varphi) = F_{hole,i}(\varphi) + F_{cv,i}(\varphi) - F_{head,i}(\varphi) \quad (3.78)$$

$$F_{hole,i}(\varphi) = t_{vb} W_p p_{i+N}(\varphi) \quad (3.79)$$

$$F_{cv,i}(\varphi) = m_v \omega^2 \left( L_i(\varphi) - \frac{h_v}{2} \right) \quad (3.80)$$

$$F_{head,i}(\varphi) = W_p p_i(\varphi) (t_{vb} - t_{vh}) \quad (3.81)$$

### 3.4.2 Journal bearing reaction forces

In equation system (3.2), terms  $F_{b,x}$  and  $F_{b,y}$  can be determined after having analyzed the bearing behavior. The main concepts with an extensive analysis can be found in [7]. All the models that simulate the bearing behavior starts from Reynolds' equation with some simplifications [31]. Commonly, two main simplifications are used: short and long bearing approximation which yield to simple forms of Reynolds' equation. The short bearing theory can be applied to bearings with a  $L/d < 0.5$ , where  $L$  and  $d$  are respectively the bearing length and diameter, and provides good values for the bearing reaction direction but predicts an erroneous large magnitude. On the other hand, the long bearing theory ( $L/d > 1$ ) provides good values for magnitudes but inaccurate values for reactions direction. The solution for short and long bearing can be combined together obtaining an approximate with extended validity range for general finite length bearings with both large and small eccentricity ratios. The vectorial composition of the results obtained with the short and long bearing theories called *finite impedance formulation* has been proposed by Childs et al. in 1977 [7]. The reaction forces of equation system (3.2) have been calculated using this theory as in [2, 32]. In the following, the reaction force  $F_b$  will be obtained for the journal bearing in Figure 3.26. In particular, the bearing reaction forces can be defined as a function of the impedance value  $W$  in order to provide a relationship between the bearing reaction and the position and velocity of the shaft. The bearing reaction forces  $F_b$  can be obtained in a reference frame  $X_b Y_b$  with origin in the centre of the journal bearing as depicted in Figure 3.26 applying the following equations:

$$\begin{cases} F_{b,x} = -2v_s \mu W_b \left( \frac{R_b}{C_r} \right)^3 W_x \\ F_{b,y} = -2v_s \mu W_b \left( \frac{R_b}{C_r} \right)^3 W_y \end{cases} \quad (3.82)$$

In order to calculate the squeeze velocity  $\mathbf{v}_s$  some steps have to be explained.

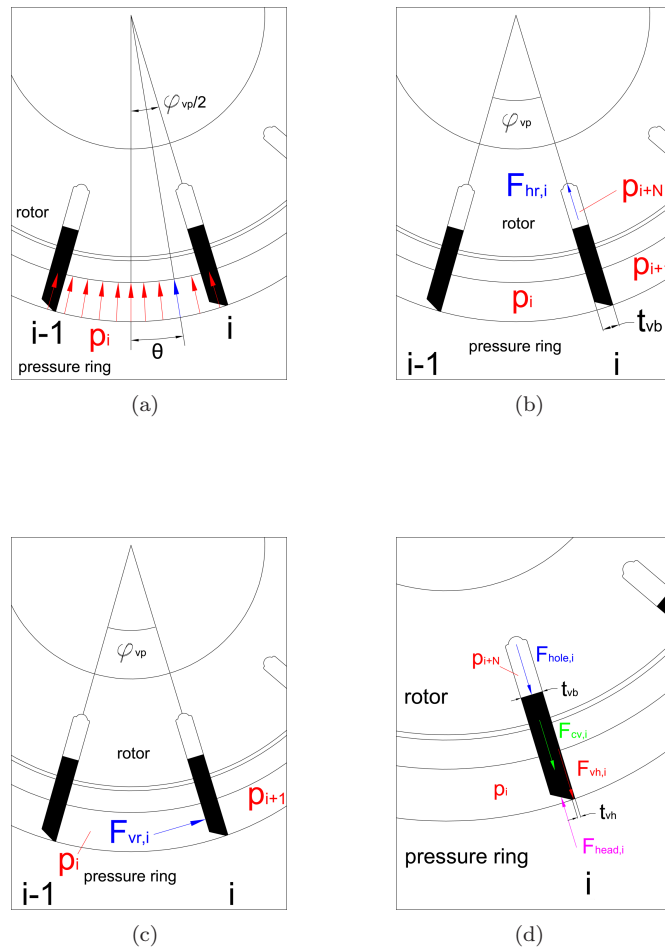


Figure 3.25: The force components taken into account in the calculation of the force acting on the rotor shaft: force due to the pressure evolution in a vane space (a), force due to the pressure evolution in a hole (b), force due to the action of the pressure field on a vane, forces acting on a vane in radial direction.

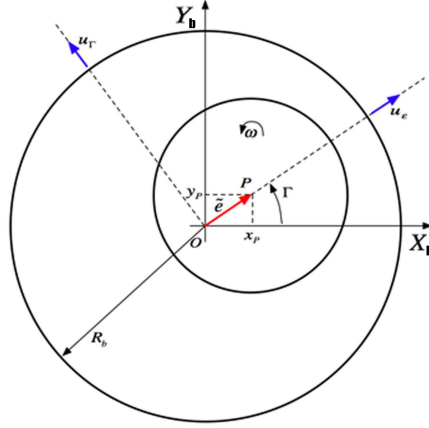


Figure 3.26: Journal bearing scheme,  $P$  is the journal center,  $O$  is the bearing center.  $\bar{\mu}_\epsilon$  and  $\bar{\mu}_\Gamma$  are the unit vector along and normal the eccentricity  $\tilde{e}$ .

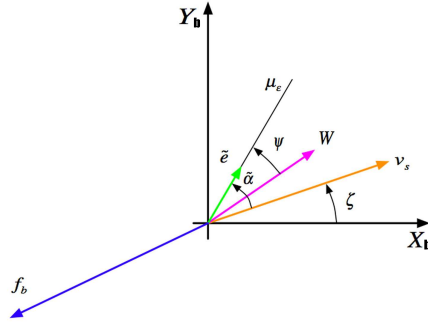


Figure 3.27: Kinematic variables in the journal bearing impedance method.

The velocity of the journal centre relative to the reference frame  $X_b Y_b$  is:

$$\mathbf{v} = \left. \frac{d(\mathbf{C}_r \epsilon)}{dt} \right|_{X_b, Y_b} \quad (3.83)$$

Where the notation  $\left|_{X_b, Y_b}\right.$  means that the temporal derivative is performed for each component of the vector  $\mathbf{C}_r \epsilon$ . Be  $\mathbf{v}_s$  the rate of change of the vector  $\mathbf{C}_r \epsilon$  with respect to a coordinate system that has an angular velocity of  $\omega \mathbf{K}$ , where  $\mathbf{K}$  is the unit vector normal to the  $X_b$  axis and out of the  $X_b Y_b$  plane:

$$\mathbf{v}_s = v - \omega \mathbf{K} \times \mathbf{C}_r \epsilon = \mathbf{u}_\epsilon v_{s\epsilon} + \mathbf{u}_\Gamma v_{s\Gamma} = \mathbf{u}_\epsilon C_r \dot{\epsilon} + \mathbf{u}_\Gamma C_r \dot{\Gamma} \quad (3.84)$$

Where  $v_{s\epsilon}$  and  $v_{s\Gamma}$  are the components of  $\mathbf{v}_s$  along the axis  $\mathbf{u}_\epsilon$  and  $\mathbf{u}_\Gamma$  respectively. Hence the terms  $C_r \dot{\epsilon}$  and  $C_r \dot{\Gamma}$  of equation (3.84) are the velocity components of the journal center with respect to a coordinate system that is rotating at an angular velocity of  $\omega \mathbf{K}$  relative to the reference frame  $X_b Y_b$ . The journal center of motion for this kind of rotating coordinate system would always appear to be in a state of pure squeeze velocity vector [33]. Hence the



vector  $\mathbf{v}_s$  can be denoted here as the journal pure squeeze velocity vector. Such a velocity vector is defined in the  $X_b Y_b$  reference system by:

$$\mathbf{v}_s = v_{s,X_b} \mathbf{I} + v_{s,Y_b} \mathbf{J} = (\dot{x}_p + y_p \omega) \mathbf{I} + (\dot{y}_p + x_p \omega) \mathbf{J} \quad (3.85)$$

Where  $\mathbf{I}$  and  $\mathbf{J}$  are the unit vector along the  $X_b$  and  $Y_b$  axis. The velocity magnitude can be calculated using equation (3.85), therefore:

$$|\mathbf{v}_s| = \sqrt{C_r \dot{\epsilon} + C_r \epsilon (\dot{\Gamma} - \omega)} \quad (3.86)$$

Quantity  $\dot{\epsilon}$  and  $\dot{\Gamma}$  are the derivatives of  $\epsilon$  and  $\Gamma$  respectively:

$$\dot{\epsilon} = \frac{x_p \dot{x}_p + y_p \dot{y}_p}{C_r \sqrt{x_p^2 + y_p^2}} x_p^2 + y_p^2 \quad (3.87)$$

$$\dot{\Gamma} = \frac{x_p \dot{x}_p - y_p \dot{y}_p}{x_p^2 + y_p^2} \quad (3.88)$$

The impedance magnitude in the  $X_b Y_b$  reference frame is:

$$W_x = W \cos(\zeta + \tilde{\alpha} - \psi) \quad (3.89)$$

$$W_y = W \sin(\zeta + \tilde{\alpha} - \psi) \quad (3.90)$$

The angle  $\zeta$  is the attitude angle of  $v_s$  relative to  $\mathbf{I}$ . It can be evaluated using equation (3.91) (see Figure 3.27):

$$\zeta = \tan^{-1} \frac{v_{s,Y_b}}{v_{s,X_b}} = \tan^{-1} \frac{C_r (\dot{\Gamma} - \omega)}{C_r \omega} \quad (3.91)$$

While the angle  $\tilde{\alpha}$ , attitude angle of  $\epsilon$  relative to  $\mathbf{v}_s$  can be calculated using equation (3.92).

$$\tilde{\alpha} = \tan^{-1} \frac{v_{s,Y_b}}{v_{s,X_b}} = \tan^{-1} \frac{C_r (\dot{\Gamma} - \omega)}{C_r \omega} \quad (3.92)$$

The angle  $\psi$  can be obtained solving a transcendental equation, but the following approximate equations can be used as well.

$$\begin{aligned} \psi \cong & \left( 1 - \frac{\tilde{a}}{\sqrt{1 - \tilde{b}^2}} \right) \\ & \left( \sin^{-1} \tilde{b} - \frac{\pi}{2} \frac{\tilde{b}}{|\tilde{b}^2|} + \tan^{-1} \frac{4(1 + 2.12B)\sqrt{1 - \tilde{b}^2}}{3\tilde{b}(1 + 3.6B)} \right) + \\ & + \tilde{\alpha} - \sin^{-1} 1(\tilde{b}) \end{aligned} \quad (3.93)$$

with:

$$B = (1 - \epsilon^2) \left( \frac{L_b}{2d_b} \right) \quad (3.94)$$

$$\tilde{a} = \epsilon \cos \tilde{\alpha} \quad (3.95)$$

$$\tilde{b} = \epsilon \sin \tilde{\alpha} \quad (3.96)$$

The magnitude of the impedance previously reported in equations (3.89) and (3.90) is:

$$W = \frac{1}{0.15\sqrt{\tilde{E}^2 + \tilde{G}^2} (1 - \tilde{a}')^{3/2}} \quad (3.97)$$

In wich:

$$\left\{ \begin{array}{l} \tilde{E} = 1 + 2.12\tilde{Q} \\ \tilde{G} = \frac{3b'(1+3.6\tilde{Q})}{4(1-\zeta)} \\ \tilde{Q} = (1 - a') \left( \frac{L_b}{d_b} \right)^{-2} \\ a' = \epsilon \cos \psi \\ b' = \epsilon \sin \psi \end{array} \right. \quad (3.98)$$

Finally the generic journal bearing reaction force can be written in a synthetic form as follows:

$$F_b = f(x_p, y_p, \dot{x}_p, \dot{y}_p) \quad (3.99)$$

## 3.5 Torque estimation

### 3.5.1 Torque due to pressure distribution

The pressure field inside the pump generates not only variable forces but also a variable torque acting on the rotor shaft. While forces act on the pump body generating vibrations, the variable torque action reflects in variation of angular velocity  $\omega$  (see section 3.1). The pressure distribution generates a pressure torque acting on the rotor shaft called  $M_p(\varphi)$  (see equation system (3.2)).

In more detail, the pressure torque is related to the pressure difference acting on consecutive vanes. Following the scheme used to calculate the pressure field, the vane  $i$  is surrounded at his right by the vane space control volume  $i+1$  and at his left by the vane space control volume  $i$  (see Figure 3.16). In this frame the pressure difference seen by vane  $i$  can be written as follows:

$$\Delta p_i(\varphi) = p_i(\varphi) - p_{i+1}(\varphi) \quad (3.100)$$

Using this convention it will be possible to get positive value for  $M_p$  when it is in concordance with rotational velocity  $\omega$ . In a general way  $M_{p,i}$  can be calculated as proposed in equation (3.101).

$$M_{p,i}(\varphi) = W_r \int_{r_r}^{L_i(\varphi)} r \Delta p_i dr \quad (3.101)$$

Integrating equation (3.101) it is possible to obtain the following expression:

$$M_{p,i}(\varphi) = \frac{W_r (p_i(\varphi) - p_{i+1}(\varphi)) (L_i(\varphi)^2 - r_r^2)}{2} \quad (3.102)$$

Finally, the total amount of pressure torque can be obtained summing the contributions of each vane:

$$M_p(\varphi) = \sum_{i=1}^N M_{p,i}(\varphi) \quad (3.103)$$

### 3.5.2 Friction torque

The contact force between vanes head and pressure ring generates a friction torque called  $M_{vh}(\varphi)$  (see equation system (3.2)). In section 3.4.1 the coupling between each vane  $i$  and pressure ring has been described in terms of force  $F_{vh,i}$  (see equation (3.78) and Figure 3.25(d)). By using the above mentioned formulation it is now easy to calculate the total amount of friction torque due to contact force  $F_{vh,i}(\varphi)$  acting between each vane and the pressure ring inner race as follows.

$$M_{vh}(\varphi) = - \sum_{i=1}^N \mu_f L_i(\varphi) F_{vh,i}(\varphi) \quad (3.104)$$

In equation (3.104)  $\mu_f$  represents the friction coefficients between vane head and pressure ring inner race. It is assumed equal to 0.05.

### 3.5.3 Torque due to viscous actions

The torque due to viscous actions is mainly related to journal bearings behavior ( $M_b$ ) and to coupling between rotor shaft and port plates ( $M_v$ ).

$$M_{vd} = M_v + M_b \quad (3.105)$$

#### Viscous torque between rotor flanks and port plates

The viscous torque generated by lubricant tangential action between rotor flanks and port plates can be calculated as follows:

$$M_v = -2 \int_{r_s}^{r_{sr}} r \mu \left. \frac{\partial v_p}{\partial z} \right|_{z=h_d} 2\pi r dr \quad (3.106)$$

In equation (3.106) the term  $\left. \frac{\partial v_p}{\partial z} \right|_{z=h_d} = \frac{r\omega}{h_d}$  represents the tangential velocity gradient in correspondence of port plates. The distance between between rotor flanks and port plates is equal to the clearance between these two components ( $h_d$ ). After the integration, the viscous torque can be directly calculated as stated in equation (3.108).

$$M_v = - \frac{\mu\pi\omega (r_{sr}^4 - r_s^4)}{h_d} \quad (3.107)$$

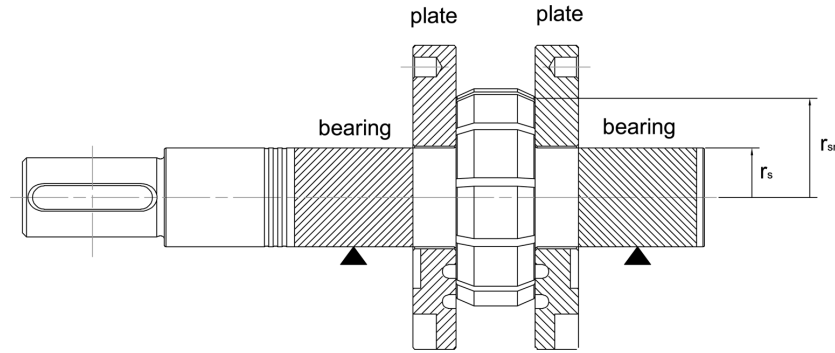


Figure 3.28: The coupling between rotor flanks and port plates.

### Journal bearings viscous torque

Viscous actions generates a constant torque  $M_{vd}$  (see equation system (3.2)) in correspondence of journal bearings and of the coupling between rotor flanks and port plates. The journal bearings viscous torque can be calculated by applying the Raimondi and Boyd theory [34–36]. In general the journal bearing viscous torque can be calculated as follows:

$$M_b = -2\bar{F}_{rotor}f_b r_s \quad (3.108)$$

Where  $\bar{F}_{rotor}$  represents the mean journal bearing load and  $f_b$  is the journal bearing friction coefficient. This last quantity can be calculated as reported in equation (3.109).

$$f_b = f_b^* \frac{C_r}{2r_s} \quad (3.109)$$

In wich  $C_r$  represents the journal bearing radial clearance and  $f_b^*$  can be calculated by diagrams in function of Sommerfeld number.

### 3.5.4 Motor drive torque

The term  $M_m$  in equation system (3.2) represents the motor torque and can be calculated as reported in equation (3.110),

$$M_m(\varphi) = K_T (\varphi_0 - \varphi) + C_T (\dot{\varphi}_0 - \dot{\varphi}) \quad (3.110)$$

in which, quantities  $K_T$  and  $C_T$  are respectively the shaft torsional stiffness and dumping,  $\dot{\varphi}_0$  represents the constant angular speed  $\omega$  and  $\varphi_0$  is the angular position ( $\varphi_0 = \omega t$ , where  $t$  represents the time integration variable). The torsional stiffness can be calculated considering the rotor shaft as two series spring elements of lengths  $l_1$  and  $l_2$  and diameters  $d_1$  and  $d_2$  respectively (see Figure 3.29). It has to be noticed that only half a length of the key is taken into account because in working condition only this part is involved in torque transmission.

$$K_{T,j} = \frac{\pi G d_j^4}{32 l_j} \quad (3.111)$$

The stiffness of the  $j^{th}$  element can be calculated as proposed in equation (3.111), in which  $G$  represents the shear modulus [37], while equivalent torsional stiffness of the rotor shaft can be calculated as follows:

$$K_T = \frac{1}{\sum_{j=1}^2 \frac{1}{K_{T,j}}} \quad (3.112)$$

Finally, the proportional damping can be calculated multiplying the stiffness  $K_T$  by the proportional damping factor  $\gamma_T$

$$C_T = \gamma_T K_T \quad (3.113)$$

The teeth joint between the pump and the drive motor can be considered infinitely rigid with respect to rotor shaft. For this reason the teeth joint stiffness is not taken into account while calculating the equivalent stiffness by equation (3.112) and the joint angular velocity in working condition can be considered as constant and equal to  $\omega$ .

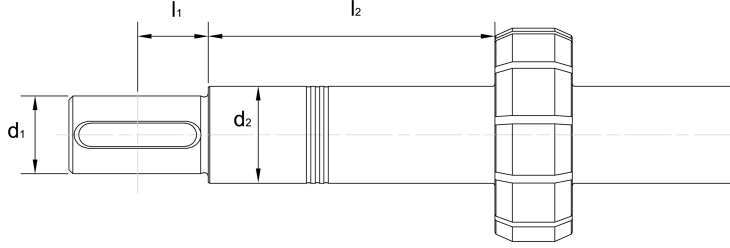


Figure 3.29: The rotor shaft.

### 3.6 The static equilibrium position

With the aim at reducing the integration time, the rotor shaft axis average position inside the journal bearings is estimated before the integration of the dynamic model described by equations of motion (see equation system (3.2)). When the rotor shaft center is in the stationary position, the shaft centre velocity vanishes and the problem is to solve a non linear equation system giving the shaft center position. In this sight the forces acting on the rotor assume the mean value on a revolution. When the integration begins, an arbitrary shaft location is defined  $(x_0, y_0)$ , then the bearing reaction is calculated and finally the shaft center position  $(x_k, y_k)$  can be calculated solving the non linear equation system (3.114). The equation system (3.2) can be further simplified as follows since  $\ddot{x} = 0$  and  $\ddot{y} = 0$ .

$$\begin{cases} 2F_{b,x}(x_k, y_k, 0, 0, \omega) + \overline{F}_{rotor,x}(x_0, y_0) = 0 \\ 2F_{b,y}(x_k, y_k, 0, 0, \omega) + \overline{F}_{rotor,y}(x_0, y_0) = 0 \end{cases} \quad (3.114)$$

Obviously the new center position  $(x_k, y_k)$  will be different from the initial position  $(x_0, y_0)$  and the pressure force evolution for the new position must be recalculated repeating the same procedure described above until the difference

between two consecutive positions is less than a threshold value. An additional control has been included to take into account the mean force variation between two consecutive iterations. In working condition, the rotor shaft center will describe an orbit around the stationary equilibrium position.

Since the rotor shaft position and the pressure field are mutually dependent, to perform the calculation depicted in the present chapter the iterative procedure depicted in Figure 3.30 has been used. Thus, the variable pressure force on the rotor can be approximately estimated from the stationary equilibrium position before starting the numerical integration, obtaining an important reduction of the integration time. The goodness of this approach has been verified as well. It is well known that during pump working, the rotor shaft position is not fixed in the stationary center location, but the rotor shaft covers an orbit around this position as shown in Figure 3.31. The validation procedure will be described in the next chapter.

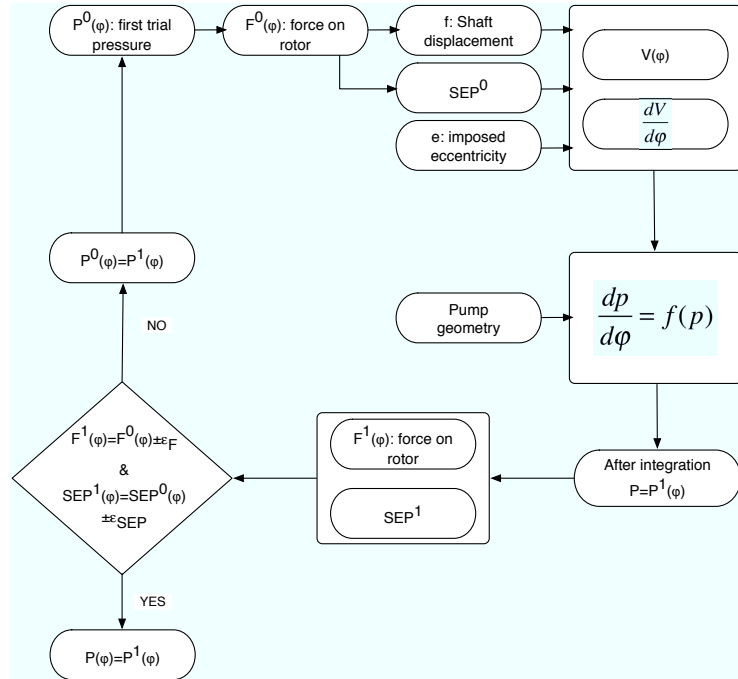


Figure 3.30: Pressure and force calculation loop.

### 3.7 Preliminary analysis

With the aim to demonstrate the consistency of the model scheme chosen to evaluate the rotor shaft dynamical behavior, two preliminary analyses have been done using *ANSYS workbench* [38]. The first is a finite element structural analysis useful to verify the shaft rotation in correspondence of the journal bearings. The rotor shaft has been loaded as depicted in Figure 3.32, in which the force  $\bar{F}_{rotor}$  is the average value of the force acting on the rotor in working condition. Three constraint conditions have been investigated:

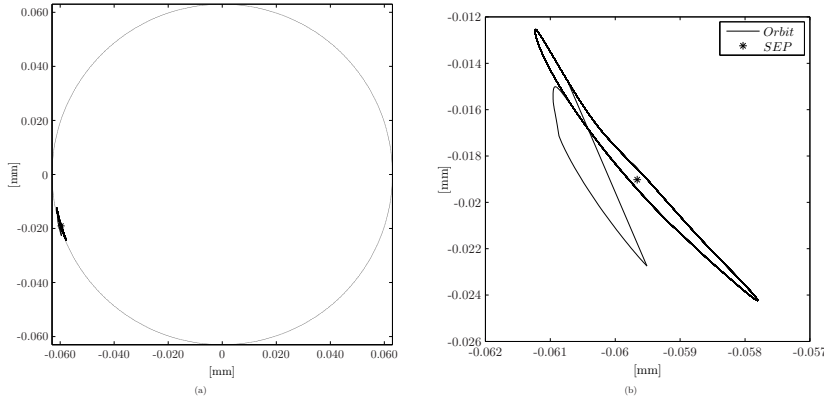


Figure 3.31: The *SEP* position with respect to journal bearing radial clearance (a) and the shaft orbit around the *SEP* (b).

- Condition 1: Two constraints in correspondence of the journal bearings middle axis (see Figure 3.32a);
- Condition 2: Two constraints with length equal to  $W_b/2$ , centered on the journal bearings middle axis (see Figure 3.32b);
- Condition 3: Two constraints as extended as the journal bearings (see Figure 3.32c).

The deflection angle in correspondence of each constraint has been calculated for each constraint condition as resumed in Table 3.1. As expected, the first constraint condition leads to the biggest angular deflection. It has to be verified if the displacement due to the deflection is compatible with the *SEP* value described in Figure 3.31 and with the journal bearing clearance as reported in equation (3.115), in which quantity  $C_r$  represents the journal bearing radial clearance, quantity *SEP* (see section 3.6) refers to journal bearing static equilibrium position and  $\delta_s$  is the shaft displacement in correspondence of journal bearing edge (see Figure 3.33). It can be noticed that in working condition the clearance between the rotor axis and the bearing is reduced to  $2 \cdot 10^{-3}$  mm. This clearance value is comparable with the material roughness value and this fact justifies the scratches clearly visible on used journals. Nevertheless, the more the journal bearing meatus decreases, the more the reaction force increase, for this reason a further finite element dynamical analysis has been performed choosing a different constraint condition. The goal of this new analysis is to verify if the natural frequencies of the rotor shaft in working condition are in the range of excitation forces that varies with a frequency equal to  $\frac{\omega N}{2\pi}$  and relative first two harmonics. The rotor shaft has been now constrained by three cylindrical constraints in correspondence of the journal bearings axis and in correspondence of the shaft terminal. The constraints in correspondence of journal bearing axis have axial extension equal to  $W_b/2$  (see Figure 3.34). In this way rotations around the rotor axis and translations in the rotor axis directions are allowed. The simulation parameters are resumed in Table 3.2 and the meshed geometry is depicted in Figure 3.35. The first two flexural modes are depicted in Figures 3.36 and 3.37. The first flexural mode is at the frequency of 13838 Hz and it

is characterized by more relevant displacement in correspondence of the rotor region, between the two journal bearings, while the second mode is at the frequency of 16641 Hz and it is characterized by more relevant displacement in the shaft region included between the journal bearing and the terminal. Both the modes are not excited by the forces acting on the rotor shaft in working condition. For this reason the dynamical model scheme resumed in section 3.1 can be considered suitable for the analysis target.

$$C_b = C - SEP - \delta_s = 2 \cdot 10^{-3} mm \quad (3.115)$$

Table 3.1: Deflection angle in correspondence of constraints.

Constraint condition	$\alpha$ [deg]
Condition 1	0.006 deg
Condition 2	0.005 deg
Condition 3	0.005 deg

Table 3.2: Finite element dynamic simulation parameters.

Young modulus	$2.1 \cdot 10^{11}$ Pa
Poisson ratio	0.3
Material density	7850 kg/m <sup>3</sup>
Yield strength	$2.5 \cdot 10^8$ Pa
Ultimate tensile strength	$4.6 \cdot 10^8$ Pa
Element kind	Tetrahedral
Number of elements	120922
Number of nodes	72690



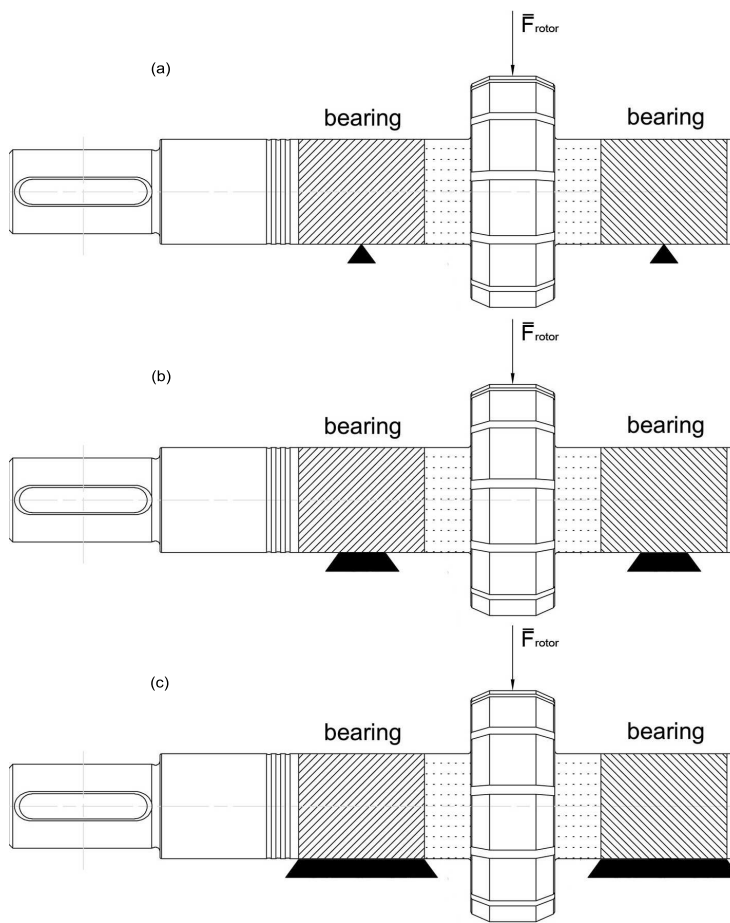


Figure 3.32: The constraint condition 1 (a), the constraint condition 2 (b) and the constraint condition 3 (c).

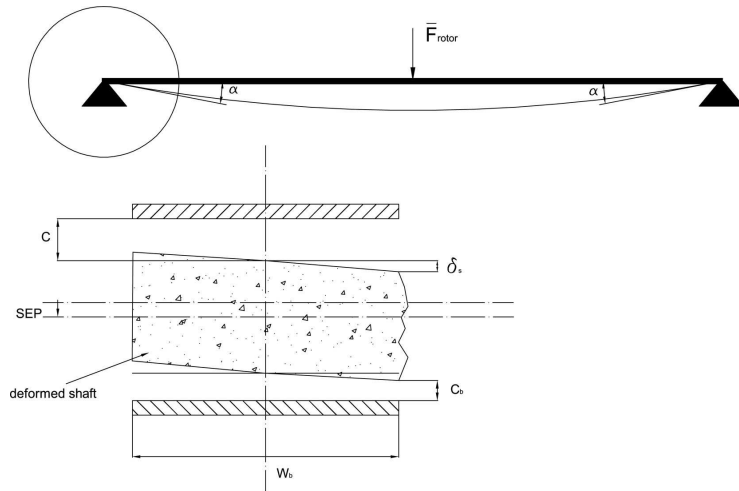


Figure 3.33: The rotor shaft deflection and the journal bearing in constraint condition 1.

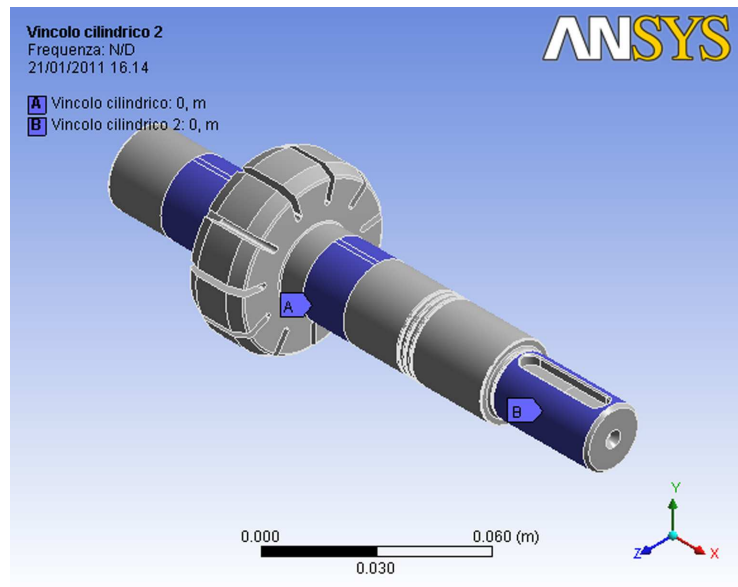


Figure 3.34: The cylindrical constraints used for the finite element dynamical analysis.

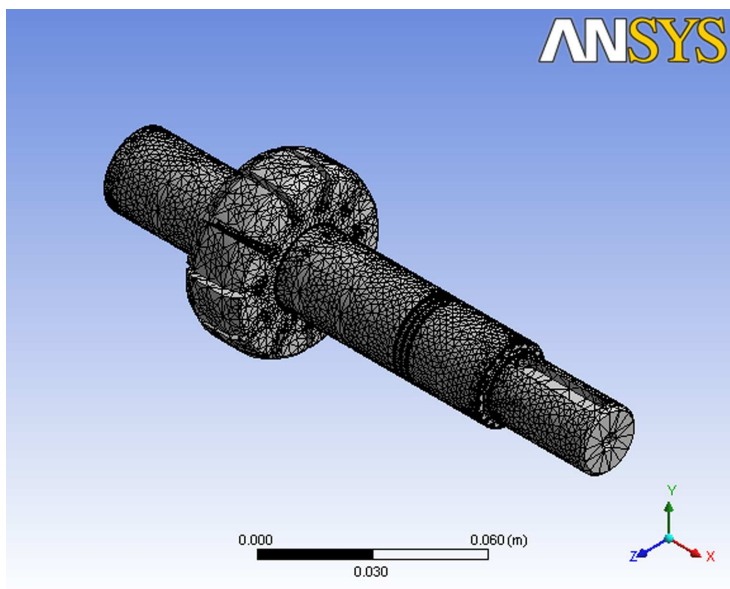


Figure 3.35: The meshed geometry used for the finite element dynamical analysis.

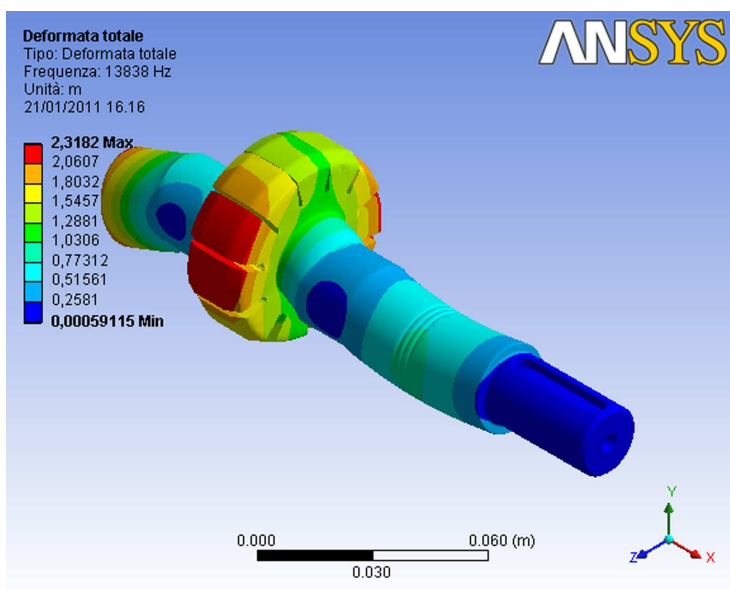


Figure 3.36: The first flexural mode (13838 Hz).

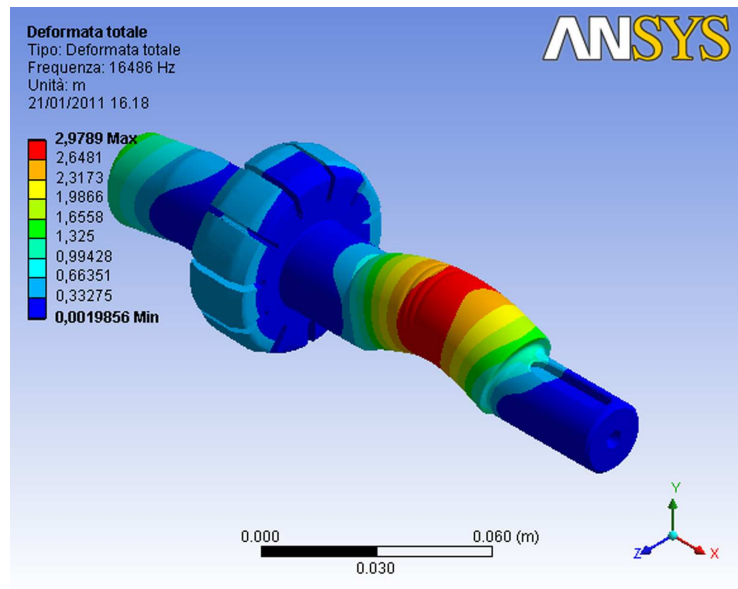


Figure 3.37: The second flexural mode (16486 Hz).

## Chapter 4

# Model implementation in MATLAB and Simulink

*In the present chapter the most important aspects related to the model implementation will be reported following the scheme previously used in Chapter 3. First of all a general description of the LP model will be provided, hence the implementation in Simulink and MATLAB environments will be described.*

### 4.1 Integration of the equations of motion

The system of equation of motion reported in (3.2) has been integrated in Simulink environment. First of all, the system has to be rewritten in the following form:

$$\begin{cases} \ddot{x} = \frac{2F_{b,x}}{m} + \frac{F_{rotor,x}}{m} \\ \ddot{y} = \frac{2F_{b,y}}{m} + \frac{F_{rotor,y}}{m} \\ \ddot{\varphi} = \frac{M_m}{J} + \frac{M_p}{J} + \frac{M_{vh}}{J} + \frac{M_{vd}}{J} \end{cases} \quad (4.1)$$

The right arguments of equation system (4.1) have been fully characterized in sections 3.4 and 3.5 from a theoretic point of view. Terms  $F_{b,x}$ ,  $F_{rotor,x}$ ,  $F_{b,y}$ ,  $F_{rotor,y}$ ,  $M_p$ ,  $M_{vh}$ ,  $M_{vd}$  can be calculated by means of MATLAB subroutines described in the next section and then evaluated in the Simulink flowchart by using the embedded block *MATLAB Fcn*. This block passes the input values obtained during the Simulink calculations to a MATLAB function for the evaluation and finally imports the results in the Simulink flowchart.

The motor drive torque  $M_m$  (see section 3.5.4) is directly calculated inside a Simulink block described in next sections.

Before launching the Simulink equilibrium model it is necessary to launch the MATLAB function *full\_model.m* (see section 4.2) and save all the variables in the current workspace. This preliminary operation makes it possible to compute all the pressure forces and torques in the stationary equilibrium position (*SEP*) following the loop depicted in Figure 3.30.

The rotor shaft equilibrium problem involves the integration of equations of motion along three degrees of freedom:  $x$ ,  $y$  and  $\varphi$ . First of all it has to be noticed that degrees of freedom  $x$  and  $y$  are coupled while degree of freedom

$\varphi$  can be integrated separately. The whole integration operation is performed by the Simulink model called *rotor\_equilibrium\_look\_up.mdl* (see Figure 4.1). Since a second order problem has to be solved, two integrations are needed as depicted in Figure 4.2, and for each one a set of initial condition in terms of displacement and velocities must be provided. In more detail, the displacements and velocities at  $t = 0$  has been set as reported in Table 4.1.

The simulation main parameters have been set by means of the Simulink dialog box as depicted in Figure 4.3. A variable step solver suitably developed for stiff problems has been used (*ode15s*) and the simulation has been performed for several shaft rotations to reach the equilibrium of the integration process (see the *Stop time* parameter in the dialog box). In more detail, the integration total period used during calculations corresponds to 10 complete shaft rotations. As a matter of fact the first iterations are necessary to reach the equilibrium and for this reasons their results must be discarded.

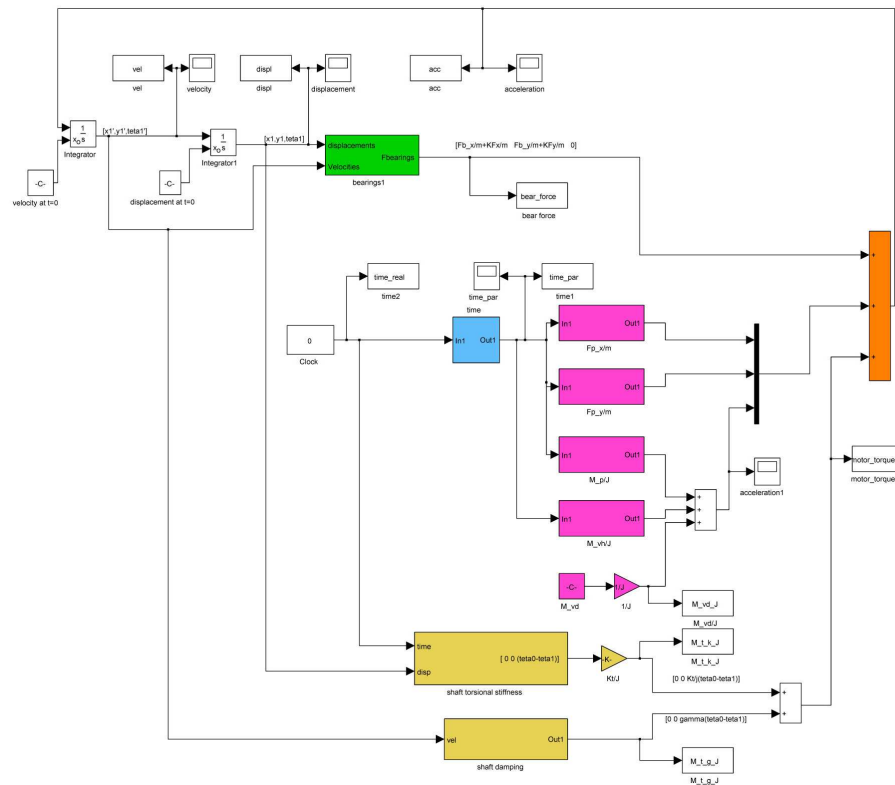


Figure 4.1: Simulink flow chart of the rotor shaft equilibrium problem. The model file is called *rotor\_equilibrium\_look\_up.mdl*.

Velocities and displacements obtained after each integration step are the input data for the blocks devoted to journal bearing reaction forces  $F_{b,x}$  and  $F_{b,y}$  and motor drive torque  $M_m$  (respectively green and yellow block in Figure 4.1). The journal bearing resulting reaction has been calculated by implementing the Childs' theory exposed in section 3.4.2 in a MATLAB subroutines that uses as input data velocities and displacements along  $x$  and  $y$  coordinate as well as

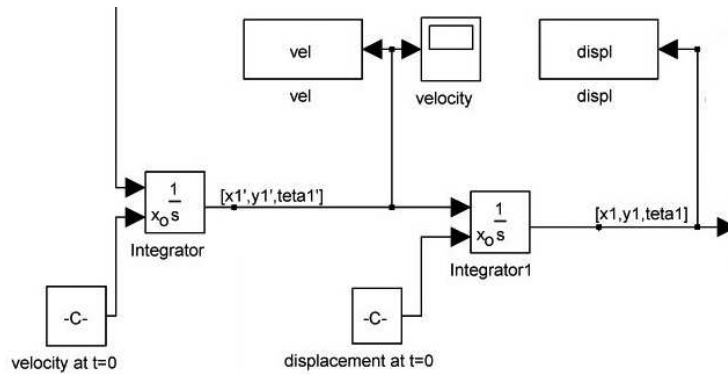


Figure 4.2: Detail of *rotor\_equilibrium\_look\_up.mdl*: the integrators.

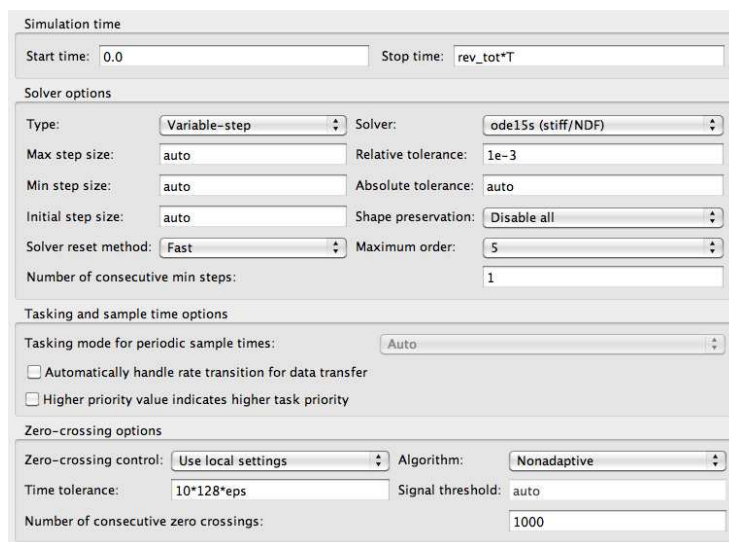


Figure 4.3: Integration parameters in the Simulink dialog box.

Table 4.1: Initial conditions in terms of displacements and velocities for the integration of the rotor shaft equilibrium problem.

Degree of freedom	Displacement i. c.	Velocity i. c.
$x$	$SEP_x$	0
$y$	$SEP_y$	0
$\varphi$	0	$\omega$

rotational velocity  $\omega$ , lubricant characteristics in terms of dynamic viscosity and journal bearings geometrical features  $R_b$ ,  $W_b$  and  $C_r$ .

The motor drive torque can be calculated by using the yellow blocks in which the formulation of equation (3.110) in section 3.5.4 is simply implemented. In Figure 4.4 the implementation of the term  $(\varphi_0 - \varphi)$  is depicted. It can be noticed that the a time input is necessary to compute the term  $\varphi_0 = \omega t$ . Since the integration takes place in the time domain corresponding to the angular domain from  $\varphi = 0$  to  $\varphi = \varphi_{vp}$ , a periodic time have been used. The periodic time calculation is performed by the blue block of Figure 4.1 whose inner structure is depicted in Figure 4.5. The time generated by the clock block first of all is divided by the period  $T$ , equivalent to a vane pitch (see equation (4.2)), consequently it is multiplied for the same quantity. In this way the periodic time depicted in Figure 4.6 is obtained. It can be noticed that the periodic time varies from 0 to  $3.6 \cdot 10^{-3}$  that is the time necessary to complete a rotation from  $\varphi = 0$  to  $\varphi = \varphi_{vp}$  at 1500 rpm, i.e. the typical pump rotational speed.

$$T = \frac{2\pi}{\omega N} \quad (4.2)$$

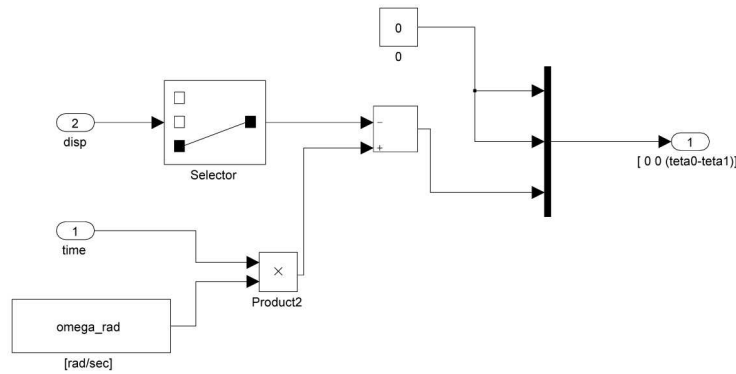


Figure 4.4: Detail of *rotor\_equilibrium\_look\_up.mdl*: a passage for the motor drive torque calculation.

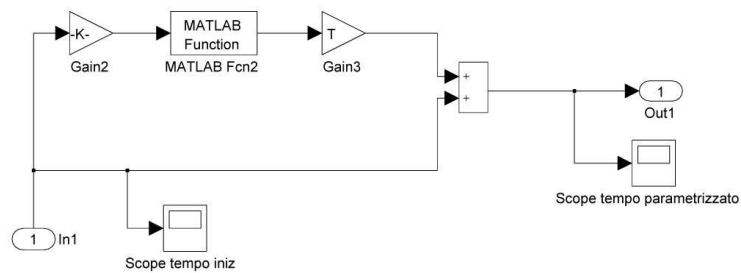


Figure 4.5: Detail of *rotor\_equilibrium\_look\_up.mdl*: the periodic time calculation.

The purple blocks of Figure 4.1 are devoted to introduce in the Simulink flowchart quantities  $F_{rotor,x}$ ,  $F_{rotor,y}$ ,  $M_p$ ,  $M_{vh}$ ,  $M_{vd}$ , previously saved in the work space



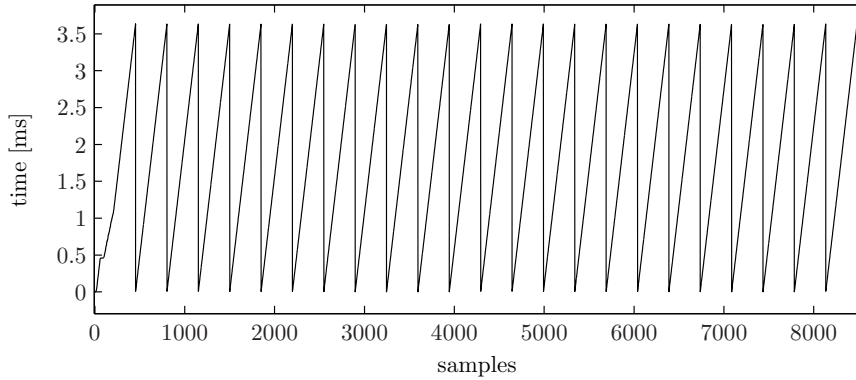


Figure 4.6: The periodic time calculated by the block of Figure 4.5.

after having launched the function *full\_model.m*. By means of *Lookup* blocks a linear interpolation of input values using the specified table is obtained. Extrapolation is performed outside the table boundaries. This tool is necessary since the variable step integrators may need values in correspondence of points in which previous integrations performed by *full\_model.m* did not take place. Finally, each block gives as output a three row vector in which the first column is related to the  $x$  component, the second to the  $y$  component and the third to the  $\varphi$  component. Hence, the output vectors of each block are summed by the orange block of Figure 4.1 to finally compose equation system (4.1).

## 4.2 Pressure and force field calculation

The *LP* model described in the previous section requires input data in terms of forces and torques (see right arguments of equation system (4.1)). All these quantities are provided by subroutines developed in MATLAB environment. All the relations derived in sections 3.2 and 3.3 have been implemented in MATLAB [3, 39]. The loop depicted in Figure 3.30 is solved by a function called *full\_model.m* that includes all the MATLAB functions described in the present section. All the geometry data useful for the calculations (see Chapter 2) are listed in a script called *data.m* in the form of structure arrays. In this way one need to modify only *data.m* if different geometry features have to be evaluated. Inside *full\_model.m* the other main functions are *complete\_look\_up.m*, *pressure\_field.m* and *rotor\_dyn\_force.m*. The first provide values for all the auxiliary quantities underlined in section 3.3 while the second implements the integration of the flow rate balance equation system.

### 4.2.1 The function containing data: *data.m*

As it can be seen in Figures 4.7 - 4.11, the geometry data and operational parameters are saved in the MATLAB workspace as structure array (when possible). In this way a less number of variables is saved and debugging operations are make easier.

```

% Contains all the geometry data and the working condition data.

%%%%%%%%%%%%%%%%%%%%%%%%%%%%%%%%%%%%%%%%%%%%%%%%%%%%%%%%%%%%%%%%%%%%%%%%
%%                               Data                               %%
%%%%%%%%%%%%%%%%%%%%%%%%%%%%%%%%%%%%%%%%%%%%%%%%%%%%%%%%%%%%%%%%%%%%%%%%

%% Generic operators
deg_2_rad=pi/180;
rad_2_deg=180/pi;
mm_2_m=10^-3;
m_2_mm=10^3;
mm3_2_m3=10^-9;

%% Fluid properties
mou=0.014; % dynamic viscosity [Pa*s]
bu=1.7237*10^9; % bulk modulus [Pa]
Va_Vo=0.01; % ratio air volume/oil volume in std conditions
ro=854; % density at 15°C [kg/m^3]
k=0.65; % flow coefficient with the distribution ducts
k_duct=0.65;
k_in=1.5346*10^-4; % flow coefficient for input interface;
% k_out=0.0029; % flow coefficient for output interface;
k_out=0.4*10^-8; % flow coefficient for output interface; 0.9

%% Number of control volumes
NV=30; % []

%% Number of vanes
N=11; % []
% Angular positions used to discretize ta vane pitch
step_number=300; % []
vane.pitch=360/N;
%% Angular velocity
n=1500; % [rpm]
omega=2*pi*n/60; % [rad/s]

omega_rad=omega; % [rad/s]

omega=rad_2_deg*omega; % [deg/s]

T=(60/n)/N; % pitch period [s]
%% Angular vector
% Angular step
delta_angle=360/(N*step_number); % [deg]
% Vector of angles
FI=[0:delta_angle:(720-delta_angle)]; % [deg]
FI_half=FI(1:length(FI)/2); % [deg]
FI_vp=FI(1:step_number); % [deg]

%% Pressure
P_in=100000; %Inlet pressure [Pa]
P_out=24000000; %Outlet Pressure [Pa]
P_d=100000; %drenaige pressure [Pa]
P_atm=100000; %external pressure [Pa]

```

Figure 4.7: The input data for the models (p. 1).

```
%% Inlet
external_inlet.width=3.5; %[mm]
external_inlet.depth=3.5; %[mm]
external_inlet.radius=25.8; %[mm]
external_inlet.start_angle=224.1; % deg
external_inlet.end_angle=334.8; % deg

internal_inlet.width=3.5; %[mm]
internal_inlet.depth=3.5; %[mm]
internal_inlet.radius=18.75; %[mm]
internal_inlet.start_angle=246.5; % deg
internal_inlet.end_angle=330.5; % deg

external_inlet.interface=236.091; % [mm^2]
external_inlet.interface_number=1;
%% Outlet
external_outlet.width=3.5; %[mm]
external_outlet.depth=10; %[mm]
external_outlet.radius=25.8; %[mm]
external_outlet.start_angle=44.3; % deg
external_outlet.end_angle=151.8; % deg

internal_outlet.width=3.5; %[mm]
internal_outlet.depth=3.5; %[mm]
internal_outlet.radius=18.75; %[mm]
internal_outlet.start_angle=13.5; % deg
internal_outlet.end_angle=194.5; % deg

external_outlet.interface=69.758; % [mm^2]
external_outlet.interface_number=4;
%% Eccentricity of the external ducts
e_e=0.63; % [mm]

%% Carvings
% (f=1)
carving(1,1).start_angle=28; % [deg]
carving(1,1).end_angle=44.3; % [deg]
% (b=2)
carving(1,2).start_angle=151.8; % [deg]
carving(1,2).end_angle=168; % [deg]
% (a=3)
carving(1,3).start_angle=203; % [deg]
carving(1,3).end_angle=224.1; % [deg]
% (e=4)
carving(1,4).start_angle=334.8; % [deg]
carving(1,4).end_angle=353; % [deg]
% (g=5)
carving(1,5).start_angle=343.5; % [deg]
carving(1,5).end_angle=373.5; % [deg]
% (c=6)
carving(1,6).start_angle=194.5; % [deg]
carving(1,6).end_angle=212.8; % [deg]
% (d=7)
carving(1,7).start_angle=225.2; % [deg]
```

Figure 4.8: The input data for the models (p. 2).

```

carving(1,7).end_angle=246.5; % [deg]

%% Carvings geometry
% Carving (a) (b) (d) (e) (f) (g)
for i=1:5
    carving(1,i).start_depth=0.1; % [mm]
    carving(1,i).end_depth=0.7; % [mm]
    carving(1,i).start_base=0.2; % [mm]
    carving(1,i).theta_splay=60; % [deg]
end
carving(1,7).start_depth=0.1; % [mm]
carving(1,7).end_depth=0.7; % [mm]
carving(1,7).start_base=0.2; % [mm]
carving(1,7).theta_splay=60; % [deg]

% Carving (c)
carving(1,6).start_depth=0.2; % [mm]
carving(1,6).end_depth=0.9; % [mm]
carving(1,6).start_base=0.2; % [mm]
carving(1,6).theta_splay=60; % [deg]

%% Vane geometry
vane.number=11;
vane.bottom_thickness=2.2; % [mm]
vane.head_thickness=0.3; % [mm]
vane.height=8.8; % [mm]
vane.width=20; % [mm]
vane.head_slope=30; % [deg]

%% Rotor geometry
rotor.radius=55/2; % [mm]
rotor.diameter=2*rotor.radius; % [mm]
rotor.side_radius_corner=51/2; % [mm]
rotor.side_diameter_corner=2*rotor.side_radius_corner; % [mm]
rotor.width=20; % [mm]
rotor.side_width=4.5; % [mm]
rotor.middle_width=rotor.width-2*rotor.side_width; % [mm]
rotor.side_slope=30; % [deg]
rotor.side_chamfer=0.3; % [mm]
% Quantity to subtract to the rotor.side_radius_corner
rotor.delta_side_radius=rotor.side_chamfer/(tand(rotor.side_slope)); % [mm]
rotor.side_radius=rotor.side_radius_corner-rotor.delta_side_radius; % [mm]

%% Rotor shaft geometry
rotor.shaft_plate=11; % [mm]
rotor.bearing_width=30; % [mm]
rotor.shaft_diameter=25; % [mm]
rotor.shaft_length_left=43; % [mm]
rotor.shaft_length_right=43; % [mm]
rotor.cut_depth=9.356; % [mm]
rotor.cut_width=2.2; % [mm]
rotor.cut_end_fillet_radius=0.8; % [mm]
rotor.cut_end_radius=18.34; % [mm]
rotor.end_fillet_distance=0.21; % [mm]
rotor.shaft_plate=11; % [mm]

```

Figure 4.9: The input data for the models (p. 3).

```
E=210000*10^6; % [Pa]
ni=0.3; % poisson ratio

%% Duct between the distribution grooves
duct.length=4.931; % [mm]
duct.diameter=3.5; % [mm]
duct.outlet=4; % []
duct.inlet=3; % []

%% Stator geometry
% Eccentricity along the x direction
stator.e_x=0; % [mm]

% Eccentricity along the y direction
%stator.e_y=-0.00213*(P_out/10^5)+2.3626; % [mm]
stator.e_y=-0.55; % [mm] 0.47
stator.inner_radius=30; % [mm]
stator.outer_radius=43.25; % [mm]

stator.inner_race=3; % [mm]

%% Journal bearing data
D_b=25*10^-3; % bearing diameter [m]
L_b=30*10^-3; % bearing length [m]
Cr_max=0.101*10^-3; % max bearing clearance [m]
Cr_min=0.025*10^-3; % min bearing clearance [m]
Cr=(Cr_max+Cr_min)/2;
%% Clearances (measured)
% Berarma
% on the vane flank
h_f=1.3*(0.009+0.014); % [mm] /2
% between the rotor and the distributor
h_dr=(0.5*(0.003+0.014)+0.5*(0.011+0.018));
%h_dr=0.5*(0.5*(0.08+0.123)+0.5*(0.011+0.018)); % [mm]
% between the stator and the distribution
%h_ds=1*(0.003+0.014); % [mm]
h_ds=h_f*0.1; % [mm]
%h_ds=(0.08+0.123)/4; % [mm]
% between the vane and the rotor groove, first vane
h_r_value=(0.005+0.0112); % [mm]
% length between vane and groove
l_g=9.15*10^-3; % [m]
% width between two vanes
w_g=10.9413*10^-3; % [m]
% width between two grooves
w_g_in=8.5788*10^-3; % [m]
% length between groove and shaft
l_g_in=5.038*10^-3; % [m]
% Duct for the drainage of the internal distribution
w_d_out=48.6585*10^-3; % [m]
w_d_in=22.8341*10^-3; % [m]
l_d=2.85*10^-3; % [m]
h_d=h_dr*10^-3; % [m]

%% data required to solve the rotor dynamic equilibrium
```

Figure 4.10: The input data for the models (p. 4).

```

J=174.970*10^-6; % [kgm^2] rotor shaft inertia
m=0.862+11*0.003; % [kg] rotor mass
f_star=1.5; %f=f_star*(C/D)
alfaT=10^-9;
%KT=8.4*10^3; % [Nm/rad]
KT=2.2*10^6; % [Nm/rad]

return

```

Figure 4.11: The input data for the models (p. 5).

## 4.2.2 The function *complete\_look\_up.m*

This script uses as input the script *data.m* and computes all the quantities involved in the integration of equation system (3.17). It includes several sub-routines:

- *pressure\_first\_trial.m*: it uses as input the script *data.m* and gives as output the first trial pressure  $p^0$ ;
- *shaft\_displacement.m*: it uses the pressure evolution  $p$  ( $p^0$  at the first trial) and *data.m* as input. It gives as output the  $x$  and  $y$  components of shaft displacement  $e_{f,x}$  and  $e_{f,y}$  (see section 3.3.1);
- *real\_eccentricity.m*: it uses as input  $e_{f,x}$ ,  $e_{f,y}$ ,  $SEP_x$  and  $SEP_y$  (see section 3.6) and gives as output the total eccentricity between rotor and stator components  $e_{tot,x}$  and  $e_{tot,y}$  (see equation 3.34);
- *volume.m*: it uses *data.m*,  $e_{tot,x}$  and  $e_{tot,y}$  as inputs and gives as output the distance between the rotor center and the pressure ring inner race  $L(\varphi)$  (see section 3.3.2), the volume  $V_i$  (see section 3.3.3), and the rate of volume variation  $\frac{dV_i}{d\varphi}$  (see section 3.3.5);
- *look\_up\_area.m*: uses  $L(\varphi)$  and the script *data.m* as inputs and gives as output the passage area values  $A_i(\varphi)$  for vane spaces (see section 3.3.6) and for holes control volume (see section 3.3.7);
- *inner\_volume.m*: uses as input  $L(\varphi)$  and the script *data.m* and gives as output the volume  $V_i$  and the rate of volume variation  $\frac{dV_i}{d\varphi}$  for holes control volumes (see sections 3.3.4 and 3.3.5);
- *look\_up\_everithingelse.m*: uses as input  $L(\varphi)$  and the script *data.m* and gives as output the clearances meatus dimensions  $h_i$ ,  $b_i$  and  $l_i$ .

All these quantities will be used to define coefficients of equation system (3.17) reported in the previous chapter.

## 4.2.3 The function *pressure\_field.m*

This function uses as input  $L(\varphi)$ ,  $V_i$ ,  $\frac{dV_i}{d\varphi}$ ,  $A_i$ ,  $h_i$ ,  $b_i$ ,  $l_i$  whose physical meaning has been described in previous sections and in the list of symbols. It integrates equation system (3.17) and gives as output the pressure evolution in vane space

control volumes and in holes control volumes. It allows also to save in the workspace the values of the flow rate described in section 3.2. The system of 26 first order non linear *ODE* with non constant coefficients is solved by using the *ODE15s* MATLAB routine that requires the entire system has to be written in a dedicated function, called *system\_26.m*.

#### ***system\_26.m* syntax**

The function must be saved in the following way:

*function DP = system\_26(fi, P)*

*DP* is a column vector corresponding to pressure first derivative with respect to angular coordinate  $\varphi$ , *fi* represents the angular coordinate  $\varphi$  and *P* is the pressure field to be calculated. Inside the function, the subroutine *system\_coefficients* computes for each integration step the system coefficients used to write the system. To better understand this last statement, a piece of the function is reported in Figures 4.12 and 4.13.

#### **4.2.4 The function *rotor\_dyn\_force.m***

This function uses as input the pressure field calculated inside vane spaces and holes to compute the forces acting on the rotor shaft in *x* and *y* direction. These forces are important in defining the effective eccentricity because they influence the shaft displacement. They can be calculated as depicted in section 3.4.1. On the other side, the forces acting on the rotor are also fundamental in calculating the rotor dynamic equilibrium (see section 3.1).

The code of function *rotor\_dyn\_force.m* is reported as an example in Figures 4.14 and 4.15.

#### **4.2.5 The script *full\_model.m***

This script includes all the calculation useful to obtain the pressure and force fields inside the pump. Starting from a first trial initial condition, it allows to obtain the pressure and force distributions after several iterations. At the end of the calculation, the values of the flow rates between the control volumes are available as well. In general from 4 to 6 iterations are needed. The iteration control is based on three conditions:

- The *SEP* value (see section 3.6) of two consecutive iterations must match under a certain tolerance (*eps\_1* on the MATLAB script);
- The average value of the force on the rotor of two consecutive iterations must match under a certain tolerance (*eps\_2* on the MATLAB script);
- The number of the current iteration is lower with respect to the maximum number of iteration allowed.

Figure 4.16 can be used to better understand the script's structure.

```

function DP=system_26(fi,P);

% computes the system of flow rate balance equations for 13 control volumes

%
%-----
%% Global variables
global look_up flow_rate vol_var;;
%-----

%% load geometry data
data

%% find the angular position
fi_index=find(FI_half<=fi);
fi_index=fi_index(1,end);
fi_discr=FI_half(fi_index); % [deg]

%% Coefficients
[V,DV,C_dv,C_ds,C_f1,C_g1,C_ext_in,C_ext_out,C_int_in,C_d_out,C_d_in,...
 C_int_out,C_t1,C_f2,C_g2,C_t2,C_vg,C_dg,...
 Q_drag,C_duct_in,C_duct_out]=...
 system_coefficients(fi_index);

%% angular regions
% fi_dom=FI_half; %[deg]
% [fi_1,fi_2,fi_3,fi_4,fi_vp,fi_htb]=angular_regions;

%% System

% Distribution volumes definition
V_man_ext=2*V(23);
V_man_int=2*V(25);
V(23)=V_man_ext+3.6184*10^4*10^-9;
V(25)=V_man_int;
V_asp_ext=2*V(24);
V_asp_int=2*V(26);
V(24)=V_asp_ext+2.0987*10^4*10^-9;
V(26)=V_asp_int;

k=look_up.k;
k_out=look_up.k_out;
A_out=2.852*10^-4;
%A_in=look_up.inlet_ext_interface;
A_in=5.0671*10^-4;
P_in=look_up.P_in;
P_out=look_up.P_in;
P_d=look_up.P_d;
ro=look_up.ro;
omega_deg=look_up.omega; %[deg/s]
omega=look_up.omega*pi/180;

P_in_dist=9.9370*10^4;

% System of equations

```

Figure 4.12: The script *system\_26.m* syntax (p. 1).



```

%% Vol 1
DP(1,1)=bulk_modulus(P(1))/(V(1)*omega_deg)*...
    (-DV(1)...
    + (Q_drag(1)...
        +C_dv(1)*(P_d-P(1))...
        +C_ds(1)*(P_d-P(1))...
        +C_g1(1)*(P(12)-P(1))+C_g2(1)*(P(2)-P(1))...
        +C_vg*(P(12)/2-P(1))+C_vg*(P(22)/2-P(1))...
        +C_t1(1)*sqrt(abs(P(2)-P(1)))*sign(P(2)-P(1))...
        +C_t2(1)*sqrt(abs(P(11)-P(1)))*sign(P(11)-P(1))...
        +C_f1(1)*(P(2)-P(1))...
        +C_f2(1)*(P(11)-P(1))...
        +C_ext_in(1)*sqrt(abs(P(24)-P(1)))*sign(P(24)-P(1))...
        +C_ext_out(1)*sqrt(abs(P(23)-P(1)))*sign(P(23)-P(1)));

% flow rate
flow_rate.drag(1,fi_index)=Q_drag(1);
flow_rate.dren_vanes(1,fi_index)=C_dv(1)*(P_d-P(1));
flow_rate.vanes_holes(1,fi_index)=C_g1(1)*(P(12)-P(1))+C_g2(1)*(P(2)-P(1));
flow_rate.holes_region(1,fi_index)=C_vg*(P(12)/2-P(1))+C_vg*(P(22)/2-P(1));
flow_rate.vane_vane(1,fi_index)=C_t1(1)*sqrt(abs(P(2)-P(1)))*sign(P(2)-P(1))...
    +C_t2(1)*sqrt(abs(P(11)-P(1)))*sign(P(11)-P(1));
flow_rate.inlet(1,fi_index)=C_ext_in(1)*sqrt(abs(P(24)-P(1)))*sign(P(24)-P(1));
flow_rate.outlet(1,fi_index)=C_ext_out(1)*sqrt(abs(P(23)-P(1)))*sign(P(23)-P(1));
% rate of volume variation
vol_var(1,fi_index)=-DV(1);

%% Vol 2
DP(2,1)=bulk_modulus(P(2))/(V(2)*omega_deg)*...
    (-DV(2)...
    + (Q_drag(2)...
        +C_dv(2)*(P_d-P(2))...
        +C_ds(2)*(P_d-P(2))...
        +C_g1(2)*(P(12)-P(2))+C_g2(2)*(P(13)-P(2))...
        +C_vg*(P(12)/2-P(2))+C_vg*(P(13)/2-P(2))...
        +C_t1(2)*sqrt(abs(P(3)-P(2)))*sign(P(3)-P(2))...
        +C_t2(2)*sqrt(abs(P(1)-P(2)))*sign(P(1)-P(2))...
        +C_f1(2)*(P(3)-P(2))...
        +C_f2(2)*(P(1)-P(2))...
        +C_ext_out(2)*sqrt(abs(P(23)-P(2)))*sign(P(23)-P(2)));

% flow rate
flow_rate.drag(2,fi_index)=Q_drag(2);
flow_rate.dren_vanes(2,fi_index)=C_dv(2)*(P_d-P(2));
flow_rate.vanes_holes(2,fi_index)=C_g1(2)*(P(12)-P(2))+C_g2(2)*(P(13)-P(2));
flow_rate.holes_region(2,fi_index)=C_vg*(P(12)/2-P(2))+C_vg*(P(13)/2-P(2));
flow_rate.vane_vane(2,fi_index)=C_t1(2)*sqrt(abs(P(3)-P(2)))*sign(P(3)-P(2))...
    +C_t2(2)*sqrt(abs(P(1)-P(2)))*sign(P(1)-P(2));
flow_rate.inlet(2,fi_index)=0;
flow_rate.outlet(2,fi_index)=C_ext_out(2)*sqrt(abs(P(23)-P(2)))*sign(P(23)-P(2));
% rate of volume variation
vol_var(2,fi_index)=-DV(2);

```

Figure 4.13: The script *system\_26.m* syntax (p. 2).

```

function [forza_rotore]=...
    rotor_dyn_force(P_calc_vanes, P_calc_holes, L_matr);

% Computes the force on the rotor shaft
% output: values of forces and directions
% input: pressures, distances between rotor and pressure ring

%% Load geometry data
data;

%% Pressure mtr. construction
st=length(P_calc_vanes)/N;

P_matr_vanes=zeros(N,st);
P_matr_holes=zeros(N,st);

for pitch=1:N
    P_matr_vanes(pitch,:)=P_calc_vanes(1+(pitch-1)*st:pitch*st);
    P_matr_holes(pitch,:)=P_calc_holes(1+(pitch-1)*st:pitch*st);
end

P_matr_vanes_plusone(1:N-1,:)=P_matr_vanes(2:N,:);
P_matr_vanes_plusone(N,:)=P_matr_vanes(1,:);

%% Direction cosines

fi=linspace(0,360,length(P_calc_vanes));
n_x=cosd(fi-90);
n_y=sind(fi-90);

nv_x=cosd(fi+360/(2*N)-90);
nv_y=sind(fi+360/(2*N)-90);

tv_x=-sind(fi+360/(2*N)-90);
tv_y=cosd(fi+360/(2*N)-90);

n_x_matr=zeros(N,st);
n_y_matr=zeros(N,st);

nv_x_matr=zeros(N,st);
nv_y_matr=zeros(N,st);

for pitch=1:N
    n_x_matr(pitch,:)=n_x(1+(pitch-1)*st:pitch*st);
    n_y_matr(pitch,:)=n_y(1+(pitch-1)*st:pitch*st);

    nv_x_matr(pitch,:)=nv_x(1+(pitch-1)*st:pitch*st);
    nv_y_matr(pitch,:)=nv_y(1+(pitch-1)*st:pitch*st);

    tv_x_matr(pitch,:)=tv_x(1+(pitch-1)*st:pitch*st);
    tv_y_matr(pitch,:)=tv_y(1+(pitch-1)*st:pitch*st);
end

%% F_sr
F_sr_matr=-2*mm_2_m*rotor.radius*mm_2_m*rotor.width*sind(360/(2*N)).*...

```

Figure 4.14: The script *rotor\_dyn\_force.m* syntax (p. 1).

```
P_matr_vanes;

% each row represents F_sr,i
F_sr_x_matr=F_sr_matr.*n_x_matr;
F_sr_y_matr=F_sr_matr.*n_y_matr;

%% F_hr
F_hr_matr=mm_2_m*vane.bottom_thickness*mm_2_m*rotor.width.*...
(P_matr_holes-(P_matr_vanes+P_matr_vanes_plusone)/2);

% each row represents F_hr,i
F_hr_x_matr=F_hr_matr.*nv_x_matr;
F_hr_y_matr=F_hr_matr.*nv_y_matr;

%% F_vr
L_matr_vanes(:,:)=L_matr(1:N,1:st);

F_vr_matr=mm_2_m*rotor.width.*(L_matr_vanes-mm_2_m*rotor.radius).*...
(P_matr_vanes-P_matr_vanes_plusone);

% each row represents F_vr,i
F_vr_x_matr=F_vr_matr.*tv_x_matr;
F_vr_y_matr=F_vr_matr.*tv_y_matr;

%% F_fv
[F_vh_x_matr, F_vh_y_matr]=...
vane_head_force(P_calc_vanes, P_calc_holes, L_matr);
F_vh_matr=(F_vh_x_matr.^2+F_vh_y_matr.^2).^0.5;

F_fv_matr=-mu_f.*F_vh_matr;

% each row represents F_vr,i
F_fv_x_matr=F_fv_matr.*tv_x_matr;
F_fv_y_matr=F_fv_matr.*tv_y_matr;

%% F_rotor
F_rotor_x_matr=F_sr_x_matr+F_hr_x_matr+F_vr_x_matr+F_fv_x_matr;
F_rotor_x=sum(F_rotor_x_matr,1);

F_rotor_y_matr=F_sr_y_matr+F_hr_y_matr+F_vr_y_matr+F_fv_y_matr;
F_rotor_y=sum(F_rotor_y_matr,1);

%% OUTPUT
forza_rotore.x=F_rotor_x;
forza_rotore.y=F_rotor_y;
forza_rotore.v_x=sum(F_vh_x_matr,1);
forza_rotore.v_y=sum(F_vh_y_matr,1);
forza_rotore.p_x=sum(F_hr_x_matr,1);
forza_rotore.p_y=sum(F_hr_y_matr,1);
forza_rotore.media_x=sum(forza_rotore.x,2)/length(forza_rotore.x);
forza_rotore.media_y=sum(forza_rotore.y,2)/length(forza_rotore.y);
forza_rotore.media=sqrt(forza_rotore.media_x.^2+forza_rotore.media_y.^2);
forza_rotore.dir=...
atand(forza_rotore.media_y/forza_rotore.media_x)+90;

return
```

Figure 4.15: The script *rotor\_dyn\_force.m* syntax (p. 2).

```

while ITER<=MAX_iter &&...
    max(abs(SEP_it-SEP))>=eps_1 &&...
    max(abs(F_pm_it-F_pm))>=eps_2

SEP=SEP_it;
F_pm=F_pm_it;

% Look up tables
[FI_matr,L_matr,area,V_matr,DV_matr,look_up]=complete_look_up;

[P_calc_vanes,P_calc_holes,flow_rate,flows,dervol]=pressure_field;
P_calc_vanes_matr(ITER,:)=P_calc_vanes;
P_calc_holes_matr(ITER,:)=P_calc_holes;

% Bearing behavior: the true eccentricity
% angle vectors
% LP model
%fi_deg_lp=FI_matr(1,:);
[p_v,p_p]=pressure_shift_lp_to_em(P_calc_vanes,P_calc_holes);

% Force on rotor calculation

% EMPIRICAL model
n_pal=11; % vane number
dati % EMPIRICAL model data
i_ang=i_ang*(360/(2*pi));
fi_deg_em=[0:i_ang:360-i_ang];
fi=fi_deg_em*2*pi/360; %[rad]
N=length(fi);
funz=1; % full flow condition
P_es=240; % [bar]

[Fr_v fi_frv Fr_p fi_frp Fr_tot fi_frtot forza_rotore]=...
    forze_dinamiche_rot(fi,p_v,p_p,funz,n_pal,P_es);
F_pm_it=[forza_rotore.media_x forza_rotore.media_y];

% rename variables
%viscosidad=mou;

% SEP calculation
options=optimset(...
    'Display','iter','TolX',10^-10,'MaxFunEvals',1000,...
    'Maxiter',600,'TolFun',10^-10); % Option to display output

Cr=(Cr_max+Cr_min)/2;
x_0=[-Cr/1000 -Cr/1000];
[SEP_it,fval]=fsolve(@sep_system,x_0,options);
%SEP_it=[-0.05718*10^-3 -0.02424*10^-3];
%SEP_it=[-0.06122*10^-3 -0.01257*10^-3];

IT=num2str(ITER);
['End of iteration ' IT]
% new iteration
ITER=ITER+1;
end

```

Figure 4.16: The *full\_model.m* syntax.

## Chapter 5

# Experimental validation

*In this section the results of experimental measurements in terms of pressure evolutions and case accelerations will be described. The frequency response functions experimental determination procedure will be reported as well, hence the lumped parameter model outputs will be compared to experimental measurements in the frame of a validation process. Finally, each result will be analyzed and discussed.*

### 5.1 Method

In the present chapter the results of the *LP* model will be validated by comparison with experimental data. Since the model simultaneously considers several phenomena involved in the pump working, a wide set of assessments is required. In more detail the method underlined hereafter has been applied.

- The results in terms of pressure evolution in a vane space and in a hole have been compared with pressure evolutions measured in working conditions (see section 5.3.1).
- The flow rates measured in working conditions have been compared with the flow rates calculated by the model (see section 5.3.2).
- The torques measured in working conditions have been compared with the torques calculated by the *LP* model (see section 5.3.3).
- The forces acting on the rotor shaft and on the pressure ring can be calculated using algorithms based on the theory exposed in sections 3.4.1 and 5.2.4. Hence a comparison between forces calculated basing on simulated and experimental pressure fields has been done (see sections 5.3.4 and 5.3.5).
- The pump casing accelerations measured in working conditions have been compared with calculated accelerations. To do this a set of frequency response functions (*FRFs*) has been combined with the forces calculated by means of the *LP* model (see section 5.3.6).

In the next sections a description of the experimental tests will be provided and finally the model assessment procedure will be presented and discussed.

## 5.2 Experimental tests

Several tests have been performed in order to determine the pressure evolution inside the pump, the flow rates in working conditions, the vibration and the frequency response functions of the pump casing. The experimental apparatus and the procedures used during the test campaign will be described in the present section.

### 5.2.1 Pressure evolution measurements

The pressure evolution in working condition has been measured by using the test bench described in section 2.3, Figure 2.18. The pressure field has been investigated both for a vane space and for a hole control volume thanks to an ad hoc designed rotor shaft, depicted in Figures 2.19. The pump used to perform pressure measurements in working conditions shows also some other differences with respect to regular pumps. For example in Figure 5.1 a brass device suitably designed to hold the pressure transducers can be immediately noticed on the pump on the right. Furthermore, the pump cover must be drilled to allow the passage of the modified rotor shaft. Finally the pump modified to carry out the pressure measurements can be mounted on the test bench as depicted in Figure 5.2: two measured chambers are obtained in the brass measuring device thanks to O-ring gaskets and the pressure evolution can be acquired by means of two piezoelectric pressure transducers *Kistler*, model 6207. In this way the pressure evolution for a vane space and for a hole are measured separately during the same run. The acquisitions have been synchronized thanks to a trigger signal provided by a proximity sensor *Balluff BES516324s4c* directly placed on the test bench motor drive shaft. All the working pressure range has been covered, from 20, up to 250 bar. For the sake of brevity, only pressure evolutions at the highest working pressure will be reported since this results better depict several important aspects. Some general observations about pressure evolutions can be finally done. It is possible to notice from Figure 5.3 that the pressure starts to increase when the communication between inlet ducts and a vane space or a hole is interrupted (i.e. at 22.5 deg for the pressure evolution in a vane space). Hence, a peak is clearly visible in the vane space pressure evolution in full flow condition (see Figure 5.3) once the outlet distribution groove, whose geometry has been described in Figure 2.14, is completely passed at about 40 deg; then the pressure evolution starts to decrease at the beginning of the inlet groove (200 deg) to finally reach the inlet pressure value when the inlet duct fully communicates with the vane space or the hole (220 deg for the vane space pressure evolution, 230 deg for the hole pressure evolution). Finally, both in Figure 5.3 and 5.4, the ripple phenomena is clearly noticeable in the high pressure region. These experimental measurements will be used hereafter to validate the *LP* model results in terms of pressure evolution.

### 5.2.2 Flow rate measurements

The main flow rate to be studied and used to assess the model results are the drainage and the outlet flow rate. Both can be measured by a test bench suitably designed (see Figure 2.18). The experimental set-up allows to carry out tests varying the working pressure from 20 up to 250 bar in a loop. The outlet flow

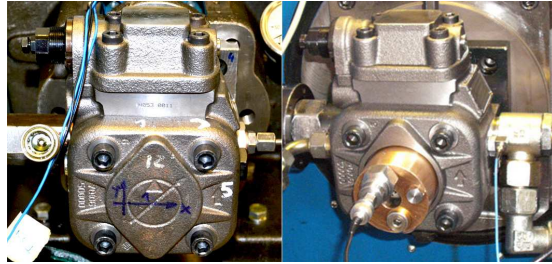


Figure 5.1: The pump *PHV05* on the test bench in normal configuration (on the left) in with the modified cover and measurements devices (on the right).

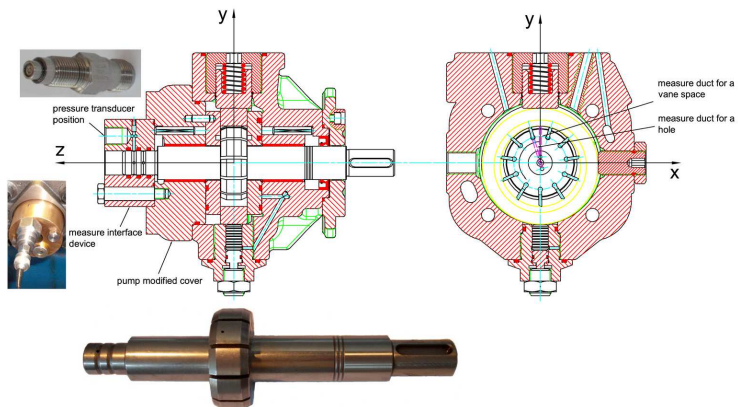


Figure 5.2: The pump *PHV05* modified to perform experimental measurements in working condition.

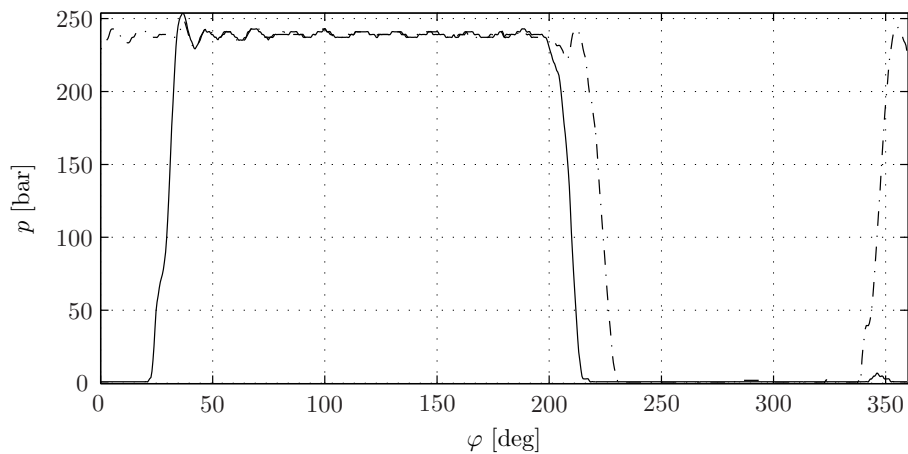


Figure 5.3: Pressure evolution in the full flow condition in a vane space (solid line) and in a hole control volume (dash-dot line).

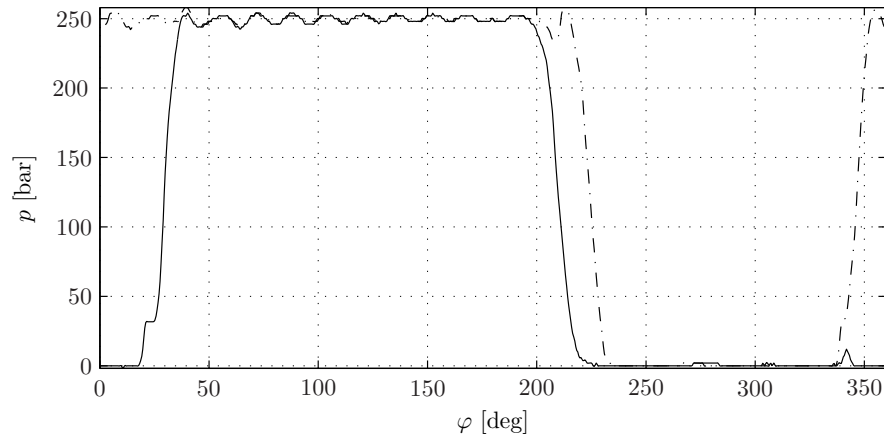


Figure 5.4: Pressure evolution in the zero flow condition in a vane space (solid line) and in a hole control volume (dash-dot line).

rate can be varied by means of a proportional flow rate valve *Vickers Eaton*, model *KBFDG4V* and the flow rate amount can be measured by a flow rate transducer *VSE* model *VS-4GP0-12V*.

In Figure 5.5 the drainage flow rate (blue line) and the outlet flow rate are reported. Analyzing the flow rates trends it is clear that the pump works in the full flow condition from 20 to 240 bar (the cutoff pressure on the characteristic curve in Figure 2.5). Then, the pump reaches its maximum working pressure, the so called dead head pressure, and quickly passes to the zero flow condition. The more the working pressure increases, the more outlet flow rate decreases. On the other side, the drainage flow rate increases: in full flow condition the drainage flow rate is just noticeable, while in zero flow condition it reaches his maximum value.

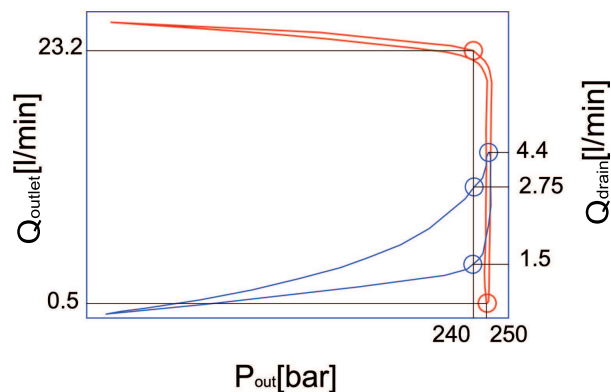


Figure 5.5: The drainage flow rate (blue line) and the outlet flow rate (red line).



### 5.2.3 Torque measurements

Using the torsionmeter inserted in the test bench (a *Staiger Mohilo* model 0160, with a full scale of 500 Nm, see Figure 2.18) it is possible to measure the torque absorbed by the pump during the test described in the previous section. In Figure 5.6 the outlet flow rate trend is reported in blue, while the red line represents the torque measured by the torsionmeter. This plot reveals the main advantage of variable displacement vane pumps with respect to fixed displacement vane pumps. In fact this kind of pumps requires less power in the zero flow condition (the main working condition) allowing to save energy. This fact is capitally important, considering that variable displacement vane pumps usually equip machine tools in which only occasionally the full flow rate regime is required. In section 3.5 this aspect is mathematically demonstrated in equation 3.102. In fact the term  $L_i(\varphi)^2 - r_r^2$  assumes the highest values in the full flow condition because quantity  $L_i(\varphi)$ , representing the distance between the rotor axis and the pressure ring inner race is in direct ratio to the eccentricity between rotor shaft and pressure ring ( $e_{tot}$ ). As depicted in Figure 3.32, the maximum eccentricity values can be reached in the full flow condition and finally it is possible to state that the torque absorbed by the pump in working conditions is in direct ratio with the square of the total eccentricity.

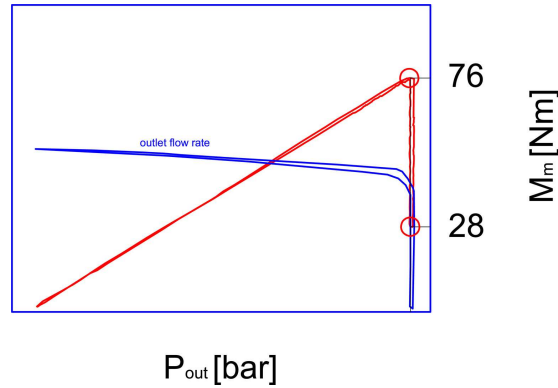


Figure 5.6: Motor torque variation (red line) from the full flow condition to the zero flow condition (see blue line).

### 5.2.4 Pressure force evolution calculation

The pressure force can be calculated once the pressure evolution is measured. It is not possible to directly measure the force on the rotor shaft and on the pressure ring inner race in working condition, nevertheless the forces acting on the rotor shaft can be calculated as suggested in section 3.4.1.

A procedure useful to calculate the pressure forces acting on the pressure ring has been defined as well. The pressure pressure distributions inside the vane spaces and inside the holes are used to determine the force acting on the pressure ring, on a  $xy$  plane. This force, called  $\mathbf{F}_{stator}$ , can be decomposed in two components (see Figure 5.7):

- $F_{stator,x}$  along  $x$  direction, it loads the balancing screw;

- $F_{stator,y}$  along  $y$  direction, it loads the control piston.

Both the components are variable with respect to the angular coordinate  $\varphi$  with period  $\varphi_{vp}$ . In more detail, the pressure force acting on the pressure ring can be obtained by using equation (5.1), in which  $N$  represents the number of vanes. The term  $\mathbf{F}_{rotor}(\varphi)$  in equation (5.1) has been already calculated in section 3.4.1 while terms  $\mathbf{F}_{cv,i}(\varphi)$  and  $\mathbf{F}_{co,i}(\varphi)$  represents the centrifugal forces relative to each vane and to the lubricant trapped in each control volume  $i$  (see Figure 5.8). Terms  $\mathbf{F}_{cv,i}(\varphi)$  and  $\mathbf{F}_{co,i}(\varphi)$  can be expressed as proposed in equations (5.2) and (5.3), where the position of center of mass relative to control volume  $V_i$  has been approximated,  $\rho$  represents the lubricant density,  $\mathbf{n}_i$  and  $\mathbf{n}_{i+N}$  represent the unit vector depicted in Figure 3.24.

$$\mathbf{F}_{stator}(\varphi) = -\mathbf{F}_{rotor}(\varphi) + \sum_{i=1}^N (\mathbf{F}_{cv,i}(\varphi) + \mathbf{F}_{co,i}(\varphi)) \quad (5.1)$$

$$\mathbf{F}_{cv,i}(\varphi) = m_v \omega^2 \left( L_i(\varphi) - \frac{h_v}{2} \right) \mathbf{n}_{i+N} \quad (5.2)$$

$$\mathbf{F}_{co,i}(\varphi) = \rho \omega^2 V_i(\varphi) \frac{L_{i-1}(\varphi) + L_i(\varphi) + 2r_r}{4} \mathbf{n}_i \quad (5.3)$$

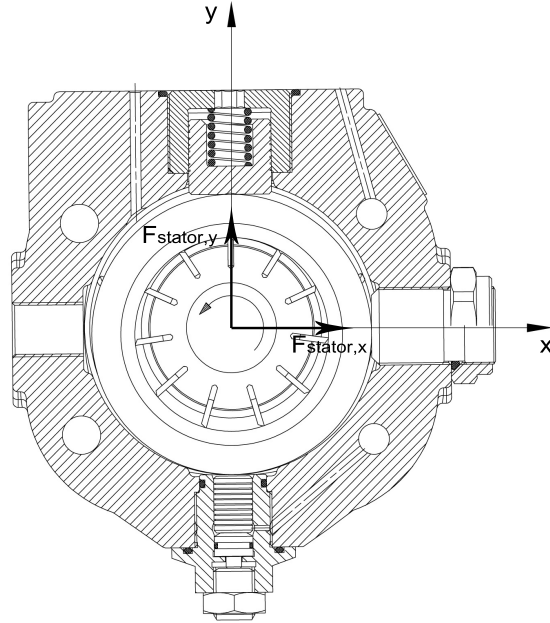


Figure 5.7: Radial pressure forces acting on the pump casing.

The pressure forces study is capitally important not only in properly designing the pressure ring and the rotor shaft, but also in characterizing the pump vibrational behavior. The force on the pressure ring will be used to study the vibrational behavior of the pump body, in fact this variable force loads the body in correspondence of the bias piston and the control piston (see Figure 2.9). The

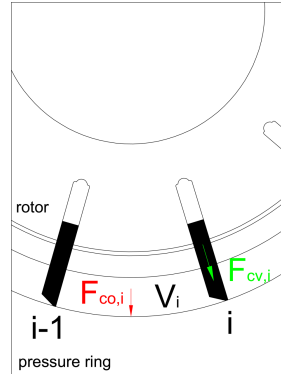


Figure 5.8: Forces acting on the pressure ring due to centrifugal actions relative to lubricant ( $\mathbf{F}_{co,i}$ ) and vane ( $\mathbf{F}_{cv,i}$ ).

force on the rotor shaft concurs in determining the real eccentricity in working condition because of its influences on the shaft displacement (see section 3.3.1). Finally, the resulting action of forces on the rotor shaft concurs in determining the journal bearings reaction force, whose actions load the pump casing in correspondence of the two journal bearings.

The pressure force evolutions acting on the pressure ring and on the rotor shaft can be calculated by means of the procedures described above and in section 3.4.1.

Figures from 5.9 to 5.12 give evidence to the main periodicity who characterize the pump behavior. In fact in each force plot a number of peaks equal to the number of vanes ( $N = 11$ ) can be noticed. Going further, the force component along  $x$  coordinate is always bigger than the force component along the  $y$  coordinate but the amplitude variation of the  $y$  component is bigger with respect to the amplitude variation of the  $x$  component. The forces on rotor shaft have opposite direction with respect to forces on pressure ring, the modulus of forces on pressure ring is slightly bigger compared to the modulus of forces on rotor shaft because the first take into account also the vane contact forces (see section 3.4). Finally, the forces acting on the rotor shaft will be used together with the journal bearings reactions and the experimental frequency response functions to calculate the accelerations of the casing surface. In this light it is important to understand which frequencies are excited by the pressure forces to distinguish the casing acceleration components due to such forces from the components due to other excitation forms. For this reason the force spectrum of Figure 5.13, concerning the total pressure force acting on the pressure ring, is provided as an example. It is possible to notice that such a force mainly excite the frequency components of 275 and 550 Hz, corresponding to 11<sup>th</sup> and 22<sup>th</sup> orders of rotation then, higher frequencies are slightly excited.

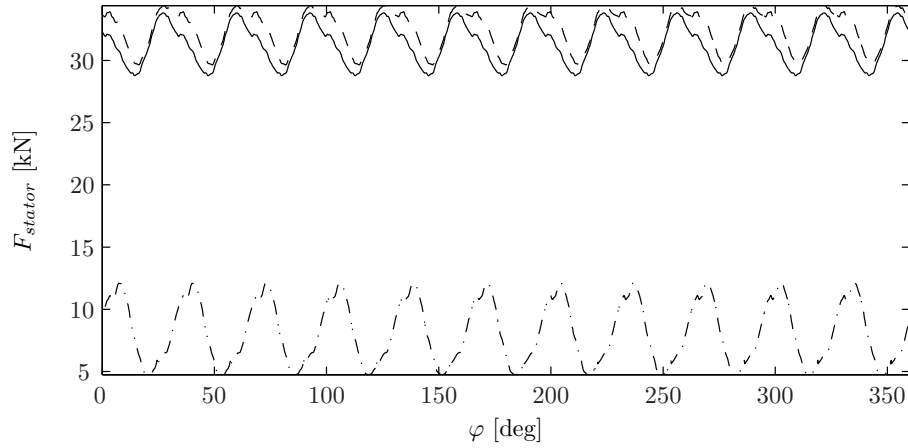


Figure 5.9: Force acting on the pressure ring in the full flow condition:  $x$  component (solid line),  $y$  component (dash-dot line), total force (dashed line).

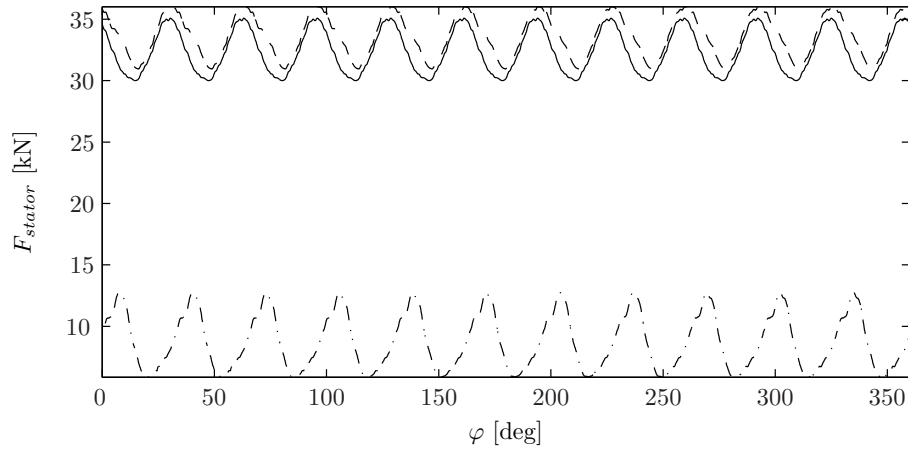


Figure 5.10: Force acting on the pressure ring in the zero flow condition:  $x$  component (solid line),  $y$  component (dash-dot line), total force (dashed line).

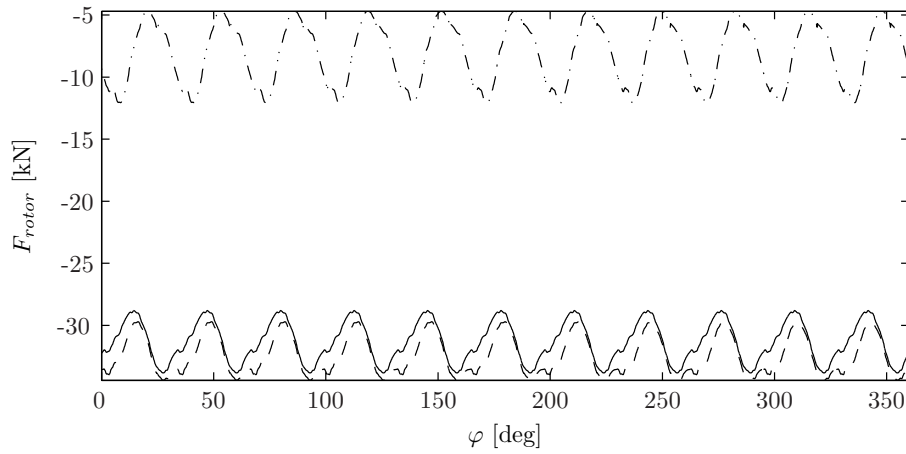


Figure 5.11: Force acting on the rotor in the full flow condition:  $x$  component (solid line),  $y$  component (dash-dot line), total force (dashed line).

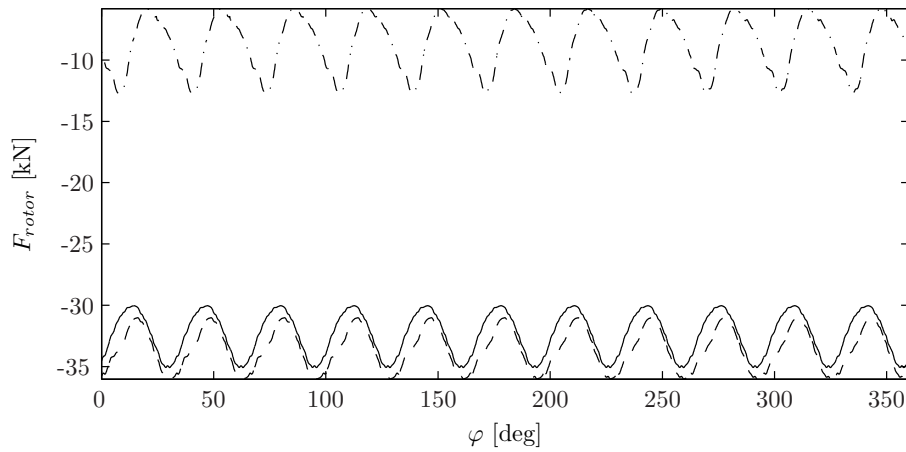


Figure 5.12: Force acting on the rotor in the zero flow condition:  $x$  component (solid line),  $y$  component (dash-dot line), total force (dashed line).

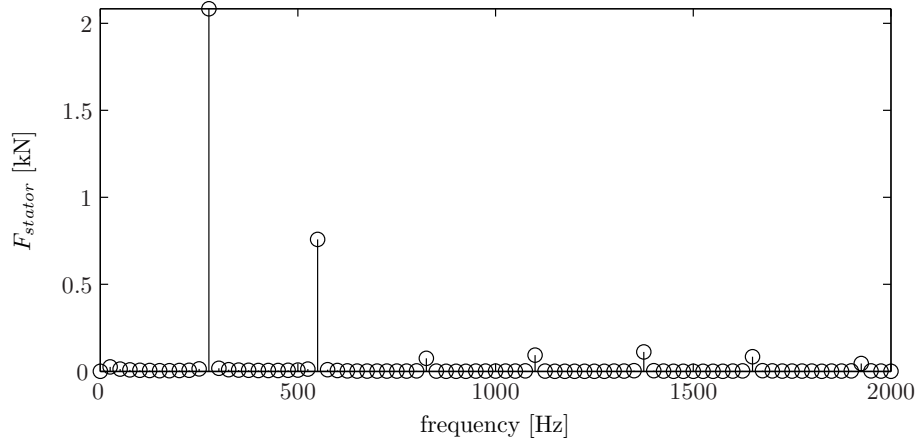


Figure 5.13: Spectrum of the total force acting on the pressure ring in full flow condition.

### 5.2.5 Case frequency response functions

The case frequency response functions have been experimentally determined to evaluate the presence of resonances in the frequency range excited by the time varying pressure forces and they are used as well to calculate the pump casing accelerations using as input data the excitation forces calculated by the models described in the previous chapter. The procedure used in order to compute the frequency response functions (*FRFs*) is the conventional procedure in which both the excitation and response are measured simultaneously to obtain the so called *Inertance*, i.e. the *FRF* between acceleration and force. Five *PCB* piezoelectric accelerometers are mounted inside the pump in order to measure the response in terms of accelerations. These accelerometers are placed in correspondence of the points in which the pump casing is supposed to be excited by time varying pressure forces (see Figure 5.14 and 5.15). Moreover, a *PCB* hammer has been used to excite the pump casing in 5 excitation points, both in  $x$  and  $y$  direction, as depicted in Figures 5.16. The response points (where the accelerometers are mounted, i.e. points  $A$ ,  $B$ ,  $C$ ,  $D$ ) have been maintained fixed during the test, while the excitation moves from one measurement point to another, in order to obtain the *FRF* among all the considered points [40]. The signals were acquired using *SCADAS III SC 305* front-end and *Lms Test.Lab* [41]. A sampling frequency of 25600 Hz was used with a frequency resolution of 0.78 Hz. Furthermore, the *FRFs* are calculated by using the  $H_1$  estimator available in *LMS Test.Lab*. This choice aims at reducing the effects of noise in the output measurements due to ambient random excitations [42].

The frequency range, which is effectively excited by the hammer, is controlled by the stiffness of the contacting surfaces and the mass of the impactor head: it is well known that there is a system resonance at a frequency given by  $(\text{contact stiffness}/\text{impactor mass})^{1/2}$  above which it is difficult to deliver energy into the test structure. Figure 5.17 shows the frequency content of all the hammer blows. It can be noticed that pulses are essentially flat up to 6 kHz, and then the decreased strength makes pulses relatively ineffective at exciting vibrations

in the frequency range above 6 kHz.

*FRF* measurements have been performed with the pump filled with lubricant at the pressure of 20 bar. To do this without perturbing measurements with the noise generated by another pump used to keep in pressure the pump under test, an original procedure has been studied. First of all the pump under test is completely filled with lubricant by using an external pump, then the external pump is disconnected by means of the load valve depicted in Figure 5.16. It is now possible to reach the desired pressure acting on the load piston. To do this, a complete sealing of the pump is obtained thanks to a sealing device directly placed on the rotor shaft hole by which the accelerometers whires can pass outside the pump (see Figure 5.18). Finally, the manometer can be used as a control during all the test operations.

A list of the transducers and instrumentation used during the test campaign is provided in Table 5.1.

Table 5.1: Instrumentation used during the *FRF* measurements.

	Model	Features
2 <i>PCB</i> accelerometers	353B18	Freq. range 1 ÷ 10000 Hz
2 <i>PCB</i> accelerometers	353B15	Freq. range 1 ÷ 10000 Hz
1 <i>PCB</i> Hammer	086D05	

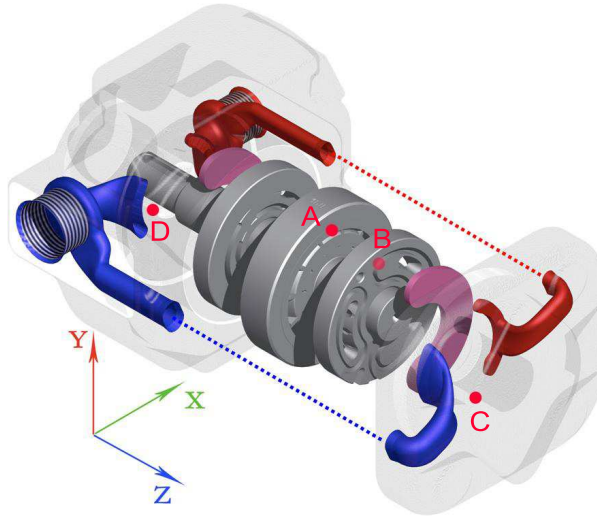


Figure 5.14: Measurement points on the pressure ring, direction  $-y$  (*A*); on the pressure ring, direction  $-x$  (*B*); on the journal bearing cover side (*C*) and on the journal bearing, motor side (*D*).

### 5.2.6 Case vibration measurements

The pump casing accelerations have been measured with the aim at comparing accelerations measured in working conditions with accelerations calculated by means of the product between experimental *FRFs* and forces calculated by

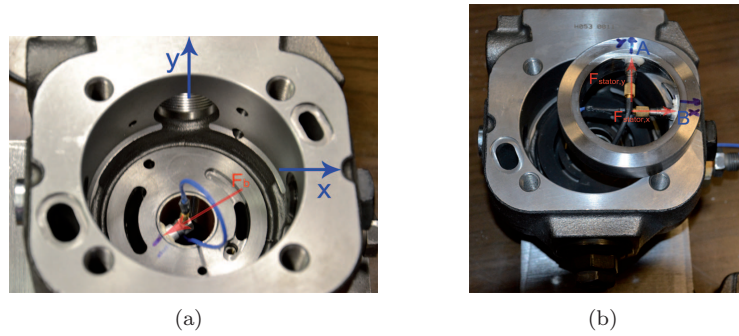


Figure 5.15: Detail of accelerometers mounted on the journal bearing, motor side, point  $D$  (a) on the pressure ring,  $-y$  direction, point  $A$  and  $-x$  direction, point  $B$  (b).

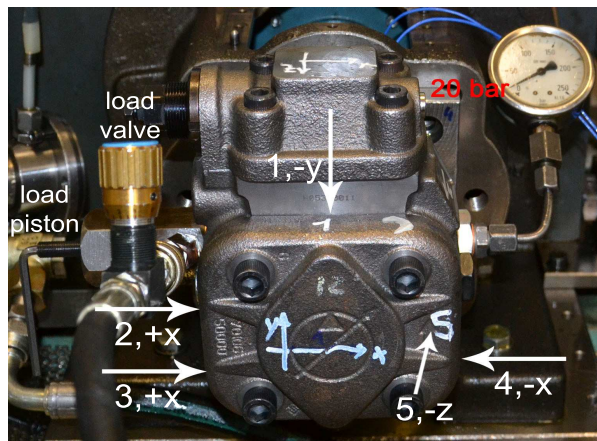


Figure 5.16: Excitation points on the pump casing.

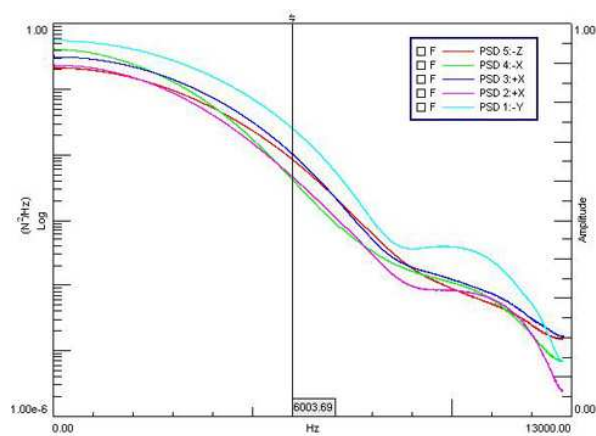


Figure 5.17: Power spectrum density ( $PSD$ ) of all the hammer blows.



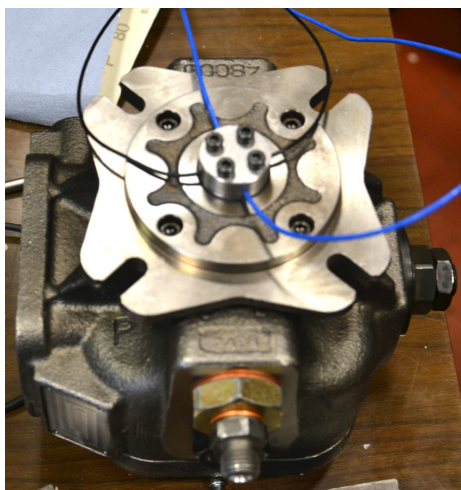


Figure 5.18: The sealing on the rotor shaft hole used to realize the passage of the accelerometers cables.

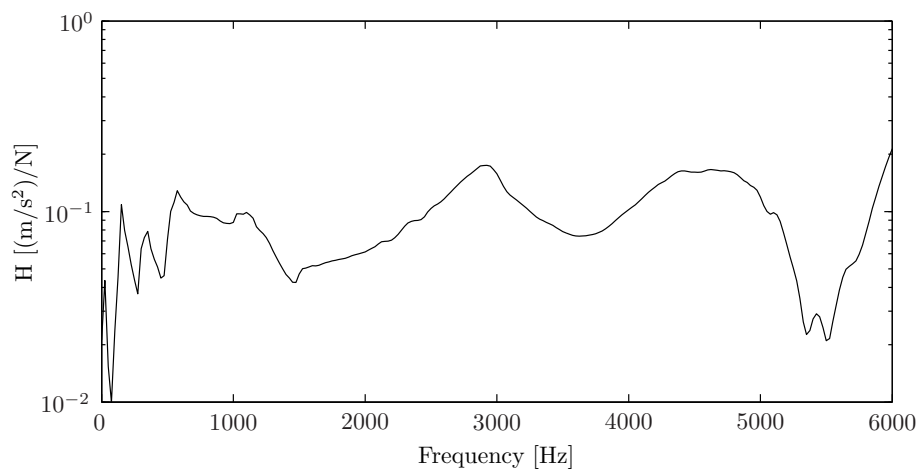


Figure 5.19: Frequency response function obtained exciting the pump casing in point 1 and measuring the acceleration in point A.

the models described in previous sections. For this reason accelerations are measured in the same points used to excite the pump casing by the hammer during *FRFs* measurements (see Figure 5.16). In more detail, accelerations are measured in correspondence of 5 points, as depicted in Figure 5.20, along the directions specified in Table 5.2. In order to observe the vibration signal in one revolution of the rotor shaft, the time domain averaging is combined with the order tracking. Concerning the experimental data, the time domain is resampled in the angular domain in order to obtain the Time Synchronous Average (*TSA*) with respect to a rotor revolution. The angular domain signals are calculated by an off-line interpolation post-processing: a tachometer signal giving 1 pulse/rev is used as a revolution reference. Since the tachometer signals gives only 1 pulse/rev, the *TSA* operation will compensate the changes in the rotor angular velocity variation over a complete revolution but will not compensate variations with a period lower than a complete revolution. In this sense the averaged re-sampled signal is independent of the rotor shaft speed variations.

The acceleration signals have been acquired for 40 s to perform a large number of averages. Finally, the signals have been resampled coherently with the *FRFs* since the experimental casing accelerations have to be compared with the accelerations calculated combining experimental *FRFs* with the pressure forces calculated by the models. The acquisition and resampling parameters as well as the correspondence between the parameters in the time and angular domain are resumed in Table 5.3. Applying the time synchronous average operation, the acceleration signal over a revolution is obtained. As an example the *TSA* of the accelerometer placed in point 3 of Figure 5.20 is depicted in Figure 5.21. Furthermore, the frequency spectrum of the *TSA* is depicted in Figure 5.22. These results are obtained testing the pump at 250 bar, in the full flow condition. Figure 5.21 puts in evidence the main pattern related to pump working: as a matter of fact 11 spikes are clearly noticeable as the pump under test has 11 vanes. One may expect a frequency spectrum with the 11<sup>th</sup> rotation order, equivalent to 275 Hz, characterized by a bigger amplitude with respect to its harmonics. Nevertheless, the main periodicity depicted by the frequency spectrum of Figure 5.22 is related to 550 Hz, equivalent to the 22<sup>th</sup> rotation order.

Table 5.2: Acceleration measurements in working conditions.

	Accelerometer type	Direction
Point 1	<i>PCB</i> model 5353B21	direction $+y$
Point 2	<i>PCB</i> model 353B15	direction $-x$
Point 3	<i>PCB</i> model 353B18	direction $-x$
Point 4	<i>PCB</i> model 353B18	direction $+x$
Point 5	<i>PCB</i> model 353B15	direction $+x$

Table 5.3: Order tracking parameters.

Fixed time sampling frequency	51200 Hz
Rotational velocity	1500 rpm
Order tracking sampling frequency	26600 Hz
Points per revolution	1024 points
Angular resolution	0.3516 deg
Order resolution	1 order
Frequency resolution	25 Hz
Number of averages	700

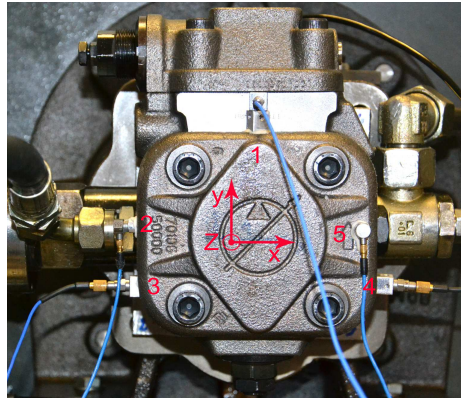


Figure 5.20: The accelerometers placed on the pump casing.

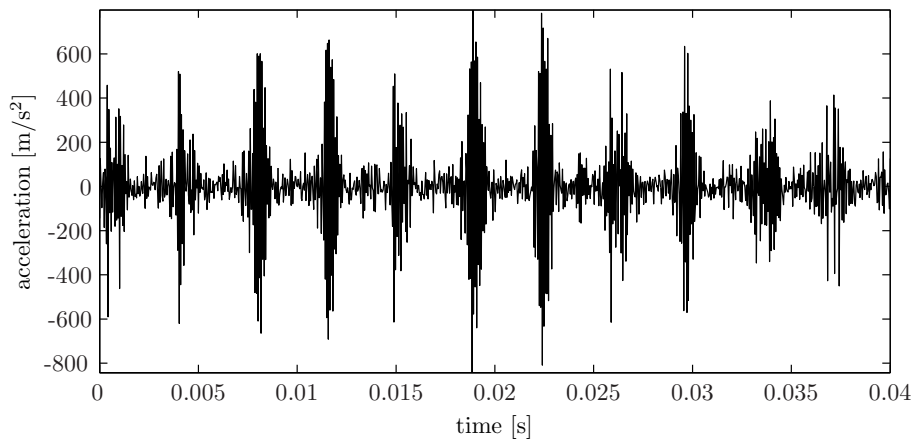


Figure 5.21: Time synchronous average of the acceleration signal acquired in correspondence of point 3 (see Figure 5.20).

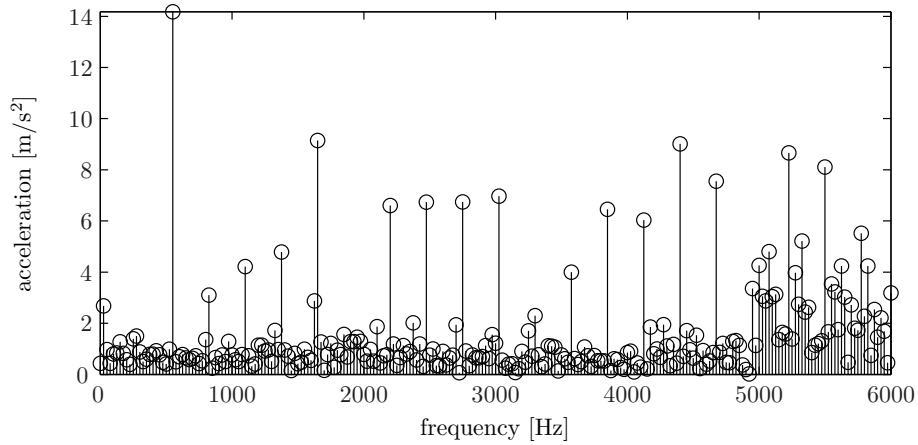


Figure 5.22: Frequency spectrum of the time synchronous average signal depicted in Figure 5.21.

## 5.3 Comparing numerical and experimental results

### 5.3.1 Pressure evolutions

The pressure evolution calculated by the *LP* model has been validated by comparison with the pressure evolution measured in working conditions (see section 5.2.1, Figures 5.9, 5.10, 5.11, 5.12).

Figures 5.23, 5.24, 5.25, 5.26 depict the comparison between measured pressures and *LP* model results in terms of pressure evolution for a complete shaft rotation in a vane control volume and in a hole control volume, in the full flow condition and in the zero flow condition as well. Quantity  $p^*$  represents the normalized pressure (see equation (5.4),  $p_{out}$  is the constant working pressure in the outlet chamber).

$$p^* = \frac{p}{p_{out}} \quad (5.4)$$

The pressure evolution are compared and validated with respect to measured data by using *Percentage of Good points* index (*PGP*) [43]. Such an index assumes higher values when the curves tend to coincide. In practice, a tolerance range  $\delta$  has to be defined a priori (in this case  $\delta$  is equal to 3%). Consequently, when a good resemblance between the measured and simulated data is obtained, a large part of the points of the latter will lie inside the tolerance area and the *PGP* will assume values tending to 100%. Table 5.4 resumes the *PGP* for the pressure evolution in a vane space and in a hole, for the full flow and zero flow condition. The simulated pressure shows a good concordance with the measured pressure and the *PGP* index gives evidence to this fact. Figures from 5.23 to 5.26 show that the simulated pressure evolutions capture the ripple phenomena. However a few mismatches between the experimental and the simulated quantities can be noticed, as the peak amplitude in a vane space at the beginning of

Table 5.4: PGP values for the pressure evolutions in a vane space and in a hole control volume, for the full flow and zero flow condition ( $\delta = 3\%$ ).

Full flow, vane space control volume	71%
Full flow, hole control volume	74%
Zero flow, vane space control volume	71%
Zero flow, hole control volume	75%

the high pressure zone in full flow condition and the instant when the pressure increases and decreases.

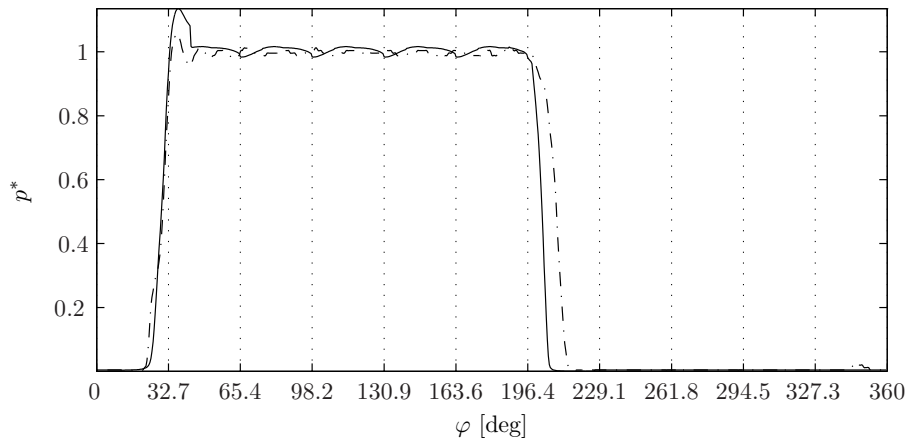


Figure 5.23: Comparison between pressure measured in working conditions (dash-dot line) and pressure calculated by the lumped parameter model (solid line) in the full flow condition for a vane space.

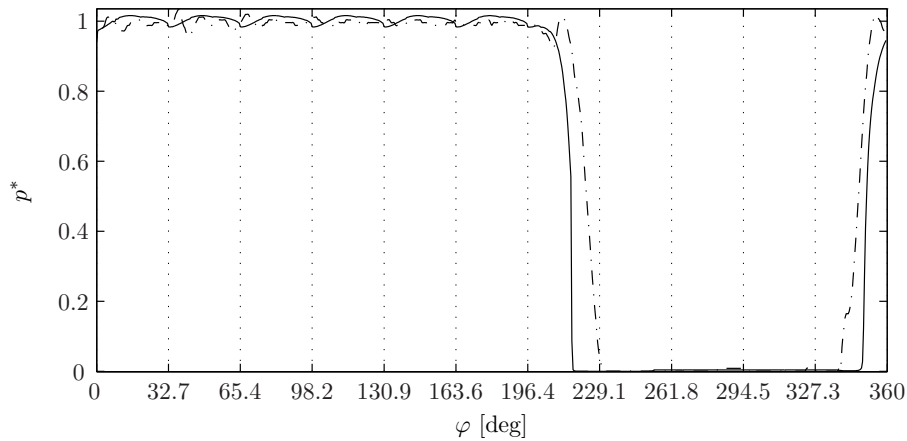


Figure 5.24: Comparison between pressure measured in working conditions (dash-dot line) and pressure calculated by the lumped parameter model (solid line) in the full flow condition for a hole control volume.

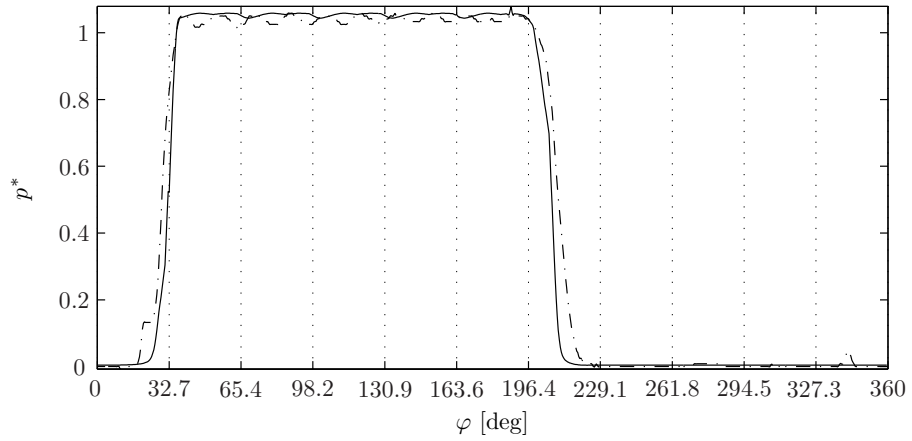


Figure 5.25: Comparison between pressure measured in working conditions (dash-dot line) and pressure calculated by the lumped parameter model (solid line) in the zero flow condition for a vane space.

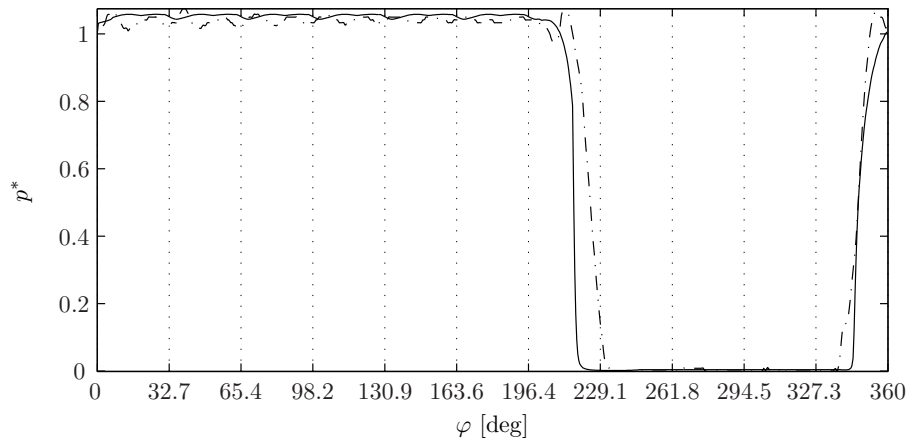


Figure 5.26: Comparison between pressure measured in working conditions (dash-dot line) and pressure calculated by the lumped parameter model (solid line) in the zero flow condition for a hole control volume.

### 5.3.2 Flow rates

During the integration of the flow rate continuity equation system, all the flow rates inside the pump can be calculated. The most interesting study can be done on the outlet and drainage flow rates. In particular, the flow rate calculated by the lumped parameter model can be compared with the flow rate directly measured on the test bench (see Figure 5.5). Table 5.5 resumes the flow rate measured in working condition. It has to be noticed that experimental tests showed great variations in terms of outlet and drainage flow rate depending on the tested pump. In fact these two features are widely influenced by the clearances inside the pump and even small variations in the geometric tolerances can involve great variations in drainage and outlet flow rates. For this reason Figure 5.5 and Table 5.5 resume the mean features in terms of pressures and flow rates obtained during the test campaign.

Table 5.5: Drainage and outlet flow rate values.

Flow rate	Pressure [bar]	Working condition	Value [l/min]
Outlet flow rate	240	Full flow	23.2
Drainage flow rate	240	Full flow	1.5 ÷ 2.75
Outlet flow rate	250	Zero flow	0.5
Drainage flow rate	250	Zero flow	4.4

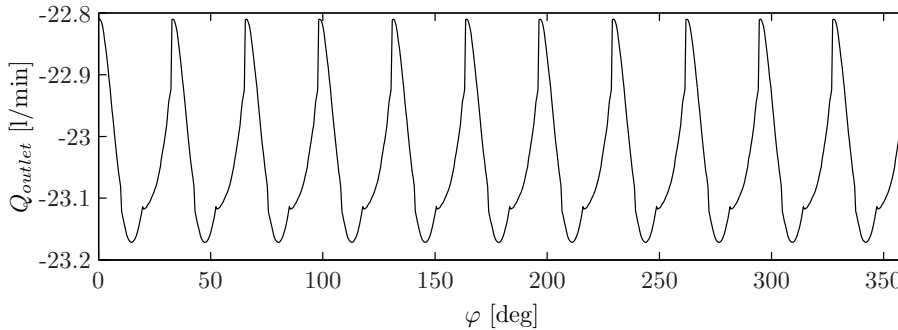


Figure 5.27: Outlet flow rate evolution in the full flow condition.

Figures 5.27, 5.28, 5.29, 5.30 resume the *LP* model results in term of flow rate and allows to appreciate the ripple phenomena once again. It can be noticed that the outlet flow rate in full flow condition computed by the *LP* model (see Figure 5.27) gives a correct estimation of the experimental value listed in Table 5.5. Same considerations can be done for the outlet flow rate in zero flow condition depicted in Figure 5.29. From the point of view of drainage flow rates, it can be noticed that the model overestimates the drainage flow rate in full flow condition (see Figure 5.28), while underestimate the drainage flow rate in zero flow condition. Finally, the calculated flow rates are negative because of the convention used in developing the model that gives negative values to flow rates coming out from the pump.

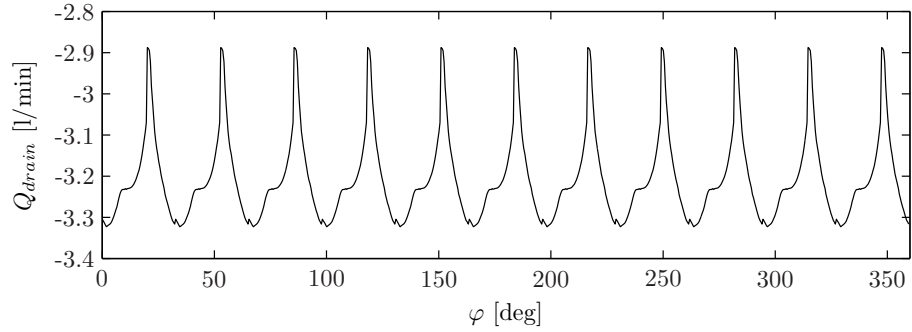


Figure 5.28: Drainage flow rate evolution in the full flow condition.

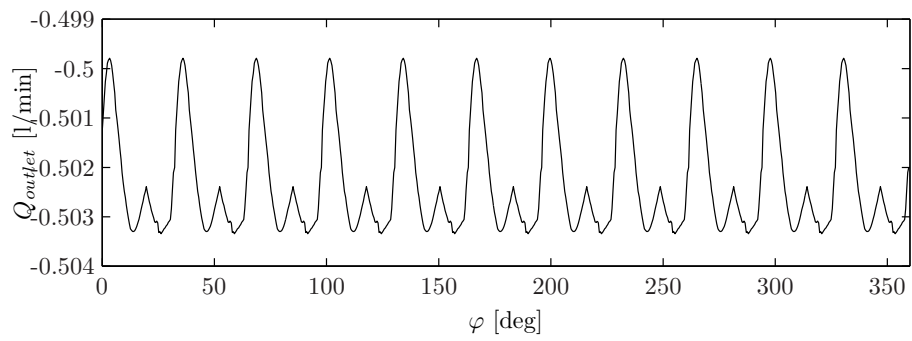


Figure 5.29: Outlet flow rate evolution in the zero flow condition.

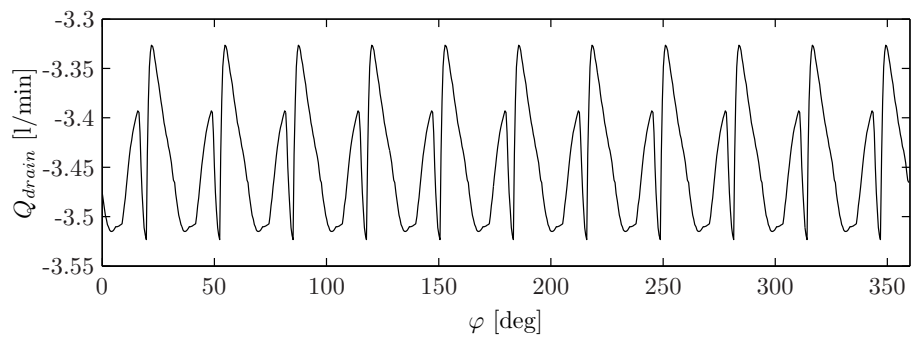


Figure 5.30: Drainage flow rate evolution in the zero flow condition.



### 5.3.3 Motor drive torque

Figure 5.6 in section 5.2.3 depicts the motor drive torque variation with respect to flow rate variation. Table 5.6 resumes the torque values in full flow and zero flow condition. Comparing values of Table 5.6 with the torque trends depicted in Figures 5.31 and 5.32 it is possible to notice a good resemblance. In fact the mean value of calculated motor drive torque in full flow condition is 76.5 Nm, while calculated motor drive torque in zero flow condition is 21.5 Nm. Finally, as it can be seen, the model slightly underestimates the motor drive torque in zero flow condition, nevertheless it must be considered that the torsionmeter full scale is 500 Nm, so the small values to be measured are probably affected by observational errors.

Table 5.6: Motor drive torque in full flow and zero flow condition.

Working condition	Pressure [bar]	Torque value [Nm]
Full flow	240	76
Zero flow	250	28

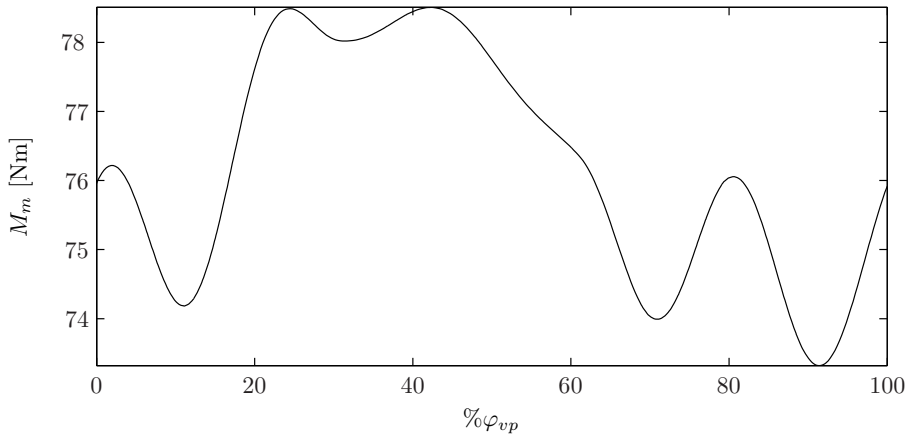


Figure 5.31: The motor drive torque evolution on a vane pitch in the full flow condition.

### 5.3.4 Forces on the pressure ring

As stated before, the study of forces acting inside the pump is capitally important in defining the pump vibrational behavior. In more detail, forces acting on the pressure ring  $F_{stator,x}$  and  $F_{stator,y}$  can be used as input data to calculate accelerations of the case surface by using the experimental frequency response functions (*FRFs*) described in section 5.2.5. In this sight forces calculation and validation is an important step in a proper optimization from a vibrational point of view.

Since the forces evolution is periodic, the comparison between the forces acting in working conditions and the forces calculated by the *LP* model will be done only from  $\varphi = 0$  to  $\varphi = \varphi_{vp}$ .

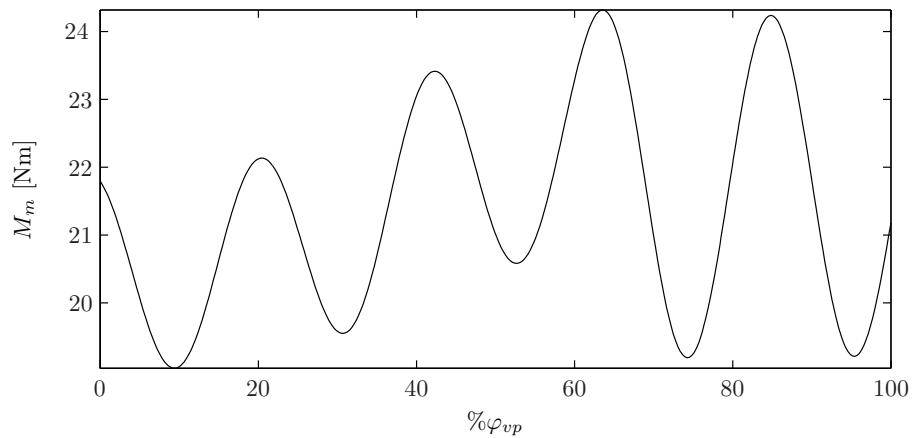


Figure 5.32: The motor drive torque evolution on a vane pitch in the zero flow condition.

Some general observations about forces acting on pressure ring have been already done in section 5.2.4. In the present section the force evolutions calculated from measured data are compared with force evolutions calculated from pressures obtained by the *LP* model.

The comparison between Figures 5.33 and 5.35 with Figures 5.34 and 5.36 shows that, nevertheless the force in  $y$  direction has lower mean value than in  $x$  direction, the most relevant variation is related to  $y$  direction. In particular, in the full flow condition, the *LP* model force exhibits a sudden variation of 8 kN (12 in the zero flow condition) at about 12 deg, while the corresponding sudden variation in  $x$  direction is about 4 kN, both in full flow and in zero flow condition. This is important in the sight of a noise and vibration optimization, since dynamic effects are mainly related to the amount and rate of force variation. It is finally possible to identify the events related to such sudden variations in Figures 5.33, 5.34, 5.35 and 5.36. In Figures from 5.23 to 5.26 the pressure evolution for holes and vane spaces, both in full flow and zero flow condition, are depicted: the  $x$  axis has been divided into 11 parts, each one corresponding to a vane pitch. It is possible to notice that a strong variation in the pressure field occurs for vane spaces in the first part of the 7<sup>th</sup> vane pitch (see the angular interval from 196.4 to 229.1 deg). Furthermore, pressure evolution simulated by the *LP* model shows more sudden changes with respect to the one calculated from experimental pressure evolutions, especially around 12 deg, corresponding to the angular region previously identified. At this angular coordinate the vane space control volume  $V_7$  and the hole control volume  $V_{19}$  start to communicate at the same time with inlet control volumes  $V_{24}$  and  $V_{26}$  (see Figure 5.37). This fact involves the pressure drops depicted in Figures from 5.23 to 5.26, in correspondence of the 7<sup>th</sup> vane pitch and finally the force sudden variation discussed above.

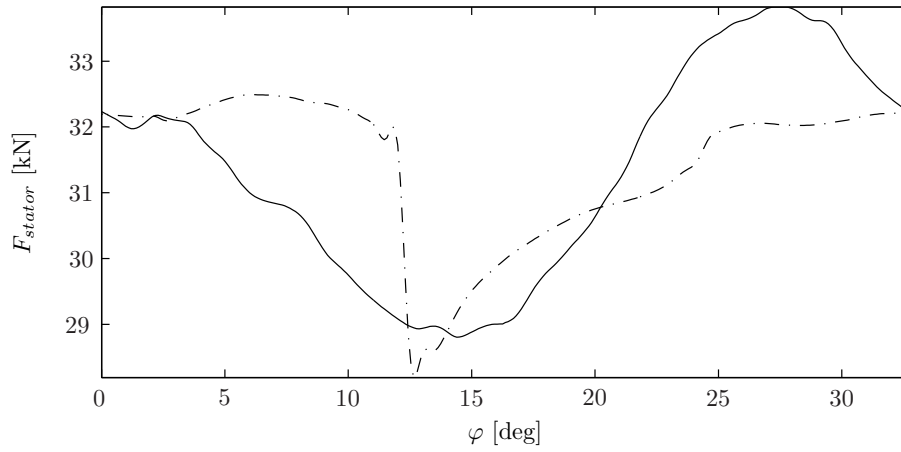


Figure 5.33: Comparison between the forces acting on the pressure ring in working condition (solid line) and the forces calculated by the *LP* model (dash-dot line) in full flow condition, *x* direction.

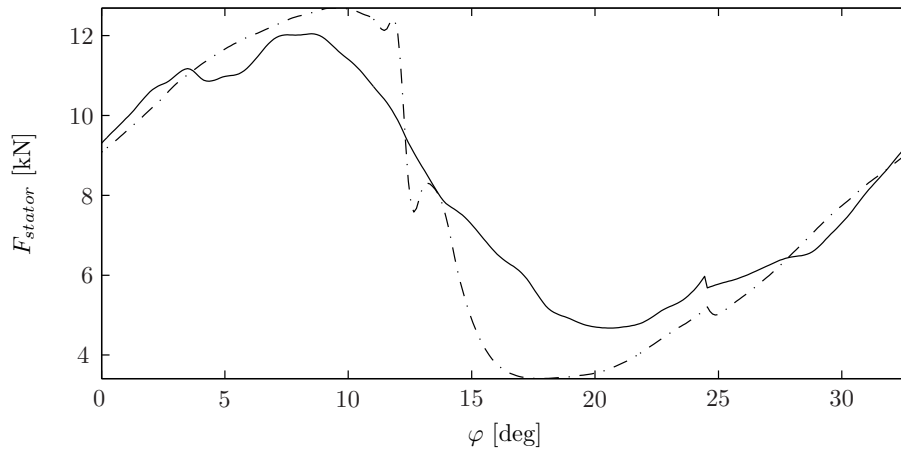


Figure 5.34: Comparison between the forces acting on the pressure ring in working condition (solid line) and the forces calculated by the *LP* model (dash-dot line) in full flow condition, *y* direction.

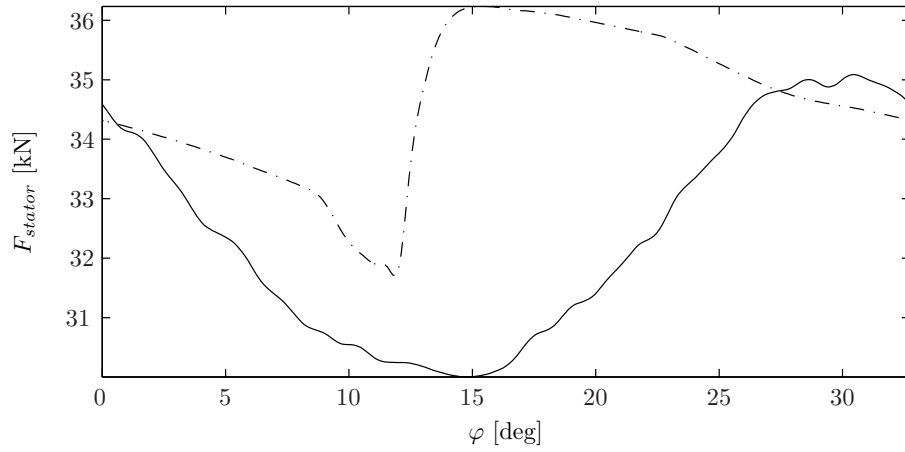


Figure 5.35: Comparison between the forces acting on the pressure ring in working condition (solid line) and the forces calculated by the *LP* model (dash-dot line) in zero flow condition, *x* direction.

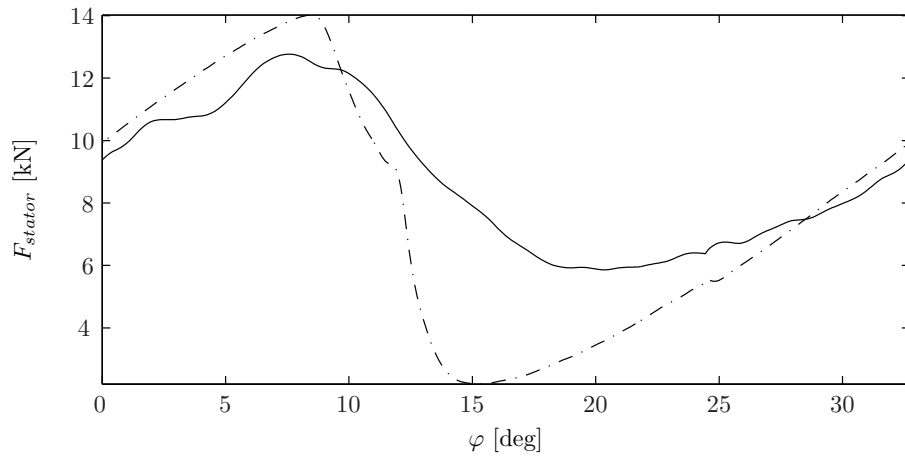


Figure 5.36: Comparison between the forces acting on the pressure ring in working condition (solid line) and the forces calculated by the *LP* model (dash-dot line) in zero flow condition, *y* direction.

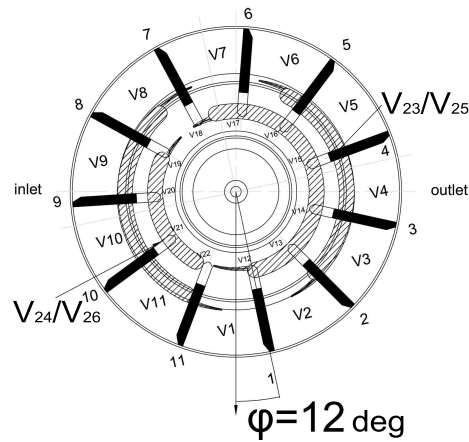


Figure 5.37: Position corresponding to 12 deg after the initial position.

### 5.3.5 Forces on the rotor shaft

As stated before, the study of forces acting inside the pump is capitially important in defining the pump vibrational behavior. In more detail, forces acting on the rotor shaft cause bearing reactions  $F_{b,x}$  and  $F_{b,y}$  who load the pump casing. These components can be used as input data to calculate accelerations of the case surface by using the experimental frequency response functions (*FRFs*) described in section 5.2.5. In this sight forces calculation and validation is an important step in a proper optimization from a vibrational point of view.

Since the forces evolution is periodic, the comparison between the forces acting in working condition and the forces calculated by the *LP* model will be done only from  $\varphi = 0$  to  $\varphi = \varphi_{vp}$ .

Some general observations about forces acting on rotor shaft have been already done in section 3.4.1. In the present section the force evolutions calculated from measured data are compared with force evolutions calculated from pressures obtained by the *LP* model. First of all it has to be noticed that forces acting on rotor shaft have opposite direction with respect to forces acting on pressure ring as a consequence of the absolute reference frame used during calculations (see Figure 2.8). With respect to forces acting on the pressure ring, force acting on rotor shaft do not take into account the vane contact force component since the vanes can slide inside the rotor. As stated before, the main force variation is related to  $y$  component, while the bigger force amount is related to  $x$  component. In general a good resemblance can be noticed between forces along the  $y$  coordinate, both in full low and in zero flow condition. On the contrary, the calculated forces along  $x$  coordinate lay on the same range of forces obtained by measured pressures, their minimum values is in correspondense of the minimum values of forces obtained by measured pressures, but their trend did not follow the trend of experimental forces. This is a consequence of the differences between calculated pressures and experimental pressure described in section 5.3.1.

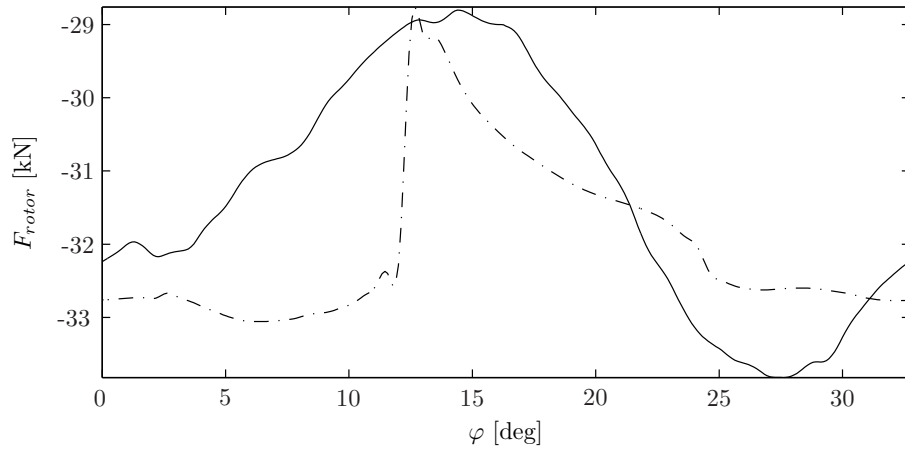


Figure 5.38: Comparison between the forces acting on the rotor shaft in working condition (solid line) and the forces calculated by the *LP* model (dash-dot line) in full flow condition, *x* direction.

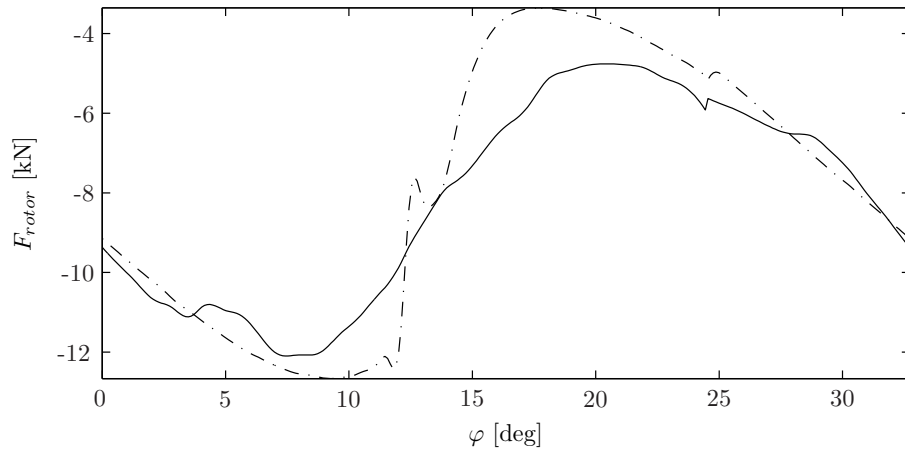


Figure 5.39: Comparison between the forces acting on the rotor shaft in working condition (solid line) and the forces calculated by the *LP* model (dash-dot line) in full flow condition, *y* direction.

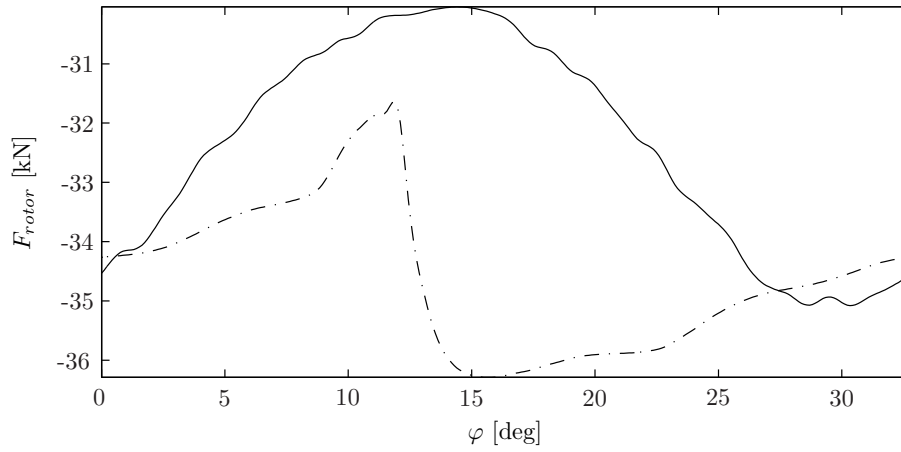


Figure 5.40: Comparison between the forces acting on the rotor shaft in working condition (solid line) and the forces calculated by the *LP* model (dash-dot line) in zero flow condition,  $x$  direction.

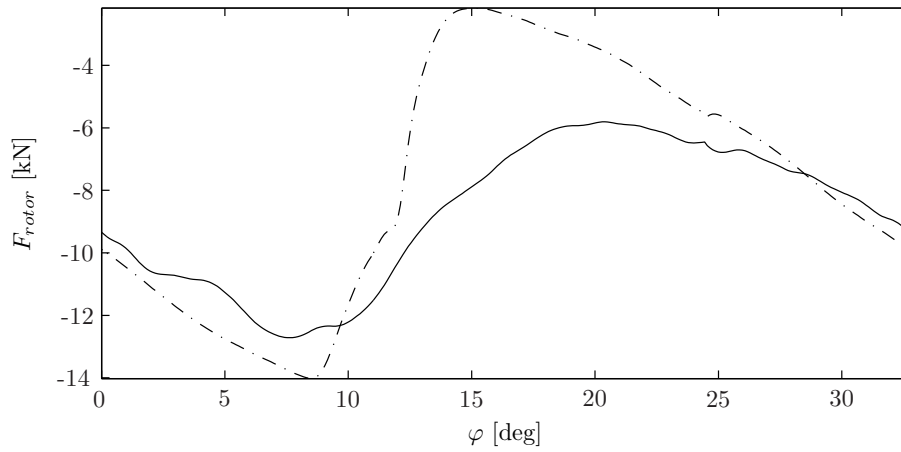


Figure 5.41: Comparison between the forces acting on the rotor shaft in working condition (solid line) and the forces calculated by the *LP* model (dash-dot line) in zero flow condition,  $y$  direction.

### 5.3.6 Pump casing accelerations

In this section the experimental accelerations measured during the test campaign on the pump casing surface, in correspondence of points 1, 2, 3, 4 depicted in Figure 5.20, will be compared with the accelerations calculated by means of the combination of model results and experimental *FRFs*. With reference to Figures 5.14 and 5.16, the following *FRFs* will be used to calculate the pump casing accelerations:

- $H_{A-y,1-y}$ : *FRF* with input in point 1, direction  $-y$  and output in point  $A$ , direction  $-y$ ;
- $H_{B-x,1-y}$ : *FRF* with input in point 1, direction  $-y$  and output in point  $B$ , direction  $-x$ ;
- $H_{C,1-y}$ : *FRF* with input in point 1, direction  $-y$  and output in point  $C$  in the direction of the journal bearing reaction force;
- $H_{D,1-y}$ : *FRF* with input in point 1, direction  $-y$  and output in point  $D$  in the direction of the journal bearing reaction force;
- $H_{A-y,2+x}$ : *FRF* with input in point 2, direction  $+x$  and output in point  $A$ , direction  $-y$ ;
- $H_{B-x,2+x}$ : *FRF* with input in point 2, direction  $+x$  and output in point  $B$ , direction  $-x$ ;
- $H_{C,2+x}$ : *FRF* with input in point 2, direction  $+x$  and output in point  $C$  in the direction of the journal bearing reaction force;
- $H_{D,2+x}$ : *FRF* with input in point 2, direction  $+x$  and output in point  $D$  in the direction of the journal bearing reaction force;
- $H_{A-y,3+x}$ : *FRF* with input in point 3, direction  $+x$  and output in point  $A$ , direction  $-y$ ;
- $H_{B-x,3+x}$ : *FRF* with input in point 3, direction  $+x$  and output in point  $B$ , direction  $-x$ ;
- $H_{C,3+x}$ : *FRF* with input in point 3, direction  $+x$  and output in point  $C$  in the direction of the journal bearing reaction force;
- $H_{D,3+x}$ : *FRF* with input in point 3, direction  $+x$  and output in point  $D$  in the direction of the journal bearing reaction force;
- $H_{A-y,4-x}$ : *FRF* with input in point 4, direction  $-x$  and output in point  $A$ , direction  $-y$ ;
- $H_{B-x,4-x}$ : *FRF* with input in point 4, direction  $-x$  and output in point  $B$ , direction  $-x$ ;
- $H_{C,4-x}$ : *FRF* with input in point 4, direction  $-x$  and output in point  $C$  in the direction of the journal bearing reaction force;
- $H_{D,4-x}$ : *FRF* with input in point 4, direction  $-x$  and output in point  $D$  in the direction of the journal bearing reaction force;



Then, each *FRF* will be multiplied by the dynamic forces calculated by means of the *LP* model to obtain case accelerations. The dynamic forces that will be multiplied with the above mentioned *FRFs* are the forces exciting the pump casing and they consist in the bearing reactions in correspondence of points *C* and *D* of Figure 5.14 and in the components of the force acting on the pressure ring  $F_{stator,y}$  and  $F_{stator,x}$ , in correspondence of points *A* and *B*. In order to obtain the casing accelerations as a function of frequency, the following equations have been used.

$$a_{1,y} = H_{A-y,1-y}F_{stator,y} + H_{B-x,1-y}F_{stator,x} + H_{C,1-y}F_b + H_{D,1-y}F_b \quad (5.5)$$

$$a_{2,-x} = H_{A-y,2+x}F_{stator,y} + H_{B-x,2+x}F_{stator,x} + H_{C,2+x}F_b + H_{D,2+x}F_b \quad (5.6)$$

$$a_{3,-x} = H_{A-y,3+x}F_{stator,y} + H_{B-x,3+x}F_{stator,x} + H_{C,3+x}F_b + H_{D,3+x}F_b \quad (5.7)$$

$$a_{4,+x} = H_{A-y,4-x}F_{stator,y} + H_{B-x,4-x}F_{stator,x} + H_{C,4-x}F_b + H_{D,4-x}F_b \quad (5.8)$$

In the equations above,  $F_{stator,x}$ ,  $F_{stator,y}$  and  $F_b$  represents respectively the spectra of forces action on the pressure ring along *x* direction, along *y* direction and in correspondence of journal bearings.

Since the reactions  $F_{b,x}$  and  $F_{b,y}$ , calculated by the *LP* model as suggested in equation system (3.2) take into account the contributions of both the journal bearings, the total reaction acting on each journal bearing has to be calculated as stated in equation (5.9). This equation is based on the assumption of the symmetry condition of constraints generated by the journal bearing located on the pump cover and the journal bearing located in the pump casing.

$$F_b = \sqrt{F_{b,x}^2 + F_{b,y}^2} \quad (5.9)$$

The comparison between experimental and calculated accelerations have been done up to 2000 Hz. The main reason of this choice can be find in Figure 5.13, in fact the pressure forces calculated by the *LP* model excite the frequencies corresponding to the 11<sup>th</sup> order of rotation and its harmonics, up to 2000 Hz. At higher frequencies, the comparison between calculated and measured acceleration does not make sense because experimental accelerations are influenced by other phenomena involved in pump working but not taken into account by the *LP* model, such as lubricant turbulences and impulsive impacts. Furthermore, the experimental accelerations measured in correspondence of points 1 in *+y* direction and in point 2 in *-y* direction are affected by a big amount of noise. This fact is due to the position of point 1 and 2, that are placed on the pump cover. Such a component is fixed to the pump casing by means of 4 screws and for this reason a big noise amount can be found in the relative accelerometers (see black square markers in Figures 5.42 and 5.43, points 1 and 2). The presence of noise makes difficult to compare the calculated accelerations with experimental data. Considering points 3 and 4, a good resemblance between measured and

calculated accelerations is obtained, with the exception of values relative to the frequency of 275 Hz. In fact the calculated accelerations usually overestimates the amplitude of this component. The main reasons of this difference are the following:

- The *LP* model does not take into account damping phenomena related to the presence of lubricant at high pressure inside the pump.
- The model does not consider the fluid inertia effects inside control volumes.
- The experimental *FRFs* have been measured using a suitably modified pump in which the rotor shaft has been removed. Then the pump has been filled with lubricant at the pressure of 20 bar. In this configuration the inertial properties of the pump used for tests can be quite different with the respect to regular pumps properties. Nevertheless, this method is the only suitable to measure *FRFs* between the casing surface and the excitation points inside the pump.
- The presence of the control piston (see Figure 2.9) has been modeled as a rigid contact. As a matter of fact the control piston is moved by the lubricant action and so the relative damping phenomena are ignored by the *LP* model.
- Only the direct paths connecting points *A*, *B*, *C*, *D* with measurement points 1, 2, 3, 4 have been taken into account.

Using the acceleration spectra depicted in Figures 5.42 and 5.43 it is possible to reconstruct the signal in the time domain. Figures 5.44(a) and 5.44(b) depicts the comparison between the calculated accelerations (red line) and the measured accelerations (black line), for the point 3, respectively in the full flow and zero flow condition. The calculated accelerations and the measured accelerations are compared by using the *Root Mean Square* statistical parameter (*RMS*) [44]. A low percent error is obtained, both for the full flow condition and the zero flow condition (see Table 5.7). In general, the main periodicities and amplitudes are matched, and a correspondence can be found between the peak positions of the calculated accelerations and the experimental data. In this sense the results of the *LP* model in terms of variable forces can be considered globally validated, under the clarifications listed above.

Table 5.7: Comparison between the *RMS* statistical parameter applied to measured and calculated accelerations signals.

Working condition	<i>RMS</i> of experimental acceleration	<i>RMS</i> of calculated acceleration	% Error
Full flow	190.1 m/s <sup>2</sup>	204.8 m/s <sup>2</sup>	7.8%
Zero flow	92.1 m/s <sup>2</sup>	100.9 m/s <sup>2</sup>	9.6%

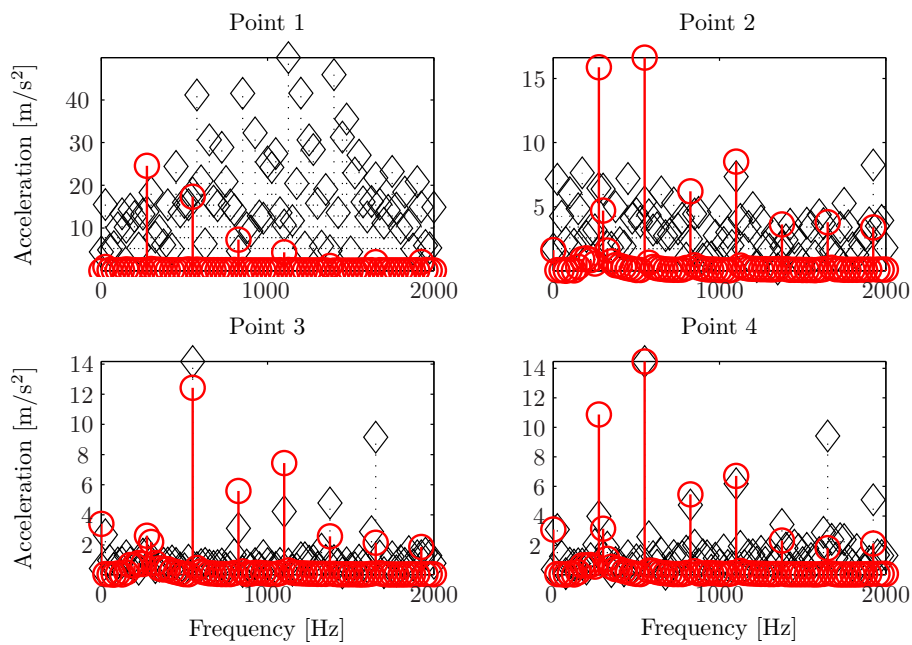


Figure 5.42: Pump casing accelerations in correspondence of points 1, 2, 3, 4 of Figure 5.20, full flow condition. The black square markers represent experimental accelerations, while the red circular markers represent the calculated accelerations.

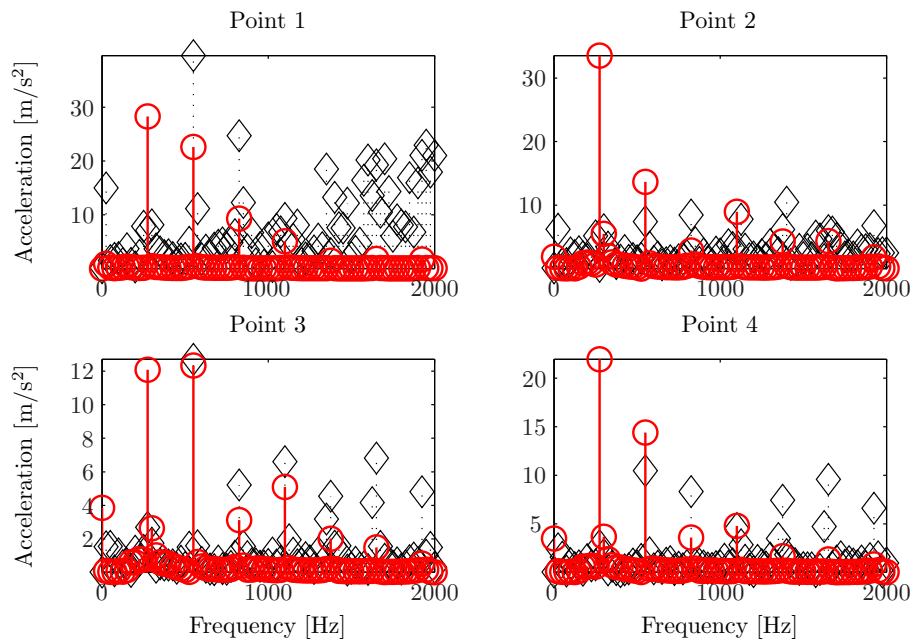


Figure 5.43: Pump casing accelerations in correspondence of points 1, 2, 3, 4 of Figure 5.20, zero flow condition. The black square markers represent experimental accelerations, while the red circular markers represent the calculated accelerations.

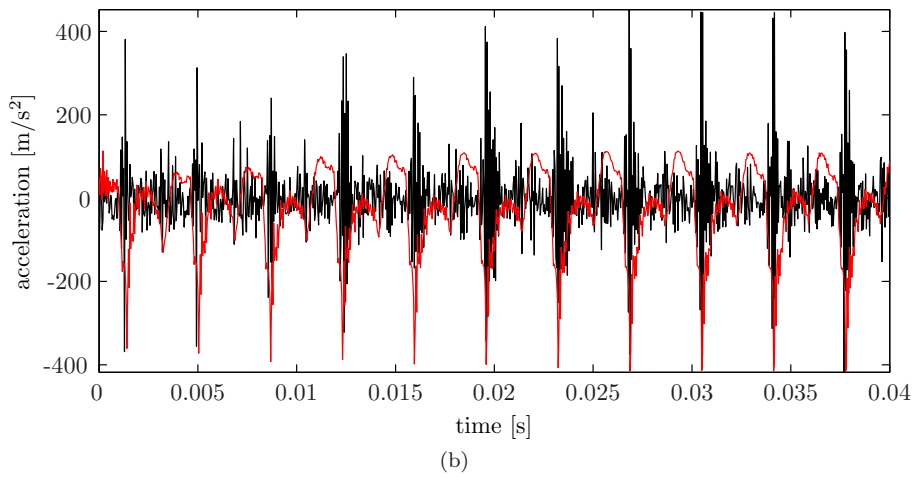
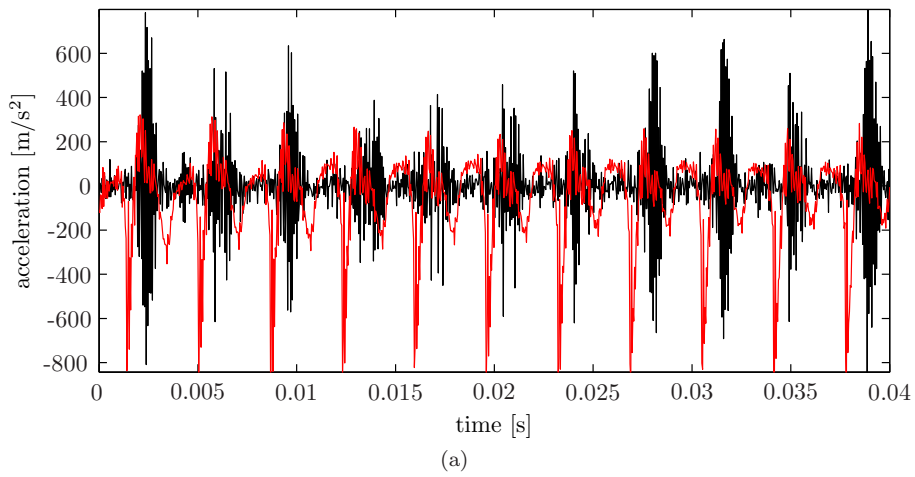


Figure 5.44: Comparison between the experimental and the calculated acceleration relative to point 3, in full flow condition (a) and in zero flow condition (b).



## Chapter 6

# Results and applications

*In the present chapter a general procedure to detect the main dynamical events taking place inside the pump in working conditions will be provided. Such a method uses the LP model results in terms of rotor shaft accelerations as an indicator of dynamical events. These results can be considered reliable since in the previous chapter a global validation procedure has been carried out.*

### 6.1 Dynamical events identification

Once the model has been validated following the procedure underlined in the previous chapter, it can be used to investigate the causes of unwanted dynamical phenomena.

As an example of application, the assessed LP model will be used in this section in order to evaluate dynamical effects related to the rotor shaft accelerations. The peaks clearly noticeable in the acceleration evolutions will be discussed and linked to dynamical phenomena taking place inside the pump in working condition. Such an event identification procedure can be a powerful tool for the designer since he can address his study to the critical events underlined by the accelerations peaks with the aim at improving the pump vibrational behavior.

#### 6.1.1 Full flow condition

Figure 6.1 depicts the acceleration evolution over one pitch, along  $x$  direction and  $y$  direction. The accelerations are plotted in function of the percentage of vane pitch  $\% \varphi_{vp}$ , since these accelerations are  $\varphi_{vp}$  periodic.

Five peaks are clearly noticeable, both in the acceleration along  $x$  and  $y$  direction. The events related to each peak are listed in Table 6.1. The 5 configurations relative to angular positions identified in Table 6.1 are reported in the following figures to better understand how the connections between the considered control volumes change over a vane pitch  $\varphi_{vp}$  in function of the angular coordinate  $\varphi$ .

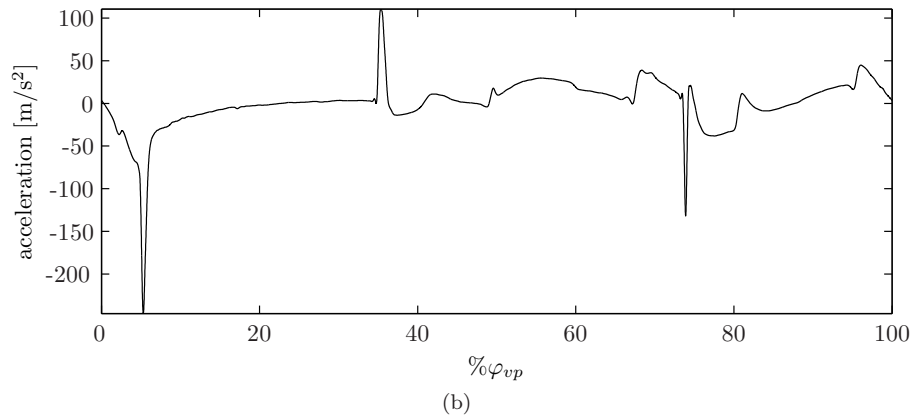
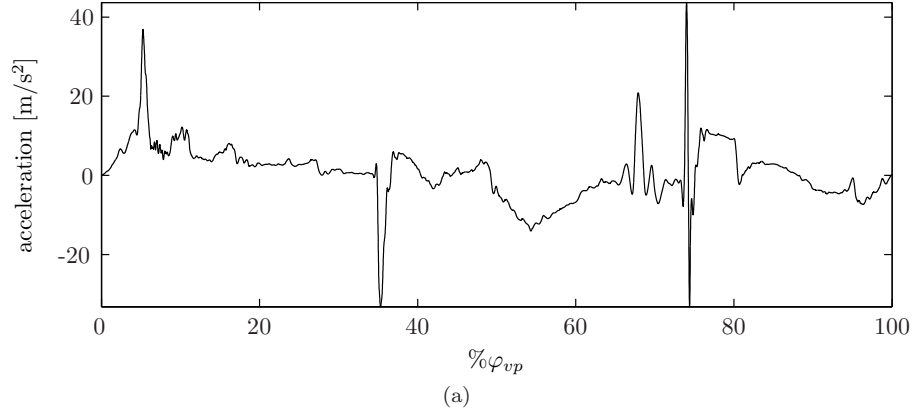


Figure 6.1: Rotor shaft accelerations in full flow condition, along  $x$  direction (a) and  $y$  direction (b).

Table 6.1: Main dynamical phenomena and time when they take place in percentage of the vane pitch.

$\% \varphi_{vp}$	$\varphi$ [deg]	Event
5%	1.7	$V_7$ is completely trapped
35%	11.5	$V_2$ is at the beginning of the outlet eyelet $V_{12}$ is at the beginning of the outlet eyelet
67%	22.2	$V_7$ is at the beginning of the inlet eyelet
74%	24.5	$V_1$ is completely trapped
95%	31.4	$V_1$ is at the beginning of the outlet carving



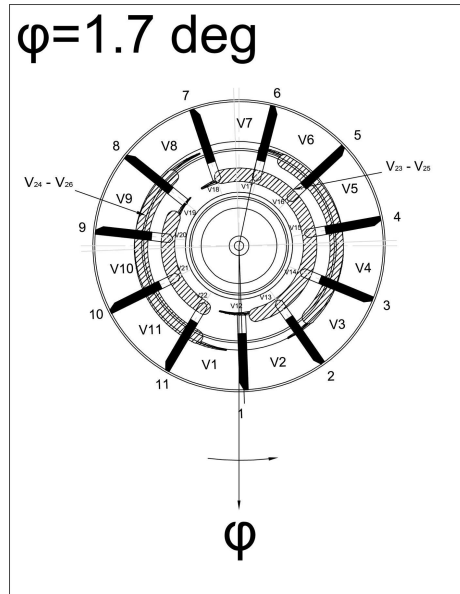


Figure 6.2: Control volumes configuration in the angular position corresponding to  $\varphi = 1.7$  deg.

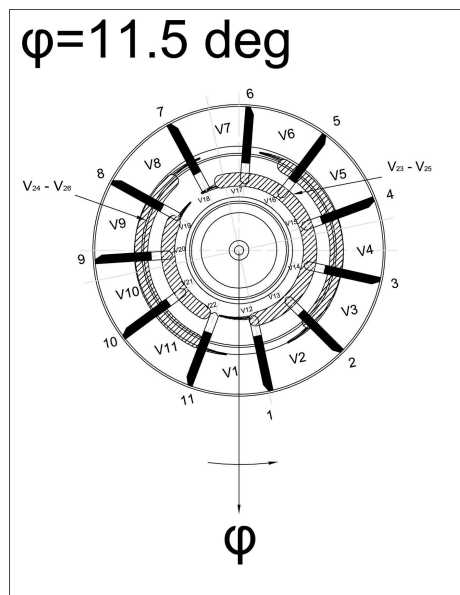


Figure 6.3: Control volumes configuration in the angular position corresponding to  $\varphi = 11.5$  deg.

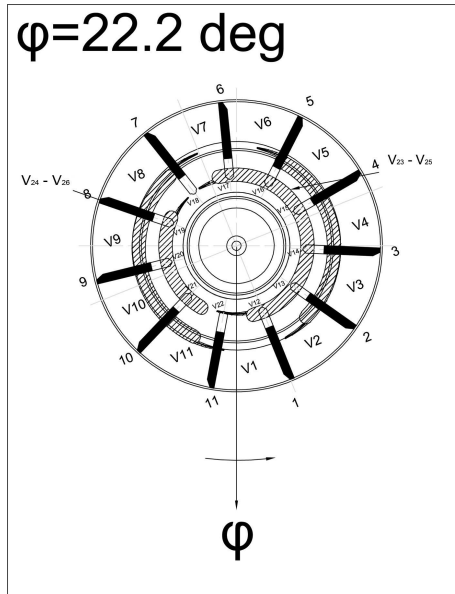


Figure 6.4: Control volumes configuration in the angular position corresponding to  $\varphi = 22.2 \text{ deg}$ .

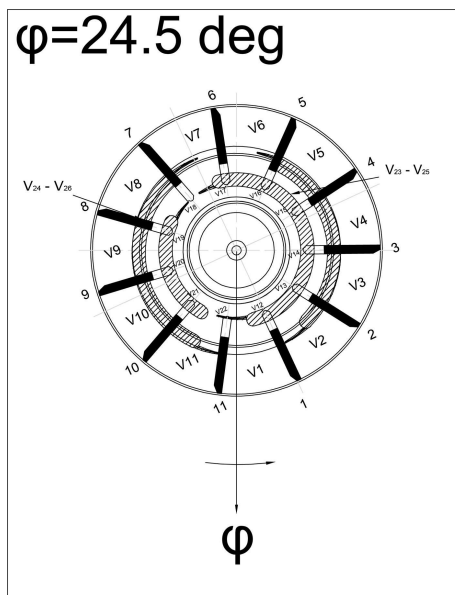


Figure 6.5: Control volumes configuration in the angular position corresponding to  $\varphi = 24.5 \text{ deg}$ .

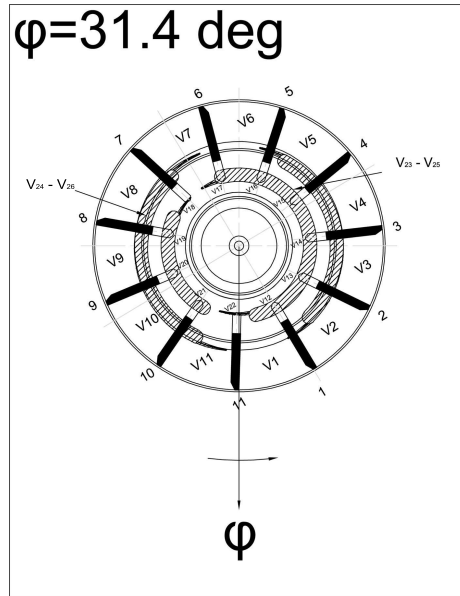


Figure 6.6: Control volumes configuration in the angular position corresponding to  $\varphi = 31.4$  deg.

### 6.1.2 Zero flow condition

Figure 6.7 depicts the acceleration evolution over one pitch, along  $x$  direction and  $y$  direction. The accelerations are plotted in function of the percentage of vane pitch  $\% \varphi_{vp}$ , since these accelerations are  $\varphi_{vp}$  periodic.

A more regular trend is depicted in zero flow condition with respect to full flow condition. As a matter of fact, the acceleration evolution over a vane pitch is characterized by smaller amplitude variations and by a single peak clearly noticeable in correspondence of the 74% of the vane pitch (see Figure 6.5). This fact can be explained taking into account the configuration in which the pump works in zero flow condition. The total eccentricity value is around 0 and for this reason the dynamical events related to shaft rotation are reduced to the one occurring at the angular coordinate  $\varphi = 24.5$  deg. In this position the control volume  $V_1$  is completely trapped. This angular coordinate corresponds to the position when the pressure increases from inlet to outlet pressure depicted in Figure 5.4.

Observing that the event underlined in the present analysis affects also the full flow condition behavior and furthermore, the typical working condition for this kind of pumps is the zero flow condition, the event taking place at 74% of the vane pitch is the first to be analyzed and improved.

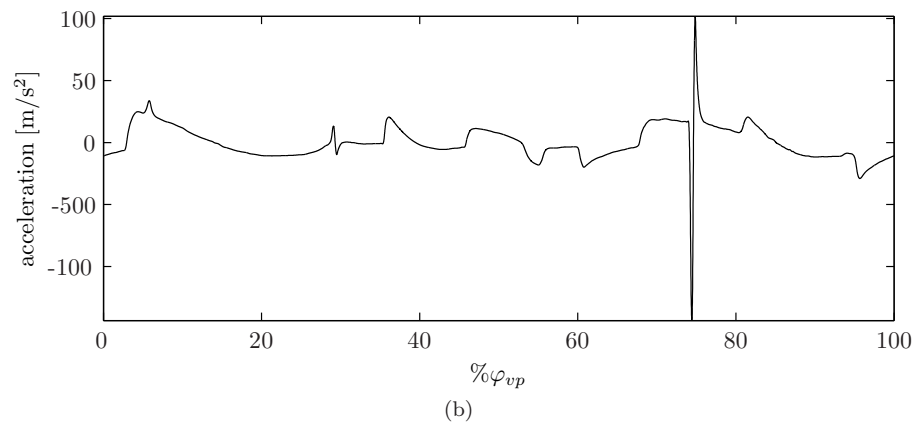
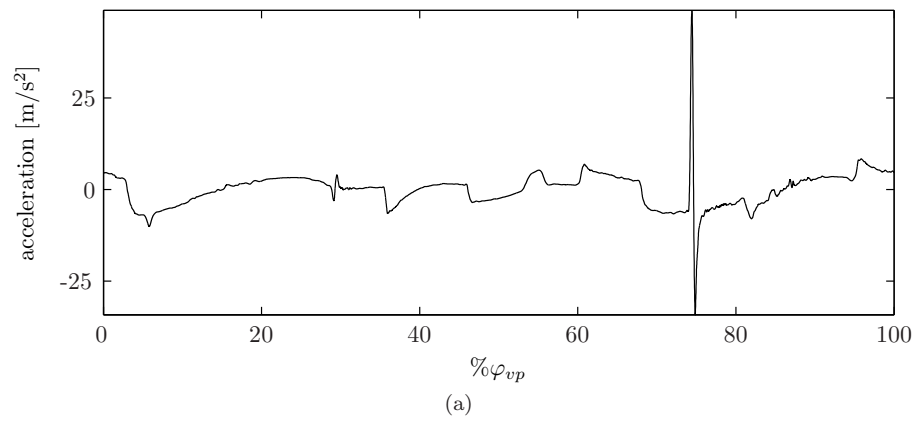


Figure 6.7: Rotor shaft accelerations in zero flow condition, along  $x$  direction (a) and  $y$  direction (b).

## Chapter 7

# Concluding remarks

This PhD thesis addresses the development of a *Lumped Parameter* model for the dynamic analysis of high pressure variable displacement vane pumps for machine tools applications whose description has been provided in Chapter 2. The developed model aims at obtaining the rotor shaft accelerations. To reach this target the rotor shaft equations of motion must be integrated. These equations can be written once the pressure field acting inside the pump is determined. This calculation allows to estimate the loads acting on the rotor shaft in terms of forces and torques and finally to write the system of equation of motion.

In Chapter 3 the *LP* model has been described from a theoretical point of view. In particular, section 3.1 deals with the *LP* model general formulation. This model takes into account the variability of the pressure evolution and forces acting on the rotor, the hydrodynamic journal bearing behavior, the friction due to viscous actions and contact forces, the rotor shaft stiffness and damping, the variations of the pump geometry with respect to working condition and all the inertia actions. It allows to calculate the rotor shaft accelerations, as well as the journal bearing reaction forces and the motor drive torque absorbed by the pump in working condition.

The *LP* model requires as input data the loads in terms of forces and torques. These quantities can be calculated once the pressure evolution is determined. A wide description of the procedure used to calculate the pressure field has been provided in section 3.2: the considered geometry and the assumptions on which the model is based are fully described. Hence, in section 3.4 the force calculation has been discussed. Two type of forces act on the rotor shaft; the two procedures useful to compute the pressure forces and the journal bearing reactions are developed. The first is based on the integration of the pressure evolution around the rotor, the latter uses the finite impedance theory to compute the journal bearing reaction forces. The load torques determination has been described in section 3.5. Three torque components have been distinguished: a load torque due to the pressure evolution inside the pump; a load torque due to the friction between the vane and the pressure ring and a load torque due to viscous actions. Finally, the journal bearing static equilibrium position has been defined in section 3.6. This position will be used as initial condition to start the integration iterative procedure with the aim at reducing the computational time.

In Chapter 4 the main problems related to model implementation in MATLAB

and Simulink are described and the most interesting code pieces are reported as well. In this frame the integration of the equation of motion characterizing the rotor shaft equilibrium is carried out in Symulink. The whole model has been described with reference to the blocks that constitutes itself. In more detail, the initial condition choice has been discussed, and the integration strategy as well as the interface between Symulink and MATLAB are explained by means of images depicting the block architecture. The main aspects related to the implementation in MATLAB of the subroutines devoted to the calculation of the pressure evolution and the pressure forces and the torques are discussed. The most interesting pieces of code are attached as well.

In Chapter 5 the method used to assess the *LP* model has been exposed. First of all the measurements performed during the test campaign have been described. A suitably modified pump has been used to measure the pressure evolutions in working conditions in all the regions of interest. Tests at different working pressures have been carried out to evaluate the flow rates and the motor drive torques in different working conditions. The method used to calculate the pressure forces from the pressure measurement has been explained, hence, the original procedure used to measure the frequency response functions of the pump casing is reported. Finally, the casing accelerations measurements and processing is briefly explained. The above mentioned experimental data have been used to assess the model and they are reported in sections 5.2.1, 5.2.2, 3.5, 5.2.5, 5.2.6.

This data have been used to assess the model by a validation procedure on several levels, in this way the goodness of intermediate results is checked as well. In more detail, the calculated pressure evolution has been assessed by using the experimental pressures. The same validation strategy has been applied to validate the flow rates and the torques. Subsequently, the pressure forces calculated by means of an *ad hoc* method applied to experimental and calculated pressures have been compared and discussed. Hence, the above mentioned forces have been combined with the frequency response functions to calculate the pump casing accelerations. This last results is finally assessed by comparison with the experimental accelerations and the results have been discussed as well.

In particular, Section 5.3.1 reports the validation of the pressure evolution obtained by the model, in the full flow rate as well as in the zero flow rate. The results have been compared with the pressures measured in working conditions and evaluated in terms of accuracy by means of the *Percentage of Good Points* index (*PGP*): the model showed an average accuracy of 73.3%. By analyzing the comparison between calculated and measured pressure evolutions it is possible to notice that the main discrepancy between the two pressure evolutions is related to the region where the pressure decreases from the outlet to the inlet pressure.

The results in terms of flow rate have been discussed in section 5.3.2. It can be noticed that the outlet flow rate in full flow condition computed by the *LP* model gives a correct estimation of the experimental value. Same considerations can be done for the outlet flow rate in zero flow condition. From the point of view of drainage flow rates, it can be noticed that the model overestimates the drainage flow rate in full flow condition, while underestimate the drainage flow rate in zero flow condition. In more detail, the outlet flow rate measured in full flow condition is 23.2 l/min, while the model predicts an outlet flow rate varying from 23.2 and 22.8 l/min. The drainage flow rate measured in full flow condition

varies from 1.5 to 2.7 l/min, while the model predicts drainage flow rate varying from 2.9 to 3.3 l/min. For the sake of brevity the flow rate comparison in the zero flow condition will be omitted in the present concluding remarks.

After having analyzed the results of pressure evolutions and flow rate calculations, the results in term of torques have been studied and validated in section 5.3.3. Variable displacement vane pumps with respect to fixed displacement vane pumps have the main advantage to self regulate their actual displacement accordingly to system requests. This fact allows to save energy when the pump is working in the zero flow condition. For this reason the motor drive torque has been compared both in full flow and in zero flow condition. The measured torque in full flow condition amounts to 76 Nm, while the motor drive torque predicted by the *LP* model varies from 73 to 79 Nm. In zero flow condition the model slightly overestimates the motor drive torque value since the torque measured in working condition amounts to 28 Nm, while the torque predicted by the *LP* model varies from 19 to 24 Nm. This last comparison can be considered satisfactory as well, but it must be taken into account that the torsiometer full scale is 500 Nm, so the small values to be measured are probably affected by observational errors.

Section 5.3.4 deals with the validation of results in terms of forces and torque. The force evolutions calculated by the model matches the main periodicity of the force evolutions calculated by experimental data. Nevertheless it has to be noticed that the *LP* model overestimates the force variation along the *y* direction and gives a force evolution in *x* direction characterize by a sudden variation not recognizable in the force evolution calculated from measured pressure data. This fact has been widely discussed in section 5.3.4. In this sight the *LP* model requires adjustments devoting at reducing the differences between simulated and measured quantity, however results in terms of forces can be considered promising and they can be used as input data for a further dynamical analysis described hereafter.

With the aim at assessing the *LP* model, a comparison in the frequency and time domain between the accelerations measured in working condition and the accelerations calculated combining the experimental *FRFs* with the calculated forces has been carried out in section 5.3.6. The procedure to calculate the pump casing accelerations is fully described from a theoretic point of view, hence the comparison of acceleration spectra has been done in the frequency range from 0 to 2000 Hz, since the forces calculated by the *LP* model does not excite the pump casing at higher frequencies. Furthermore, it has been observed that only accelerometers directly placed on the pump casing gives reliable measurements, in fact the spectra of the accelerations signals measured by the accelerometers on the pump cover are largely affected by noise in the considered frequency range. Considering the points on the pump casing, a good resemblance between measured and calculated accelerations spectra is obtained, with the exception of values relative to the frequency of 275 Hz. In fact the calculated accelerations usually overestimates the amplitude of this frequency component. The main reasons of these differences are related to the following lacks of *LP* model: the damping phenomena related to the presence of lubricant at high pressure inside the pump are not considered, the effects of lubricant inertia inside control volumes have been neglected, the accelerations of the pump casing are probably influenced by other paths not taken into account by the present work and the control piston is modeled as a rigid contact neglecting the relative damping

phenomena.

Hence, the signal has been reconstructed in the time domain and the *Root Mean Square (RMS)* of measured accelerations and calculated accelerations are compared both in full flow and in zero flow condition, obtaining respectively a percent error of 7.8% and 9.6%. It can be noted that this validation procedure can be considered as a global validation of the *LP* model.

Finally, as reported in Chapter 6, the assessed model can be used to relate the pump dynamic effects to the phenomena taking place in working condition. As an example in section 6.1 an event identification procedure is carried out. The pump has been studied both in full flow and in zero flow condition and the most critical event affecting the pump dynamical behavior was found to occur at the 74% of the vane pitch. In this angular position a vane space is completely trapped and a fast passage from inlet to outlet pressure can be found in the pressure evolution. This procedure can be a powerful tool for the designer who can address his study to the critical events underlined by the analysis to suitably modify the pump geometry in order to attenuate the dynamic effects. The main original contribution of this work concerns the application of a non-linear model to a variable displacement vane pump implementing formulations about the pressure evolution and variable forces acting on the rotor, the hydrodynamic journal bearing behavior, the friction due to viscous action and contact forces, the rotor shaft stiffness and damping, the variations of the pump geometry with respect to working condition and all the inertia actions. In particular, it is original to include all these important dynamic effects in the same model, with the aim at taking into account their interactions. This can be important in order to foresee the influence of working conditions and design modification on the pump vibrational behavior. In this sense the developed *LP* model could be a very useful tool in prototype design, in order to identify the origin of unwanted dynamic effects.



## Appendix A

# Inlet and outlet control volumes

In the present appendix the volumes of outlet and inlet ducts are provided. In more detail, the outlet duct corresponds to control volume  $V_{23}$  and the inlet duct corresponds to control volume  $V_{24}$ . Their values are resumed in Table A.1. The values of control volumes relative to inner distribution ( $V_{25}$  and  $V_{26}$ ) are provided as well.

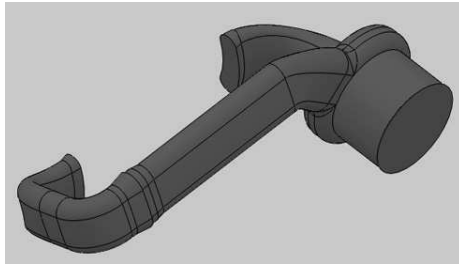


Figure A.1: The outlet control volume shape ( $V_{23}$ ).

Table A.1: Volume amount of inlet and outlet ducts.

Control volume	Volume [m <sup>3</sup> ]
Outlet control volume $V_{23}$	$2.46 \cdot 10^{-5}$
Inlet control volume $V_{24}$	$4.46 \cdot 10^{-5}$
Outlet control volume $V_{25}$	$7.37 \cdot 10^{-7}$
Inlet control volume $V_{26}$	$3.68 \cdot 10^{-7}$



Figure A.2: The inlet control volume shape ( $V_{24}$ ).

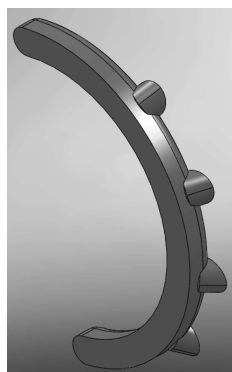


Figure A.3: The inner outlet control volume shape ( $V_{25}$ ).

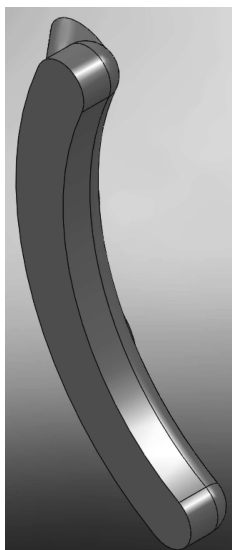


Figure A.4: The inner inlet control volume shape ( $V_{26}$ ).



## Appendix B

# Journal bearing reaction forces

The journal bearing reaction force is obtained as a result of the *LP* model, as explained in section 3.1. It has been supposed that journal bearing total reaction acts in correspondence of the *SEP* position calculated in section 3.6. As a remind, the accelerometers depicted in Figure 5.14, positions *C* and *D* are placed in the same positions underlined by the *SEP* calculation.

The journal bearing reactions in the full flow and zero flow condition are respectively depicted in Figures B.1 and B.2. These results will be used, together with the forces acting on the pressure ring ( $F_{stator,x}$  and  $F_{stator,y}$ ) and the *FRFs* experimentally measured in working condition, to calculate the acceleration of the pump casing surface.

It has been supposed that the total reaction force acting in points *C* and *D* can be calculated using equation (5.9).

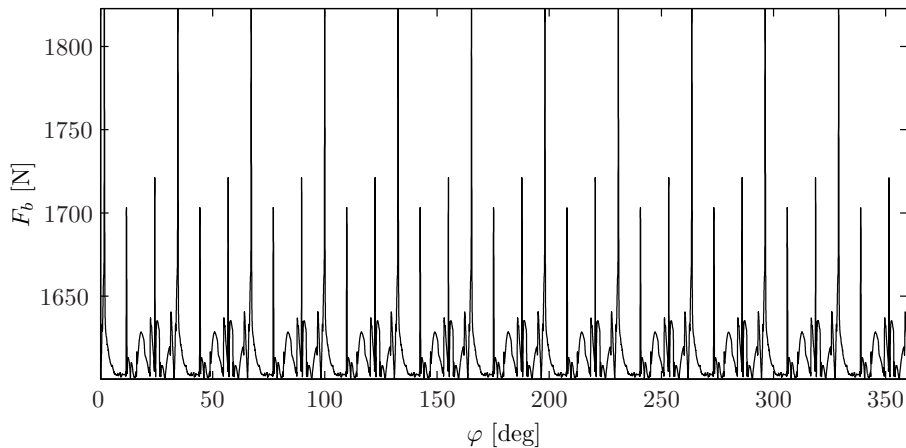


Figure B.1: Journal bearing reaction force in the full flow condition.

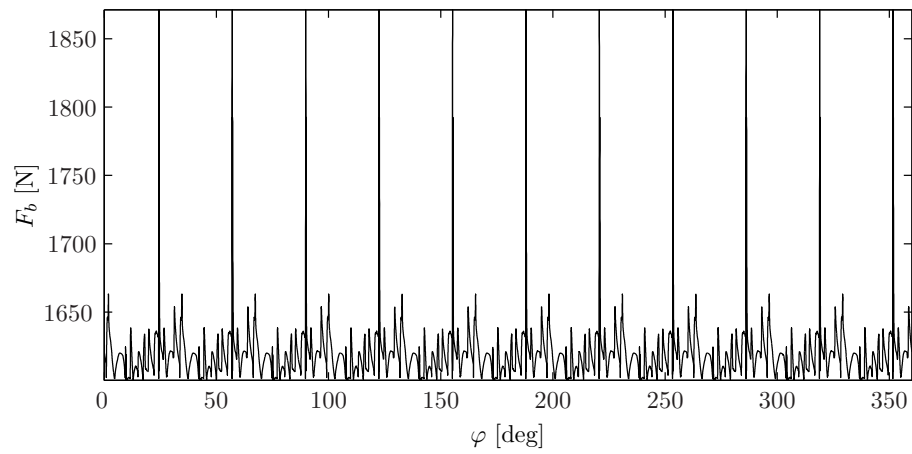


Figure B.2: Journal bearing reaction force in the zero flow condition.

# Bibliography

- [1] REXROTH. *Il Manuale di Oleodinamica*.
- [2] Mucchi, E., 2007. “Dynamic analysis of external gear pumps by means of non linear models and experimental techniques”. PhD thesis, Università degli Studi di Ferrara - Engineering Department in Ferrara, March.
- [3] Shampine, L. F., Gladwell, I., and Thompson, S., 2003. *Solving ODEs with matlab*. CAMBRIDGE.
- [4] Mucchi, E., Dalpiaz, G., and Fernández del Rincón, A., 2010. “Elastodynamic analysis of a gear pump. part 1: Pressure distribution and gear eccentricity”. *Mechanical Systems and Signal Processing*, **24**, pp. 2160–2179.
- [5] Mucchi, E., Dalpiaz, G., and Rivola, A., 2010. “Elastodynamic analysis of a gear pump. part 2: Meshing phenomena and simulation results”. *Mechanical Systems and Signal Processing*, **24**, pp. 2180–2197.
- [6] Mucchi, E., and Dalpiaz, G., 2008. “Simulation of gear pump dynamic behaviour by an integrated *lp/fe* model”. In *Seconda Giornata di Studio in Onore di Ettore Funaioli*, E. Asterisco, ed.
- [7] Childs, D., Moes, H., and van Leeuwen, H., 1977. “Journal bearing impedance descriptions for rotordynamic applications”. *Transactions of ASME*, pp. 198–214.
- [8] Hattori, K., Suzuki, H., and Hasegawa, J., 1987. “Design method of a small-ripple vane pump”. *SAE International*(871681).
- [9] Barbarelli, S., Bova, S., and Piccione, R., 2009. “Zero-dimensional model and pressure data analysis of a variable-displacement lubricating vane pump”. *SAE International*(2009-01-1859).
- [10] Cantore, G., Paltrinieri, F., Tosetti, F., and Milani, M., 2008. “Lumped parameters numerical simulation of a variable displacement vane pump for high speed ice lubrication”. *SAE International*(2008-01-2445).
- [11] Milani, M., Paltrinieri, F., Tosetti, F., Bianchini, A., Ferrara, G., and Ferrari, L., 2009. “Design and optimization of a variable displacement vane pump for high performance ic engine lubrication, part 2”. *SAE International*(2009-01-1064).
- [12] Borghi, M., Milani, M., and Valentini, A., 1999. “Pompe a palette - sperimentazione e calcolo”. *Oleodinamica Pneumatica Lubrificazione*, pp. 76–84.
- [13] Fiebig, W., and Heisel, U., 1993. “Comportamento dinamico di pompe a palette a regolazione di pressione”. *Oleodinamica-Pneumatica*, pp. 122–131.

- 
- [14] Mancò, S., Nervegna, N., Rundo, M., and Armenio, G., 2004. “Modeling and simulation of variable displacement vane pumps for ic engine lubrication”. *SAE International*(2004-01-1601).
- [15] Gellrich, R., Kunz, A., Beckmann, G., and E., B., 1995. “Theoretical and practical aspects of the wear of vane pumps, part a. adaptation of a model for predictive wear calculation”. *Wear*(181-183), pp. 862–867.
- [16] Novi, N., Squarcini, R., and Frenzo, F., 2009. “Dynamic and kinematic evaluation of automotive variable displacement vane pumps for reliability characterization”. *SAE International*(2009-01-0191).
- [17] Bianchini, A., Ferrara, G., Ferrari, L., Paltrinieri, F., Tosetti, F., and Milani, M., 2009. “Design and optimization of a variable displacement vane pump for high performance ic engine lubrication, part 1”. *SAE International*(2009-01-1045).
- [18] Kunz, A., Gellrich, R., Beckmann, G., and Broszeith, E., 1995. “Theoretical and practical aspects of the wear of vane pumps, part b. analysis of wear behaviour in the vickers vane pump test”. *Wear*(181-183), pp. 868–875.
- [19] Dickinson, A. L., Edge, K. A., and Johnston, D. N., 1993. “Measurements and prediction of power steering vane pump fluidborne noise”. In *Proceedings of the 1993 Noise and Vibration Conference*, S. of Automotive Engineers, ed.
- [20] Mucchi, E., Venturi, V., and Dalpiaz, G., 2007. “A hybrid  $lp/fe$  model for the dynamic analysis of external gear pumps”. In *Proceedings of the International Mechanical Engineering Congress & Expositions IMECEC2007*.
- [21] Nervegna, N., 2003. *Oleodinamica e Pneumatica*, Vol. 2. Politeko, Torino.
- [22] Belladonna, U., 2001. *Elementi di Oleodinamica*. Hoepli.
- [23] Rabie, M., 2009. *Fluid Power Engineering*. McGraw-Hill.
- [24] Cundiff, J. S., 2002. *Fluid power circuits and controls: fundamentals and applications*. CRC Press.
- [25] Majumdar, S. R., 2001. *Oil Hydraulic Systems: Principles and Maintenance*. McGraw-Hill.
- [26] *Pompa a Palette a Cilindrata Variabile ad Alta Pressione di esercizio - TIPO 01 PHV 05*. BERARAMA oleodinamica, Via G. Parini, 9 - 40033 - Casalecchio di Reno, Bologna, Italy.
- [27] THE MATHWORKS, 2001. *SIMULINK, Model-Based and System-Based Design*, June.
- [28] Mancò, S., and Nervegna, N., 1986. “Modello matematico di pompe oleodinamiche a ingranaggi esterni”. *Oleodinamica-Pneumatica*.
- [29] Bonacini, C., and Borghi, M., 1991. “Calcolo delle pressioni nei vani fra i denti di una macchina oleodinamica ad ingranaggi esterni”. *Oleodinamica-Pneumatica*.
- [30] Bigi, P., 1996. “Analisi teoretico-sperimentale di una pompa a palette”. Master’s thesis, Università degli Studi di Bologna - Facoltà di Ingegneria.
- [31] Funaioli, E., Maggiore, A., and Meneghetti, U., 1987. *Lezioni di Meccanica Applicata alle Macchine*. Pàtron editore.



- 
- [32] Venturi, V., 2008. “Advanced numerical methods for the dynamic optimisation of mechanical components”. PhD thesis, Università degli Studi di Ferrara - Engineering Department in Ferrara.
- [33] Booker, J. F., 1971. “Dynamically loaded bearings: Numerical application of the mobility method”. *Journal of Lubrication Technology*, pp. 168–176.
- [34] Raimondi, A. A., and Boyd, J., 1958. “A solution for the finite journal bearing and its application to analysis and design: part 1”. *A.S.L.E. Transactions*, **1**(1), pp. 159–173.
- [35] Raimondi, A. A., and Boyd, J., 1958. “A solution for the finite journal bearing and its application to analysis and design: part 2”. *A.S.L.E. Transactions*, **1**(1), pp. 175–193.
- [36] Raimondi, A. A., and Boyd, J., 1958. “A solution for the finite journal bearing and its application to analysis and design: part 3”. *A.S.L.E. Transactions*, **1**(1), pp. 194–209.
- [37] Rao, S. S., 2004. *Mechanical Vibrations*. Pearson Education International, Upper Saddle River.
- [38] Madenci, E., and Ibrahim, G., 2006. *The Finite Element Method and Applications in Engineering Using ANSYS*. Springer.
- [39] Hunt, B. R., Lipsman, R. L., and Rosenberg, J. M., 2001. *A Guide to MATLAB for Beginners and Experienced Users*. CAMBRIDGE.
- [40] Heylen, W., Lammens, S., and Sas, P., 2004. Modal analysis theory and testing.
- [41] LMS INTERNATIONAL, 2003. *Modal Impact User Manual*. Leuven.
- [42] BRÜEL & KJÆR, 1988. *Structural Testing - Part 1 - Mechanical Mobility Measurements*.
- [43] Bussola, R., and Tiboni, M., 1999. Parametrical identification for a complex mathematical model of indexing cam mechanisms by means of genetic algorithm. Tech. rep., Eurogen, Jyväskylä, Finland, May 30 - June 3.
- [44] Brown, S. J., 1986. *Mechanical Signature Analysis*. Academic Press, London.





Your E-Mail Address

marco.cavallari@unife.it

Subject

dichiarazione di conformita'

Io sottoscritto Dott. (Cognome e Nome)

Cavallari Marco

nato a

Legnago

Provincia

Verona

il giorno

30/12/1982

avendo frequentato il corso di Dottorato di Ricerca in:

Scienze dell'Ingegneria

Ciclo di Dottorato

XXIII

Titolo della tesi in Italiano

Modello a Parametri Concentrati per l'Analisi del Campo di Pressione e del Comportamento  
Vibrotorio di Pompe a Palette a Cilindrata Variabile

Titolo della tesi in Inglese

A Lumped Parameter Model for the Pressure and Vibration Analysis of Variable Displacement vane  
Pumps

Titolo della tesi in altra Lingua Straniera

Tutore - Prof:

Giorgio Dalpiaz

Settore Scientifico Disciplinare (SSD)

ING-IND/13

Parole chiave (max 10)

pressione pompe vibrazione parametri concentrati modello

Consapevole - Dichiaro

CONSAPEVOLE --- 1) del fatto che in caso di dichiarazioni mendaci, oltre alle sanzioni previste dal codice penale e dalle Leggi speciali per l'ipotesi di falsità in atti ed uso di atti falsi, decade fin dall'inizio e senza necessità di alcuna formalità dai benefici conseguenti al provvedimento emanato sulla base di tali dichiarazioni; -- 2) dell'obbligo per l'Università di provvedere al deposito di legge delle tesi di dottorato al fine di assicurarne la conservazione e la consultabilità da parte di terzi; -- 3) della procedura adottata dall'Università di Ferrara ove si richiede che la tesi sia consegnata dal dottorando in 4 copie di cui una in formato cartaceo e tre in formato .pdf, non modificabile su idonei supporti (CD-ROM, DVD) secondo le istruzioni pubblicate sul sito :

<http://www.unife.it/dottorati/dottorati.htm> alla voce ESAME FINALE – disposizioni e modulistica; --

4) del fatto che l'Università sulla base dei dati forniti, archiverà e renderà consultabile in rete il testo completo della tesi di dottorato di cui alla presente dichiarazione attraverso l'Archivio istituzionale ad accesso aperto "EPRINTS.unife.it" oltre che attraverso i Cataloghi delle Biblioteche Nazionali Centrali di Roma e Firenze. --- DICHIARO SOTTO LA MIA RESPONSABILITA' --- 1) che la copia della

tesi depositata presso l'Università di Ferrara in formato cartaceo, è del tutto identica a quelle presentate in formato elettronico (CD-ROM, DVD), a quelle da inviare ai Commissari di esame finale

e alla copia che produrrò in seduta d'esame finale. Di conseguenza va esclusa qualsiasi responsabilità dell'Ateneo stesso per quanto riguarda eventuali errori, imprecisioni o omissioni nei contenuti della tesi; -- 2) di prendere atto che la tesi in formato cartaceo è l'unica alla quale farà riferimento l'Università per rilasciare, a mia richiesta, la dichiarazione di conformità di eventuali copie; -- 3) che il contenuto e l'organizzazione della tesi è opera originale da me realizzata e non compromette in alcun modo i diritti di terzi, ivi compresi quelli relativi alla sicurezza dei dati personali; che pertanto l'Università è in ogni caso esente da responsabilità di qualsivoglia natura civile, amministrativa o penale e sarà da me tenuta indenne da qualsiasi richiesta o rivendicazione da parte di terzi; -- 4) che la tesi di dottorato non è il risultato di attività rientranti nella normativa sulla proprietà industriale, non è stata prodotta nell'ambito di progetti finanziati da soggetti pubblici o privati con vincoli alla divulgazione dei risultati, non è oggetto di eventuali registrazioni di tipo brevettale o di tutela. --- PER ACCETTAZIONE DI QUANTO SOPRA RIPORTATO

Firma Dottorando \_\_\_\_\_  
Ferrara, li 09 febbraio 2011 . Firma del Dottorando

Firma Tutore Marco Corbelli  
Visto: Il Tutore Si approva Firma del Tutore Esposito